

**SYNCHROTRON-BASED SPECTROMICROSCOPIC
CHARACTERIZATION OF AEROSOL CHEMISTRY**

A Dissertation
Presented to
The Academic Faculty

by

Amelia F. Longo

In Partial Fulfillment
of the Requirements for the Degree
Doctor of Philosophy in the
School of Earth and Atmospheric Sciences

Georgia Institute of Technology
May 2016

COPYRIGHT © 2016 AMELIA F. LONGO

**SYNCHROTRON-BASED SPECTROMICROSCOPIC
CHARACTERIZATION OF AEROSOL CHEMISTRY**

Approved by:

Dr. Ellery Ingall, Advisor
School of Earth and Atmospheric Sciences
Georgia Institute of Technology

Dr. Rodney Weber
School of Earth and Atmospheric
Sciences
Georgia Institute of Technology

Dr. Jennifer Glass
School of Earth and Atmospheric Sciences
Georgia Institute of Technology

Dr. Yan Feng
Environmental Science Division
Argonne National Laboratory

Dr. Yuanzhi Tang
School of Earth and Atmospheric Sciences
Georgia Institute of Technology

Date Approved: March 18, 2016

ACKNOWLEDGEMENTS

My time as a Ph. D. student was marked by the opportunity to work with a number of talented scientists, both inside and outside of my field. These people took the time to share their knowledge and insights not only on science, but on life. Among these individuals is my academic advisor, Ellery Ingall, whose guidance has helped me navigate my doctoral studies and whose support and humor has made him a friend. I would also like to thank Dr. Yan Feng for her perseverance, support, and the outside perspective she is always willing to provide. I would like to recognize the many collaborators who have help create the research described in this dissertation. Without their willingness to share samples and data, this work out not be possible. I would like to thank Dr. Yuanzhi Tang, Dr. Jennifer Glass, and Dr. Rodney Weber for the insights they have provided on my dissertation.

Finally, I would like to thank my family for always supporting my academic pursuits with their love, encouragement, and care packages.

TABLE OF CONTENTS

	Page
ACKNOWLEDGEMENTS	iii
LIST OF TABLES	viii
LIST OF FIGURES	ix
LIST OF SYMBOLS AND ABBREVIATIONS	x
SUMMARY	xi
<u>CHAPTER</u>	
1 Introduction	1
1.1 Historical focus of aerosol chemistry	1
1.2 Effect of aerosols on human health	1
1.3 Role of aerosols in biogeochemical cycling and climatic processes	2
1.4 Synchrotron-based spectromicroscopy	4
1.5 Overview of Dissertation	6
2 P-NEXFS analysis of aerosol phosphorus delivered to the Mediterranean Sea	7
2.1 Abstract	7
2.2 Introduction	8
2.3 Methods	9
2.3.1 Ambient aerosol collection	9
2.3.2 Emission source collection	10
2.3.3 Total phosphorus and soluble phosphate determination	11
2.3.4 Synchrotron-based X-ray spectromicroscopy	12
2.3.5 P-NEXFS data analysis	14
2.4 Results and Discussion	16

2.4.1	Ambient aerosols	16
2.4.2	Emission sources	20
2.5	Conclusions	21
2.6	Supporting Materials	22
3	Composition and oxidation state of sulfur in atmospheric particulate matter	28
3.1	Abstract	28
3.2	Introduction	29
3.3	Methods	32
3.3.1	Ambient aerosol collection	32
3.3.2	Emission source collection	33
3.3.3	Sulfate standards	34
3.3.4	Synchrotron-based spectromicroscopy	34
3.3.5	Data analysis	36
3.4	Results	37
3.4.1	Oxidation state of sulfur	37
3.4.2	Sulfate composition	40
3.5	Discussion	43
3.6	Supporting Material	47
4	Iron oxidation state and composition of Saharan aerosols: Evidence of modification during atmospheric transport	51
4.1	Abstract	51
4.2	Introduction	52
4.3	Methods	54
4.3.1	Sample collection	54
4.3.2	HYSPLIT	56
4.3.3	Total and soluble iron	58

4.3.4 Soluble ions	59
4.3.5 pH modelling	59
4.3.6 Synchrotron Analysis	60
4.3.7 Data reduction and analysis	62
4.4 Results	63
4.4.1 Iron solubility	64
4.4.2 Iron composition	65
4.4.3 Oxidation State	67
4.5 Discussion	69
4.6 Supporting materials	74
5 The role of iron composition and oxidation state in the solubility of aerosol iron	79
5.1 Abstract	79
5.2 Introduction	80
5.3 Methods	82
5.3.1 Sample collection	82
5.3.2 HYSPLIT	84
5.3.3 Total and soluble iron	85
5.3.4 Soluble ions and pH modelling	86
5.3.5 Synchrotron analysis	87
5.3.6 Data reduction and analysis	89
5.4 Results	90
5.4.1 Iron solubility	90
5.4.2 Oxidation state	92
5.4.3 Iron composition	93
5.5 Discussion	95

5.6 Supporting materials	104
APPENDIX A: Standard Databases	110
REFERENCES	111
VITA	130

LIST OF TABLES

	Page
Table 2.1: Total and Soluble Phosphorus of PM10 Samples collected at Finokalia Research Station	22
Table 2.2: Organic Phosphorus Compounds and CAS Numbers	26
Table 3.1: Summary of Ambient PM2.5 Collection	47
Table 3.2: Composition of Sulfate from Bulk Ambient Aerosols and Emission Sources	49
Table 3.3: Composition of Sulfate in Individual Particles	50
Table 4.1: Collection Locations of Saharan Soil Collected from Morocco, Libya, and Senegal	74
Table 4.2: Iron Data Table for Saharan Air Masses	75
Table 4.3: Concentration of Soluble Ions to model pH with ISORROPIA	76
Table 4.4: Compositional Cluster of Bulk Samples and Individual Particles for Saharan Soil and Each Aerosol Collection Location	77
Table 5.1: Sample Collection Information for India, Southern Ocean, Finokalia Research Station, and GEOTRACES Samples	104
Table 5.2: Sample Collection for Samples Collected at the Bermuda Institute of Ocean Science	105
Table 5.3: Sample Collection Locations	106
Table 5.4: Bermuda Institute of Ocean Science Aerosol Data	107
Table 5.5: India, GEOTRACES, Southern Ocean, and Finokalia Research Station Aerosol Data	108
Table 5.6: Composition of Bulk Aerosol and Individual Aerosol Particle Samples	109

LIST OF FIGURES

	Page
Figure 2.1: Total and Soluble Phosphorus of Mediterranean Aerosols	16
Figure 2.2: Phosphorus Composition of Mediterranean Aerosols	17
Figure 2.3: Relationship between Phosphorus Composition and Relative Solubility of Phosphorus	19
Figure 2.4: HYSPLIT Back Trajectories for Air Masses Originating in Europe and North Africa	23
Figure 2.5: Spectra of Several Organic Phosphorus Standards	27
Figure 3.1: The Oxidation State of Sulfur in Common Emission Sources	38
Figure 3.2: Sulfur Oxidation State of Bulk Aerosol and Individual Aerosol Particles	39
Figure 3.3: Bulk and Individual Particle Sulfate Composition	41
Figure 3.4: X-ray Fluorescence Maps of Sulfur for Two Ambient Particulate Matter Samples	48
Figure 4.1: Total and Soluble Iron of Saharan Dust	64
Figure 4.2: Mean Bulk and Individual Particle Iron Composition of Saharan Dust	67
Figure 4.3: Travel Time as a Function of Iron Oxidation State	68
Figure 4.4: The Fe-XANES Spectra of Saharan Soil compared to the Fe-XANES Spectra from Individual Particle from the GEOTRACES Collection Station	78
Figure 5.1: Total and Soluble Iron from Global Sample Set	91
Figure 5.2: Solubility of Iron plotted against Oxidation State of Iron	92
Figure 5.3: Average Bulk Iron Composition of Each Sampling Location	94
Figure 5.4: Iron Solubility as a function of pH	98
Figure 5.5: Factors Affecting the Solubility of Iron at Individual Collection Locations	100

LIST OF SYMBOLS AND ABBREVIATIONS

BIOS		Bermuda Institute of Ocean Science
eV		Electron Volt
DMS		Dimethyl sulfide
Fe		Iron
FRS		Finokalia Research Station
HNLC		High Nutrient Low Chlorophyll
HYSPLIT		Hybrid Singly Particle Lagrangian Trajectory Model
P		Phosphorus
PCA		Principal Component Analysis
P-	NEXFS	Phosphorus Near Edge X-ray Fluorescence Spectroscopy
PM10		Particulate Matter with an aerodynamic diameter of < 10 μm
PM2.5		Particulate Matter with an aerodynamic diameter of < 2.5 μm
S		Sulfur
Si		Silicon
S-	NEXFS	Sulfur Near Edge X-ray Fluorescence Spectroscopy
S. O.		Southern Ocean
TSP		Total Suspended Particles
XANES		X-ray Absorption Near Edge Structure
XRF		X-ray Fluorescence

SUMMARY

Synchrotron-based techniques provide a powerful and surprisingly underutilized approach to explore atmospheric aerosol chemistry. These techniques were employed to investigate phosphorus, sulfur, and iron in aerosols to address oceanographic and environmental research questions. By using X-ray fluorescence microscopy and near edge X-ray fluorescence spectroscopy, a variety of chemical properties including the oxidation state, local structure, physical distribution, elemental associations, and mineralogy of the element of interest can be obtained for both individual aerosol particles and bulk aerosol samples. When used in conjunction with ancillary measurements, such as solubility and pH, synchrotron-based techniques can provide evidence of underlying chemical mechanisms occurring during atmospheric transport. Chapter 1 provides a historical view of aerosol research as well as touching on human health and biogeochemical implications of aerosols. Phosphorus and iron, vital nutrients for all organisms, control the primary productivity of many ocean regions, and aerosol deposition constitutes a major source of nutrients to remote ocean regions. However, the factors controlling the solubility and bioavailability of iron and phosphorus remain unclear. The phosphorus-limited Mediterranean Sea receives seasonal inputs of Saharan dust, which have been extensively studied as a source of phosphorus to marine phytoplankton. In Chapter 2, phosphorus from Mediterranean aerosols were examined, and aerosol phosphorus from European air masses was found to be more than three times more soluble than phosphorus from North African air masses. This suggests that while

North African air masses deliver more total phosphorus to the Mediterranean, the phosphorus from Europe is substantially more soluble, and bioavailable.

The remaining chapters all yielded insights on metal chemistry occurring in the atmosphere. Chapter 3 examines the composition and oxidation of sulfur in ambient aerosols collected from the greater Atlanta, Georgia area and common emission sources. Metal sulfates were found at both the bulk and individual particle levels, highlighting the importance of sulfur and transition metal interactions in the atmosphere. Individual aerosol particles consistently contained reduced sulfur in the elemental sulfur oxidation state. The reduced sulfur, S^0 , was found to account for up to 20% of total sulfur in large particles ($>1 \mu\text{m}$). The ultimate source of this sulfur species is likely a primary emission due to incomplete combustion or aerosolized bacteria from soil.

Chapter 4 focuses on the characterization of iron in aerosolized Saharan dust. Examination of Saharan dust after different distances of atmospheric transport revealed shifts in oxidation state, composition, and pH. The longer air masses spent travelling through the atmosphere, the more reduced the iron became. This suggests that a reductive mechanism is at work in the atmosphere to transform aerosol iron in Saharan dust. The pH was also consistently lower in samples that had a longer travel time. The finding of lower pH in these samples suggests that acidic processes are working to solubilize aerosol iron in Saharan dust. This is further supported by the finding of iron sulfates and iron phosphates, phases that likely formed as a result of secondary acidic processes in the atmosphere.

Building on this study of aerosol iron in Chapter 5, a global sample set was compiled with samples from the Mediterranean, India, the Southern Ocean, the Atlantic

Ocean, and Bermuda. Generally, samples that contained high total iron contained iron that was relatively less soluble, and conversely, samples with low total iron contained iron that was relatively more soluble. Ambient aerosols across all sampling locations were dominated by iron oxides and often contained iron sulfates as a constituent. The presence of iron sulfates could indicate that acidic reactions are taking place in the samples, however; there was no unifying factor that appeared to control the solubility of aerosol iron across all sampling locations. There were general trends among specific sampling locations. For example, Mediterranean samples showed that iron solubility was correlated with pH, suggesting acidic reactions may control the solubility of aerosol iron at this location. This sampling location specific relationships suggest that source region, rather than a single transformation mechanism, likely plays a key role in determining the solubility of aerosol iron. This work demonstrates the potential of applying synchrotron-based techniques to studies of atmospheric chemistry and lays the foundation for future studies to further unravel the particle aging.

CHAPTER 1

INTRODUCTION

1.1 Historical focus of aerosol chemistry

Atmospheric aerosols are solid or liquid particles that exist in and are transported through the atmosphere. Aerosols can be directly emitted from anthropogenic and biogenic sources, which is considered a primary emission. Aerosols can also form in the atmosphere from gaseous constituents through secondary processes. For years, studies of atmospheric chemistry have centered on ameliorating air pollution (Dockery & Pope, 1994; Kay, 1952; Munger, 1952; Schwartz, Dockery, & Neas, 1996). Air pollution was viewed as a concentration of a contaminant that could cause damage to human health, property, or discomfort and was largely focused on primary emission sources (Munger, 1952) until secondary pollutants, such as ozone, came to light (Atkinson & Smith, 1983). Air pollution studies, as with many advances in environmental health, stemmed from the adverse human health effects associated with aerosols.

1.2 Effect of aerosols on human health

Throughout history there have been events of severe air pollution that have drawn attention to the adverse effects of aerosols on human health. London's smog episodes of 1952 are among the most famous; however, other notable events have occurred in Meuse Valley, Belgium in December 1930 and Donora, Pennsylvania (Dockery & Pope, 1994).

These extreme air pollution events that dramatically affected human health were some of the first indicators that air pollution could adversely affect human health on a large scale. In these cases, particulates and sulfur oxides were responsible for respiratory disease. Negative health effects have also been linked to oxidative stress caused by reactive oxygen species. Water soluble transition metals have been shown to form reactive oxygen species through redox cycling in the atmosphere (Kelly, 2003; Vidrio, Jung, & Anastasio, 2008). Aerosol iron, specifically, was believed to play an important role in the formation of reactive oxygen species (Shafer et al., 2010; Y. Zhang, Schauer, Shafer, Hannigan, & Dutton, 2008). These species link aerosols to cardiovascular disease as well (Tao, Gonzalez-Flecha, & Kobzik, 2003).

1.3 Role of aerosols in biogeochemical cycling and climatic processes

Aerosols play a key role in climatic processes by absorbing solar radiation in the atmosphere or reflecting solar radiation back into space (Ramanathan, Crutzen, Kiehl, & Rosenfeld, 2001). Aerosols also serve a key purpose as cloud condensation nuclei and ice nuclei, which can lead to increased cloud albedo (Twomey, 1977). Both the reflection of solar radiation and the increased cloud albedo lead to a net cooling effect. Increased cloud albedo through cloud condensation nuclei has also been tied to biological processes. Some marine phytoplankton produce a compound called dimethyl sulfide, or DMS. Dimethyl sulfide is then oxidized to sulfur dioxide in the atmosphere, where it becomes effective cloud condensation nuclei (Charlson, Lovelock, Andreae, & Warren, 1987). The resulting increased cloud albedo is further hypothesized to play role in mediating sunlight and surface temperature, potentially selecting which marine phytoplankton will be most successful, and creating a feedback loop.

The shift from pollution based to oceanographically-focused aerosol studies occurred with the iron hypothesis, which linked the iron and carbon cycles (Martin, 1990). Briefly, the iron hypothesis states that inputs of iron to high nutrient low chlorophyll regions will lead to algal blooms large enough to sequester significant carbon dioxide (Martin, 1990). Vast ocean regions are limited by nutrients, including phosphorus and iron (Graham & Duce, 1982; Krom, Emeis, & Van Cappellen, 2010; Krom, Kress, Brenner, & Gordon, 1991; Mahowald et al., 2008). This was even suggested as a mitigation strategy for the buildup of carbon dioxide in the atmosphere. While riverine inputs can alleviate nutrient limitation in coastal regions, aerosol deposition is the major source of nutrient input in remote ocean regions. Seasonal inputs of nutrients from aerosol deposition can lead to algae blooms. This phenomenon was extensively studied as part of the iron hypothesis (Boyd et al., 2000; Buesseler, Andrews, Pike, & Charette, 2004; K. H. Coale et al., 2004; K.H. Coale, Johnson, & Fitzwater, 1996; de Jong et al., 2012). Similarly, phosphorus controls the productivity of the Mediterranean Sea. Mineral dust inputs from the Sahara Desert have been studied as a source of seasonal phosphorus to the Mediterranean (Escudero et al., 2011; Ganor & Mamane, 1982; Guerzoni et al., 1999). Both iron and phosphorus exist only in the solid and aqueous phases in the atmosphere, with no gaseous phase; therefore, some of the processes (such as acid processing) that are hypothesized to control the solubility of phosphorus are also hypothesized to control the solubility of iron.

Chemical transformations that occur during atmospheric transport are suggested to control the solubility of phosphorus and iron. The solubility of these elements is crucial because it is intrinsically linked to their bioavailability; however, the factors that control the solubility of aerosol phosphorus and iron still remain unclear (Beauchemin et al., 2003; Jickells et al., 2005; Mackey et al., 2012; Mahowald et al., 2005). Both of these elements are susceptible to acid mobilization, which has led to the acidic reactions as a

leading hypothesis to explain solubility variations. Acidic species, such as sulfuric and nitric acid, can accumulate on a particle, overcoming the carbonate buffer capacity. This allows the pH of a particle to fall as low as 1 to 2, where recalcitrant phosphorus and iron minerals become more soluble (Nenes et al., 2011; Oakes, Ingall, et al., 2012; Z. Shi et al., 2011).

Iron has more complex chemistry, compared to phosphorus, as a redox active element. In addition to acidification as a means to solubilize aerosol iron, photo-chemical reactions and ligand assisted dissolution are also key chemical mechanisms that may occur during atmospheric transport (Paris, Desboeufs, & Journet, 2011; X. Zhu et al., 1993). For iron, bioavailability is tied to oxidation state as well as solubility. Photo-chemical reactions and ligand-assisted dissolution often involve the redox cycling of iron. The speciation of aerosol iron has even been suggested to affect the bioavailability of iron over glacial-interglacial timescales. During the Last Glacial Maximum, reduced iron(II) increased by up to seven times more than interglacial levels; in contrast, iron(III) was found to only double (Spolaor, Vallelonga, Cozzi, Gabrielli, et al., 2013). This further links aerosol chemistry to climatic scale responses.

1.4 Synchrotron-based spectromicroscopy

Synchrotron-based techniques allow for unique characterizations from nanometer to centimeter spatial scales. X-ray fluorescence (XRF) microscopy has been extensively used in the field of biology (Baines et al., 2011; E Ingall et al., 2013; Twining et al., 2011). XRF microscopy has also been widely used to examine environmental samples such as soils and sediments (Diaz et al., 2008); however, the application of synchrotron-based spectroscopy is more common (D. Hesterberg, Zhou, Hutchison, Beauchemin, & Sayers, 1999; Dean Hesterberg, 2010; Morra, Fendorf, & Brown, 1997; J. Prietzel et al., 2011; J. Prietzel, Thieme, Eusterhues, & Eichert, 2007; Jörg Prietzel, Dümig, Wu, Zhou,

& Klysubun, 2013). The application of synchrotron-based spectromicroscopy on aerosol studies is a relatively new field of research (De Santiago et al., 2014; Higashi & Takahashi, 2009; Longo et al., 2014; Ryan C. Moffet et al., 2012; Oakes, Ingall, et al., 2012; Oakes, Weber, Lai, Russell, & Ingall, 2012; Y. Takahashi et al., 2006).

Synchrotron-based techniques are ideal for aerosol studies due to the spatial scales that these techniques can access. In this work, two spatial scales are employed. The millimeter spatial scale is used to obtain an average view of aerosol composition. In this mode, only spectroscopy is used, and is commonly referred to as ‘bulk’ spectroscopy. The second analysis mode accesses micron to sub-micron spatial scales. Here, both XRF microscopy and spectroscopy are employed. The XRF microscopy and spectroscopy methods employed in this study detect fluorescence signals. These techniques use X-ray photons to eject inner core electrons. The energy required to eject an electron from the K electron shell of an atom occurs at an energy value termed the K-edge. As electrons from higher shells relax back into the vacant K shell, a fluorescence signal is emitted. The heavier the element, the more energy is needed to eject K-shell electrons. For example, iron has a higher K-edge than sulfur and phosphorus. In spectroscopic techniques, the sample is scanned over a range of incident energies, centered around the K-edge, making spectroscopic techniques element-specific. Features of the energy versus fluorescence scan provide information on oxidation state for redox active metals as well as information on the chemical form of the element of interest. In XRF microscopy, a single incident energy is used. Incident X-ray energy is typically set at an energy that is high enough to excite all the elements of interest. By choosing the correct incident energy, the distribution of each element of interest can be visualized, thus allowing the determination of the physical distribution of elements of interest, as well as its spatial association with other elements. The sample is then rastered through the focused X-ray beam with fine motors to generate images. This technique can yield concentration information but not

compositional information. By combining these techniques to examine aerosol samples, individual aerosol particles can be located through XRF microscopy and interrogated with spectroscopy.

1.5 Overview of dissertation

In this dissertation, aerosol chemistry of iron, phosphorus, and sulfur will be explored through the application of synchrotron-based techniques. By employing synchrotron spectromicroscopy, aerosols can be examined at both the bulk scale, where an average composition is determined, as well as at the individual particle level. Insights from composition and oxidation state were combined with traditional wet chemistry techniques to elucidate secondary processes that modify aerosol chemistry during atmospheric transport.

In Chapter 2, the composition of phosphorus in Mediterranean samples will be explored. By examining relationships between phosphorus composition, solubility, and source region, differences between anthropogenically influenced European air masses and mineral dust influenced North African air masses will be determined. In Chapter 3, the oxidation state of aerosol sulfur and the composition of sulfate aerosol is examined for samples collected from Atlanta, Georgia. This examination provides further evidence that metal sulfates likely play a key role in the aerosol chemistry of urban environments. Chapters 4 and 5 focus on aerosol iron speciation. In Chapter 4, the composition and oxidation state of iron in Saharan dust revealed evidence of both acidic and reductive reactions taking place during atmospheric transport. In the final chapter, samples from five different locations were used to search for global trends in aerosol iron solubility. Relationships between iron solubility and iron composition, iron oxidation state, distance travelled, pH, and elemental concentrations were explored by sampling location as well as for all sampling locations together.

CHAPTER 2

P-NEXFS ANALYSIS OF AEROSOL PHOSPHORUS DELIVERED TO THE MEDITERRANEAN SEA

2.1 Abstract

Biological productivity in many ocean regions is controlled by the availability of the nutrient phosphorus. In the Mediterranean Sea, aerosol deposition is a key source of phosphorus and understanding its composition is critical for determining its potential bioavailability. Aerosol phosphorus was investigated in European and North African air masses using Phosphorus Near Edge X-ray Fluorescence Spectroscopy (P-NEXFS). These air masses are the main source of aerosol deposition to the Mediterranean Sea. We show that European aerosols are a significant source of soluble phosphorus to the Mediterranean Sea. European aerosols deliver on average 3.5 times more soluble phosphorus than North African aerosols and furthermore are dominated by organic phosphorus compounds. The ultimate source of organic phosphorus does not stem from

Longo, A.F., Ingall, E.D., Diaz, J.M., Oakes, M., King, L.E., Nenes, A., Mihalopoulos, N., Violaki, K., Avila, A., Benitez-Nelson, C.R., Brandes, J., McNulty, I., Vine, D.J. (2014) P-NEXFS Analysis of Aerosol Phosphorus Delivered to the Mediterranean Sea. *Geophysical Research Letters*. DOI: 10.1002/2014GL060555.

common primary emission sources. Rather, phosphorus associated with bacteria best explains the presence of organic phosphorus in Mediterranean aerosols.

2.2 Introduction

Atmospheric deposition is an important source of nutrients to oligotrophic ocean regions (Graham & Duce, 1982; Mahowald et al., 2008). In the Eastern Mediterranean Sea, biological productivity is strongly limited by the vital nutrient phosphorus (Krom et al., 2010; Krom et al., 1991), with aerosol deposition accounting for at least one third of all phosphorus inputs (Ganor & Mamane, 1982). Large dust plumes, clearly visible in satellite images, stretch from North Africa to the Mediterranean Sea. Perhaps as a consequence of this visible and obviously significant contribution, previous studies have mainly focused on Northern Africa as the major source of nutrients to the Mediterranean (Escudero et al., 2011; Ganor & Mamane, 1982; Guerzoni et al., 1999). Despite the eastern Mediterranean basin receiving air masses from Europe at least 70% of the time (Kouvarakis, Mihalopoulos, Tselepidis, & Stavrakaki, 2001), phosphorus within European-sourced aerosols has not been as extensively studied due to comparatively lower mass deposition. Yet, it is the composition of the aerosol and the ability of microorganisms to assimilate nutrients from this source, i.e. bioavailability, that must also be considered.

Phosphorus bioavailability has traditionally been linked to the composition and abundance of different chemical phases (Beauchemin et al., 2003; Mackey et al., 2012). Phosphorus is thought to be bioavailable when present as highly soluble inorganic and organic compounds. Assessments of phosphorus bioavailability in aerosols have been

challenged by current analytical limitations. Typically, studies of aerosol phosphorus rely upon sequential chemical extraction or leaching techniques to assess the composition, and therefore the potential bioavailability of phosphorus (Anderson, Faul, & Paytan, 2010; H. Y. Chen, Fang, Preston, & Lin, 2006; Izquierdo et al., 2012; Markaki et al., 2003; Ridame & Guieu, 2002). These techniques have painted a complex picture of aerosol phosphorus composition, showing that phosphorus occurs in a number of different phases including organic, inorganic, and mineral forms, and that these phases can undergo many transformations in response to environmental conditions (Anderson et al., 2010; Baker, Jickells, Witt, & Linge, 2006; H. Y. Chen et al., 2006; Nenes et al., 2011); however, phases used to calibrate extraction methods were developed for soil and marine sediment analysis, thus may not be entirely representative of phosphorus phases found in aerosol. Here we combine novel synchrotron-based techniques with traditional analyses to show that European aerosols contribute phosphorus to the Mediterranean Sea that is vastly different in phosphorus composition and solubility than North African aerosols.

2.3 Methods

2.3.1 Ambient aerosol collection

Air masses originating in North Africa and Europe were sampled at the Finokalia research station (35°32'N, 25°67'E), a remote site on the island of Crete, Greece, located 70 km from the nearest major city. This site was chosen as it is isolated from both local and regional influences (Markaki et al., 2003), making it an ideal location for examining the transport of long range aerosols. Samples of particulate matter with an aerodynamic diameter < 10 µm, PM10, were collected on Teflon filters using a virtual impactor with

an operational flow rate of 16.7 L min^{-1} . Samples were collected over a one to three day period from 2009-2011 during which either North African or European air masses dominated (Table 2.1). A total of fourteen samples were analyzed, five from European and nine from North African air masses (Table 2.1), hereafter referred to as simply European and North African samples. Hybrid Single Particle Lagrangian Integrated Trajectory Model (HYSPLIT) (Draxier & Hess, 1998; Izquierdo et al., 2012) back trajectories were completed for each sample in order to confirm the geographic origin of the air masses sampled. HYSPLIT back trajectories were calculated between 1000 m and 3000 m above ground level for five days preceding sample collection (Kalivitis et al., 2007). Dust is either homogeneously distributed from 0 to about 3000 m, during spring and autumn dust events, or is found in a layer between 2500 – 4000 m during summer and autumn dust events. HYSPLIT back trajectories computed at 1000 m show the origin of air masses within the boundary layer; this height is chosen, rather than the more conventional heights of 0 m or 500 m to avoid orographic problems. HYSPLIT back trajectories were completed for each sample in order to confirm the geographic origin of the air masses sampled (Figure 2.4). While HYSPLIT back trajectories do not guarantee that pure end members were sampled, the air masses were dominated by either North African or European origins. Ambient aerosol samples were stored at -20°C until analysis.

2.3.2 Emission source collection

Emissions from ultra-low sulfur diesel fuel and gasoline were collected using US Environmental Protection Agency protocols under typical urban driving conditions (Oakes, Ingall, et al., 2012). Coal fly ash from an electrostatic precipitator, provided by

The Southern Company, was aerosolized and collected with a PM_{2.5} cyclone inlet sampler (Oakes, Ingall, et al., 2012). Smoke produced from the burning of materials collected from coniferous and deciduous trees native to Georgia, USA, was sampled during a controlled biomass burning experiment using a cyclone inlet sampler placed 3.5 m above the burn area at a flow rate of 16.7 L min⁻¹ for approximately 30 minutes. The ash produced from the biomass burning experiment was also analyzed. Although emission sources were not collected from European or North African locations, source materials presented here are considered to be reasonably similar to those found in Europe and North Africa. Thus, these emission source end members are used as a proxy for primary phosphorus sources found in European and North African air masses. In addition, the following lyophilized commercially-available source materials were analyzed: pollen (*Quercus ruba*; Sigma P7895), the gram-negative pseudomonad bacterium *Azotobacter vinelandii* (Sigma A2135), and the gram-positive spore-forming bacterium *Bacillus subtilis* (Sigma B4006). These commercially available materials were handled and analyzed in the same manner as the phosphorus standards (2.6 Supporting Material). Emission source samples were stored at -20°C until analysis.

2.3.3 Total phosphorus and soluble phosphate determination

Total phosphorus was measured for all samples with a technique employing high temperature combustion (550°C for 2 hours) followed by extraction in acid (1N HCl, agitated for 24 hours) (Aspila, Agemian, & Chau, 1976). The extracts were centrifuged prior to analysis to remove suspended particles. Total phosphorus content was measured using standard spectrophotometric techniques (Murphy & Riley, 1962). Soluble phosphate was determined for all samples collected at the Finokalia research station. For

these samples half of a Teflon filter was extracted by sonicating with 15 ml of nanopure water (Milli-Q, resistivity: 18.2 M Ω -cm) for 45 minutes. It should be noted that sonication could extract organic phosphorus; therefore, this method can overestimate soluble phosphate in a sample. Prior to analysis, each extracted solution was filtered through polyethersulfone membrane (PES) filters (0.45 μ m pore size diameter), to remove suspended particles. A Dionex AS4A-SC column with ASRS-ULTRA-II suppressor in autosuppression mode of operation was used for the analysis of dissolved inorganic phosphate (DIP). The reproducibility of the measurements defined as standard deviation of five consecutive analyses was better than 2%. The detection limit, defined as 3 times the standard deviation of the blank, was 0.06 μ M DIP.

2.3.4 Synchrotron-based X-ray spectromicroscopy

Samples were analyzed on the X-ray fluorescence microscope located at beamline 2-ID-B at the Advanced Photon Source, Argonne National Laboratory. The beamline is optimized to examine samples over a 1-4 keV energy range using a focused X-ray beam with a spot size of approximately 100 nm² (McNulty et al., 2003). Phosphorus Near Edge X-ray Fluorescence Spectroscopy (P-NEXFS) data were collected in two modes that differ based on spatial resolution. In the first mode, individual phosphorus-rich particles with a diameter of greater than 1 micron were identified in X-ray fluorescence maps; these particles were then interrogated with micro P-NEXFS. The individual phosphorus-rich particles seen in X-ray fluorescence maps are obvious contributors to total sample phosphorus. However, much of the total phosphorus on an aerosol filter can also be contained in particles that are less phosphorus-rich and therefore less apparent in X-ray fluorescence maps. Therefore, in the second mode, larger areas of the filters were also

examined with an unfocused beam (spot size = 0.28 mm²) to obtain bulk spectra representative of the average phosphorus phase present.

In order to maximize the number of samples analyzed in the allotted time, X-ray fluorescence maps were created by rastering the focused beam in 0.5 μm steps with an incident energy of 2185 eV. At this resolution, individual phosphorus-rich particles were clearly discernible. PNEXFS spectra were collected over an energy range of 2130 to 2210 eV in 0.33 eV steps, using a 1 s dwell time at each step. P-NEXFS measurements for both bulk and individual phosphorus-rich particles were repeated at least three times, in a single position, creating a minimum effective dwell time of 3 s. X-ray spectromicroscopy data were collected using an energy dispersive silicon drift detector (-Ketec- with a 5 mm² sensitive area). A flow of helium was introduced between the X-ray optical hardware and the sample to reduce X-ray backscatter. An in-line monitor stick composed of fluorapatite was measured with each sample in order to identify and correct for any potential drift in monochromator energy calibration that occurred during analyses (de Jonge et al., 2010). Clean areas of Teflon and cellulose acetate filters were examined as blanks and showed negligible background signal.

P-NEXFS provides essentially the same information as another commonly cited technique, P-XANES (Phosphorus X-ray Absorption Near Edge Structure) spectroscopy. The two techniques differ primarily in the method of signal detection. P-NEXFS uses the X-ray fluorescence signal which is inversely proportional to the absorption signal used in a P-XANES measurement.

2.3.5 P-NEXFS data analysis

Linear combination fitting is an effective tool for the deconvolution of spectra of known mixtures (Ajiboye, Akinremi, & Jurgensen, 2007). Using Athena software (Ravel & Newville, 2005), individual particle and bulk P-NEXFS spectra were fit with previously characterized phosphorus standard materials using a linear combination approach to determine both speciation and relative abundance of phosphorus phases (Jörg Prietzel et al., 2013). Additionally, bulk P-NEXFS spectra of ambient aerosol were fit using emission sources rather than standards; this approach was used to determine if phosphorus in ambient aerosols could be accounted for solely by emission sources. Athena uses a non-linear, least-squares minimization approach to fit spectra of unknown materials with spectra of standard materials and computes an error term, R-factor, to quantify the goodness of fit produced by a particular linear combination of standard P-NEXFS spectra. The linear combination of standards that yielded the lowest R-factor reflect the best fit (Ravel & Newville, 2005).

The data for an individual P-NEXFS spectrum was normalized to create a relative intensity value of approximately 1 for post-edge area of the spectra (> 2160 eV). The data were also processed using a three-point smoothing algorithm built into the software. Smoothing did not appreciably change the data, other than removing high frequency noise. The standard database used in our spectral linear combination fitting included phosphorus minerals and inorganic phosphorus compounds discussed in Ingall et al. (2011), as well as a variety of organic phosphorus compounds (Appendix A). An iterative process was used to refine the standard database used to model the sample spectra. First, complex, high temperature, and high-pressure minerals, unlikely to be major components

of aerosol phosphorus were excluded from the database (Oakes, Weber, et al., 2012). Second, the database was narrowed through elimination of standards with low contribution (i.e. less than 10%) or poor fit (i.e. high R-factor) during initial linear combination fitting. Finally, the composition of individual phosphorus-rich particles determined using micro P-NEXFS helped to guide the choice of standards for the modeling of bulk P-NEXFS spectra.

Spectra can be similar within certain compound classes like phosphorus esters (2.6 Supporting Material Figure 2.6) and mineral classes like apatites (ED Ingall et al., 2011). Also, insufficient quantities of a specific mineral or compound in a sample can also lead to underestimation of the specific compound during linear combination fitting (Dean Hesterberg, 2010). We therefore generalized our results into four chemical classes: apatite, metal phosphates, alkali and alkaline earth metal phosphates, and organic phosphorus + polyphosphate, with distinct implications for phosphorus solubility and bioavailability. The apatite chemical class includes fluorapatite, hydroxyapatite, carbonate fluorapatite, carbonate hydroxyapatite, and chlorapatite. Minerals in the metal phosphate chemical class have a dominant metal cation like iron, copper, or manganese and include vauxite, cornetite, wardite, and wolfeite. Alkali and alkaline earth metal phosphates (hereafter referred to as alkali phosphates) include sodium phosphate and calcium dihydrogen phosphate; these phases typically have high solubility. The final chemical class, organic phosphorus + polyphosphate, includes organic compounds like adenosine-5'-triphosphate (ATP), lipids (and other phosphorus esters), and polyphosphates, all compounds of biological origin.

2.4 Results and Discussion

2.4.1 Ambient aerosols

Aerosol phosphorus from North African air masses was on average $16 \pm 14\%$ soluble. In contrast, aerosol phosphorus from European air masses was on average $54 \pm 6\%$ soluble (Figure 2.1). Despite European-sourced aerosols having less total phosphorus than North African aerosols, the mass of soluble phosphorus per mass of aerosol is comparable (Figure 2.1). Consistent with our findings based on our limited sample set, sequential extraction methods have shown that anthropogenically-influenced

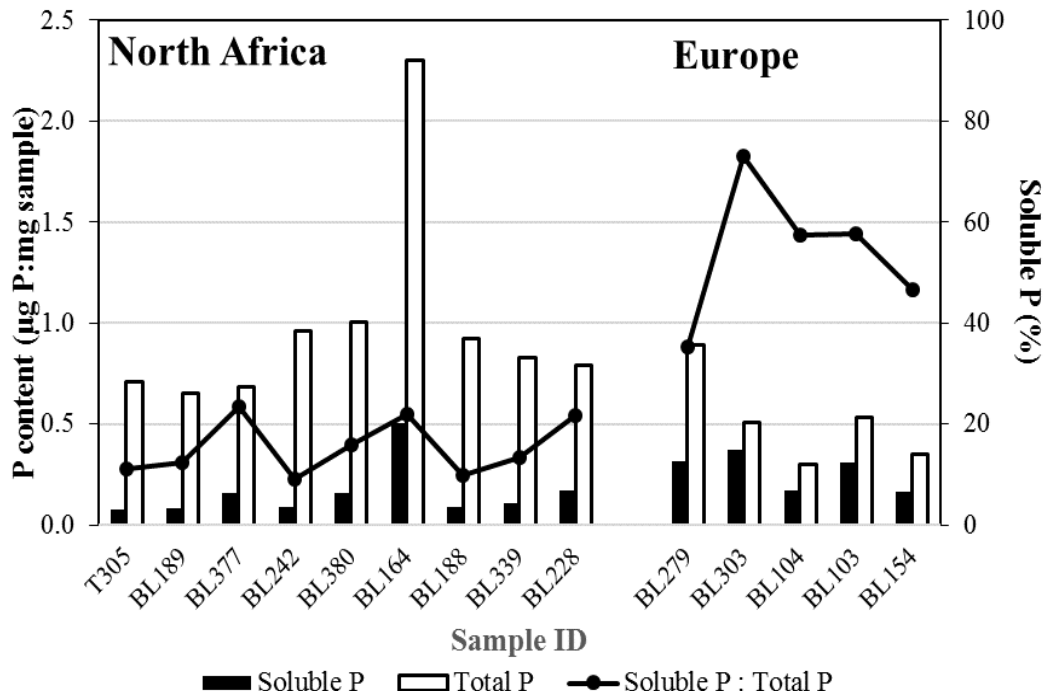


Figure 2.1 Total and soluble Phosphorus of Mediterranean Aerosols Total phosphorus content (white) and soluble phosphorus content (black) show both European and North African samples are potential sources of phosphorus to the Mediterranean Sea. The molar ratio of soluble phosphorus to total phosphorus (line) expressed as a percentage shows European aerosol can be up to 4.7 times more soluble than North African aerosol. Typically, the reproducibility for measuring soluble phosphorus and total phosphorus are 2% and 10%, respectively.

air masses, such as those originating in Europe, tend to have more soluble phosphorus than North African aerosol (Anderson et al., 2010; Izquierdo et al., 2012). Our bulk P-NEXFS measurements further showed that European-sourced aerosols were dominated by the organic phosphorus + polyphosphate chemical class and were on average composed of $94 \pm 14\%$ organic phosphorus + polyphosphate and $6 \pm 14\%$ metal phosphate, with undetectable alkali phosphates or apatite (Figure 2.2). In contrast, the average phosphorus composition of North African-sourced aerosols was $32 \pm 33\%$ apatite, $25 \pm 30\%$ alkali phosphates, $27 \pm 27\%$ organic phosphorus +

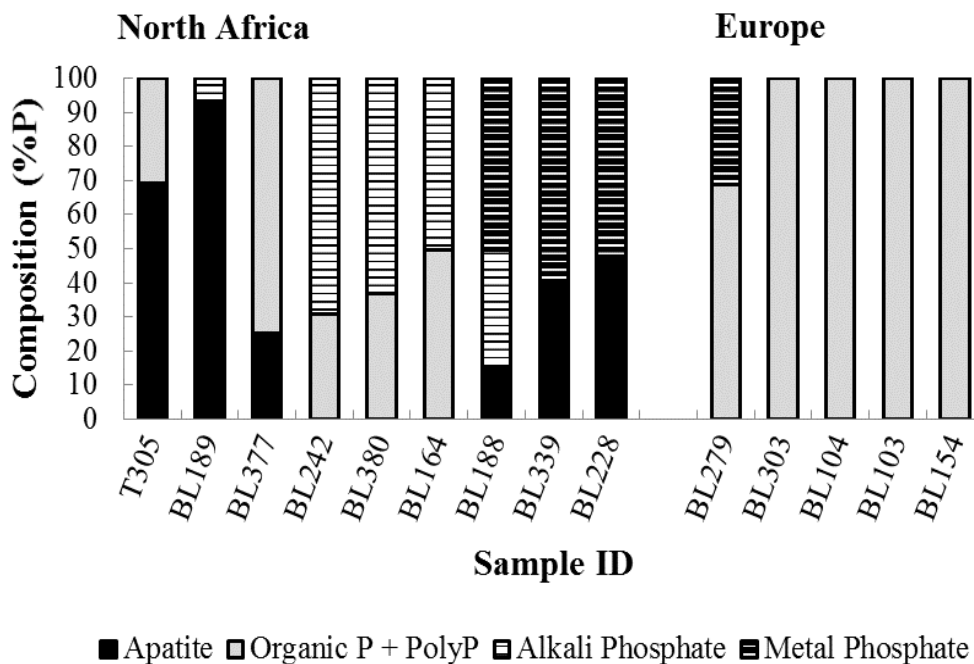


Figure 2.2 Phosphorus Composition of Mediterranean Aerosols Linear combination fitting of each aerosol spectra was used to determine the phosphorus composition in each sample. The distribution of apatite (black), organic phosphorus + polyphosphate (grey), alkali phosphates (white striped), and metal phosphates (black striped) determined through linear combination fitting are shown for each sample.

polyphosphate, and $18 \pm 27\%$ metal phosphate (Figure 2.2). Micro PNEXFS analysis revealed that individual phosphorus-rich particles from European and North African air masses were often solely comprised of organic phosphorus + polyphosphate or apatite, respectively.

Previous studies based on sequential extraction techniques have shown that apatite is the most abundant phosphorus phase followed by oxide-associated phosphorus in North African-sourced air masses (Anderson et al., 2010; Nenes et al., 2011). Our results suggest organic phosphorus + polyphosphate as well as alkali phosphates account for a large fraction of the phosphorus in the North African derived aerosol (Figure 2.2). The oxide-associated phosphorus fraction determined by sequential extraction techniques can include labile organic phosphorus as well (Anderson et al., 2010). Therefore, our finding of organic phosphorus + polyphosphate in North African-sourced aerosols could be consistent with chemical extraction methods and suggests organic phosphorus is present in the oxide-associated fraction identified in these studies. The presence of alkali phosphates in North African air masses may reflect recycling of apatite-derived phosphorus. At low pH, apatite more readily dissolves into aerosol water droplets (Anderson et al., 2010) that are subsequently dehydrated, possibly resulting in supersaturation of these droplets with respect to alkali phosphates. If sulfuric acid is the dominant acidic species present, aerosol water content may continue to be high even at low pH, which further facilitates dissolution of phosphorus.

Soluble phosphorus percentage shows the strongest correlation with the relative abundance of organic phosphorus + polyphosphate (Figure 2.3). However, the correlation coefficient of 0.61 indicates that significant variability in this relationship exists, likely

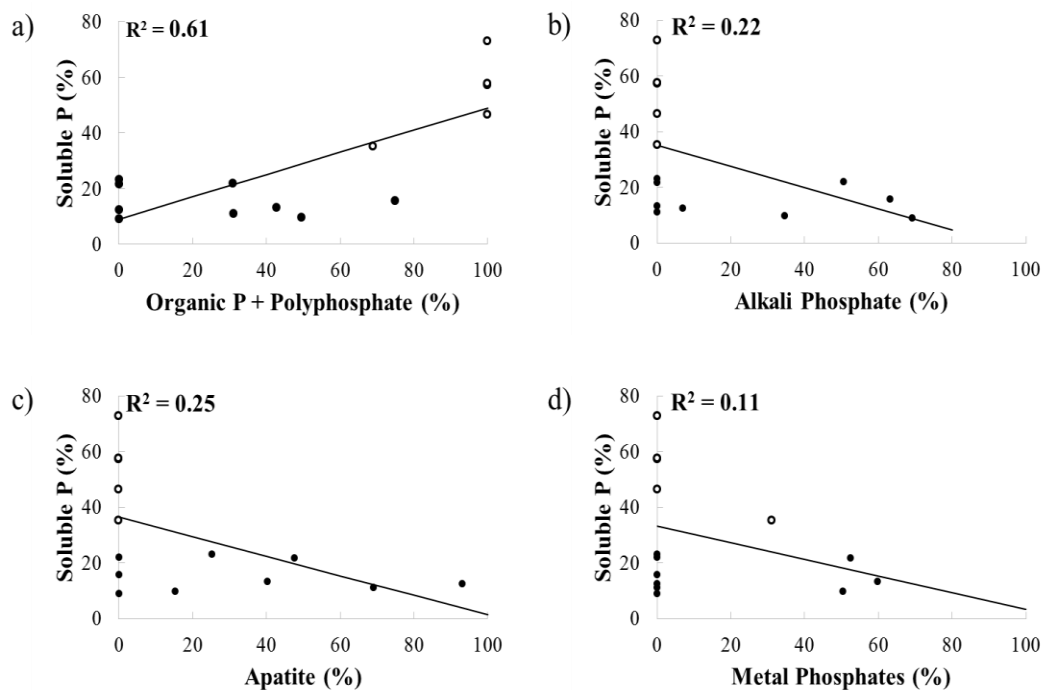


Figure 2.3 Relationship between Phosphorus Composition and Relative Solubility of Phosphorus Plots of percent soluble phosphorus versus phosphorus composition are shown for North African (\circ) and European (\bullet) sourced aerosol samples. The only chemical class showing a notable correlation with solubility is organic phosphorus + polyphosphate (a) suggesting that this class does in part influence solubility.

tied to the abundance and solubility of specific organic phosphorus compounds *within* the defined chemical class. Organic phosphorus compounds exhibit a wide range of structures and compositions that are generally not possible to distinguish with P-NEXFS (2.6 Supporting Material). These species, in turn, differ in terms of phosphorus solubility. Also, acidification of normally insoluble phosphorus phases can increase phosphorus solubility (Nenes et al., 2011). Anthropogenic emissions are well-documented sources of acidic species (Nenes et al., 2011) and have also been linked to more soluble forms of aerosol phosphorus (Izquierdo et al., 2012; Zamora, Prospero, Hansell, & Trapp, 2013). Varying quantities of acidic species (Nenes et al., 2011) entrained in European and North

African air masses would likely lead to different levels of phosphorus solubilization during atmospheric transport.

2.4.2 Emission sources

In addition to ambient aerosol samples, several common emission sources were analyzed with bulk P-NEXFS. Spectral linear combination fitting showed that pollen and the bacteria *Bacillus subtilis* and *Azotobacter vinelandii* were dominated by organic phosphorus + polyphosphate. Coal fly ash, diesel, volcanic ash, and biomass burning ash were comprised of apatite, metal phosphates, and organic phosphorus + polyphosphate. Neither gasoline nor biomass burning emissions showed a discernable phosphorus edge, so phosphorus composition could not be characterized for these sources. Spectral linear combination fits based only on source emission spectra for ambient aerosol samples were usually inferior to fits utilizing phosphorus compounds and minerals. The dissimilarity between source emissions and ambient aerosol suggest either that atmospheric processing strongly modifies phosphorus composition or that another unknown phosphorus source is a dominant aerosol component. For example, aerosol production by plants and other organisms is a possible source of organic aerosol phosphorus (Artaxo et al., 2002; Benitez-Nelson, 2000). Biogenic pathways involved in aerosol production remain uncertain (Artaxo et al., 2002; Benitez-Nelson, 2000); however, primary emissions from vegetative cover could also account for the dominance of organic phosphorus + polyphosphate class seen in European air masses. Microbial cells have also been recognized as an important natural component of aerosol (Bauer et al., 2002; Burrows, Elbert, Lawrence, & Poschl, 2009). Due to a globally ubiquitous distribution (Bauer et al., 2002; Burrows et al., 2009), bacteria are potentially a key contributor to the organic

fractions present in both the North African and European aerosol examined here. In fact, when various emission sources were used as standards in spectral linear combination fitting, fits containing bacteria as a standard produced the best results for ambient aerosols sampled from both North African and European air masses.

2.5 Conclusion

This work demonstrates, based on our limited data set, that synchrotron-based techniques provide valuable insights into the composition and therefore the factors influencing the solubility and bioavailability of phosphorus in aerosols. The distinctively higher phosphorus solubility in European aerosol is attributed largely to the presence of organic phosphorus. Preliminary evidence suggests that this organic phosphorus may be associated with bacteria; however, further research is necessary to specifically characterize the organic phosphorus containing phases and determine the prevalence of bacteria in Mediterranean aerosols. Shifts in wind direction observed over seasonal and inter-annual timescales (Chamard et al., 2003) have been suggested as a key factor controlling the delivery of vital nutrients to marine systems (Hamza, Enan, Al-Hassini, Stuut, & de-Ber, 2011). Climate simulations suggest that European-sourced winds will be more prevalent over the Mediterranean Sea than North African-sourced winds in the future (McInnes, Erwin, & Bathols, 2011). If phosphorus in European aerosols is consistently shown to be 3.5 times more soluble than North African aerosol, then predicted increases European influences will lead to more soluble phosphorus loading to the Mediterranean Sea and ultimately more biological productivity.

2.6 Supporting Material

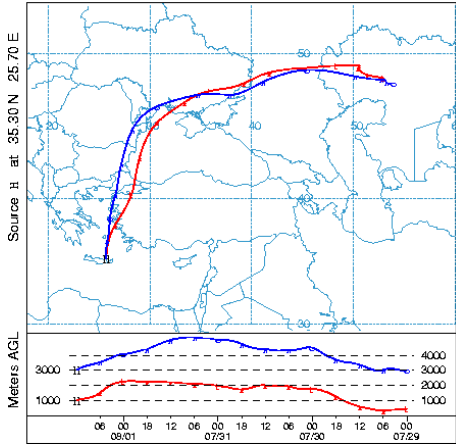
Table 2.1 lists sample collection dates and supporting information for each sample. HYSPLIT back trajectories calculated for each sample were used to determine air mass origin (Figure 2.4).

Table 2.1 Total and soluble phosphorus of PM10 samples collected at Finokalia Research Station

Sample ID	Collection Date	Loading ($\mu\text{g}/\text{m}^3$)	Soluble P (nmol/m^3)	Total P ($\mu\text{mol}/\text{m}^3$)	Air mass Origin
BL - 164	12/17/09	9.9	0.162	0.735	North Africa
BL - 188	2/18/10	100	0.304	3.090	North Africa
BL - 189	2/20/10	140	0.367	2.940	North Africa
BL - 228	5/15/10	82	0.454	2.089	North Africa
BL - 242	6/17/10	63	0.180	1.954	North Africa
BL - 339	1/29/11	57	0.204	1.518	North Africa
BL - 377	4/28/11	91	0.469	2.006	North Africa
BL - 380	5/5/11	77	0.395	2.499	North Africa
T-305	1/23/09	170	0.427	3.809	North Africa
BL - 154	11/24/09	20	0.105	0.227	Europe
BL - 103	8/1/09	23	0.228	0.395	Europe
BL - 104	8/3/09	24	0.132	0.230	Europe
BL - 279	9/19/10	27	0.273	0.776	Europe
BL - 303	11/6/10	22.	0.266	0.365	Europe

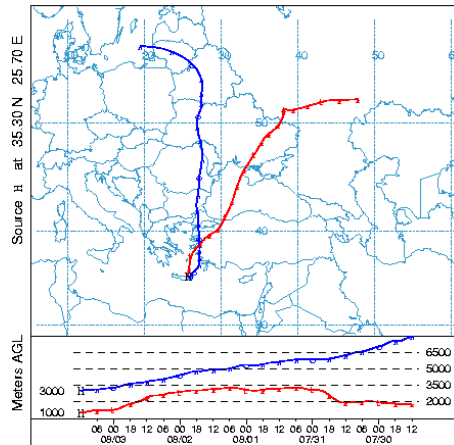
BL103

NOAA HYSPLIT MODEL
Backward trajectories ending at 12 UTC 01 Aug 09
GDAS Meteorological Data



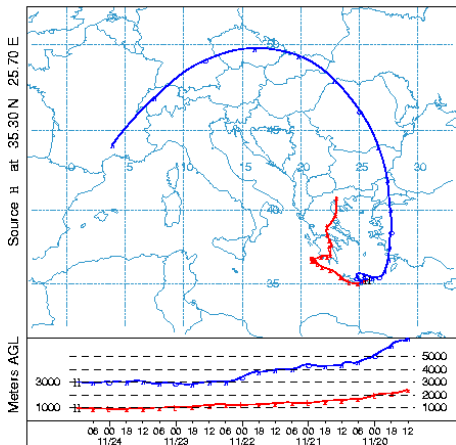
BL154

NOAA HYSPLIT MODEL
Backward trajectories ending at 12 UTC 03 Aug 09
GDAS Meteorological Data



BL104

NOAA HYSPLIT MODEL
Backward trajectories ending at 12 UTC 24 Nov 09
GDAS Meteorological Data



BL279

NOAA HYSPLIT MODEL
Backward trajectories ending at 12 UTC 19 Sep 10
GDAS Meteorological Data

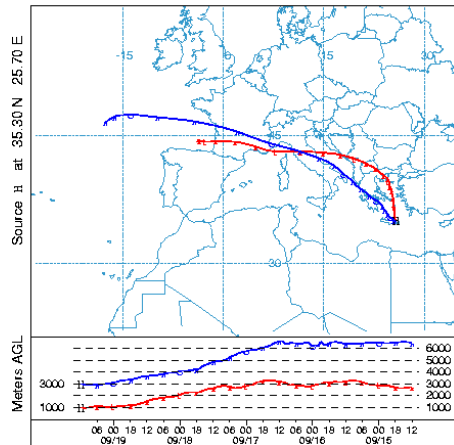
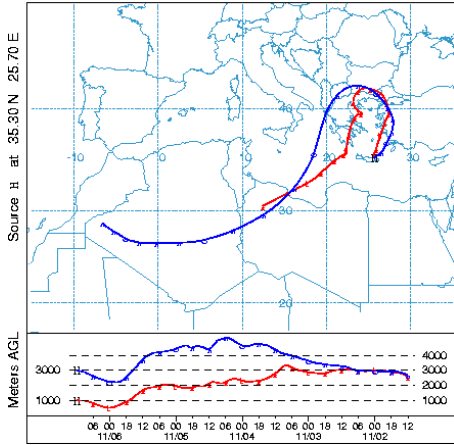


Figure 2.4 HYSPLIT back trajectories for samples showing the European or North African dominance of each sample.

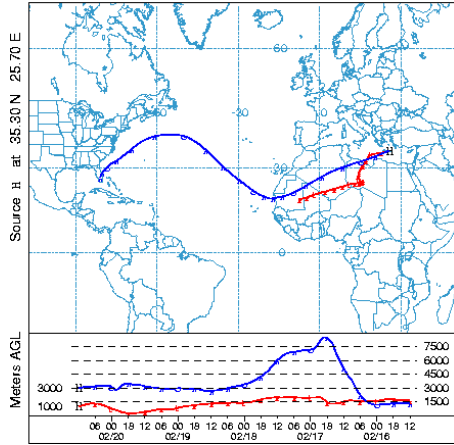
BL303

NOAA HYSPLIT MODEL
Backward trajectories ending at 12 UTC 06 Nov 10
GDAS Meteorological Data



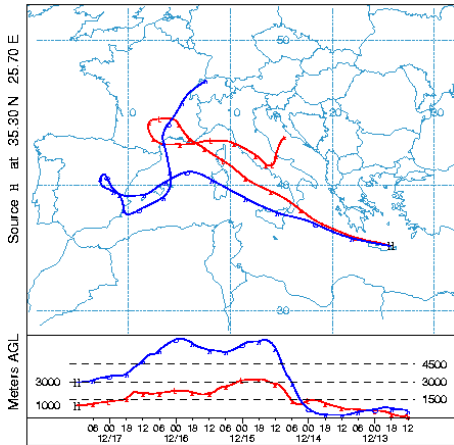
BL189

NOAA HYSPLIT MODEL
Backward trajectories ending at 12 UTC 20 Feb 10
GDAS Meteorological Data



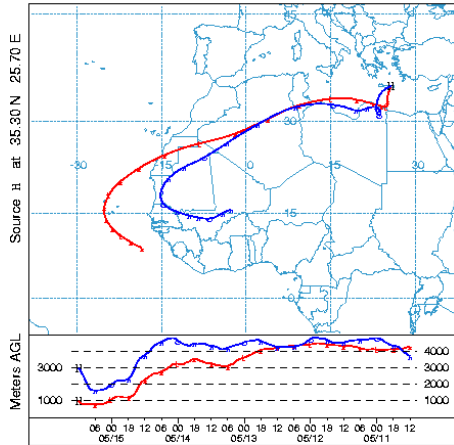
BL164

NOAA HYSPLIT MODEL
Backward trajectories ending at 12 UTC 17 Dec 09
GDAS Meteorological Data



BL228

NOAA HYSPLIT MODEL
Backward trajectories ending at 12 UTC 15 May 10
GDAS Meteorological Data



BL188

NOAA HYSPLIT MODEL
Backward trajectories ending at 12 UTC 18 Feb 10
GDAS Meteorological Data

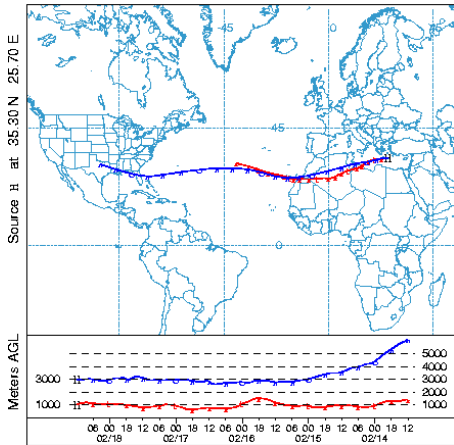
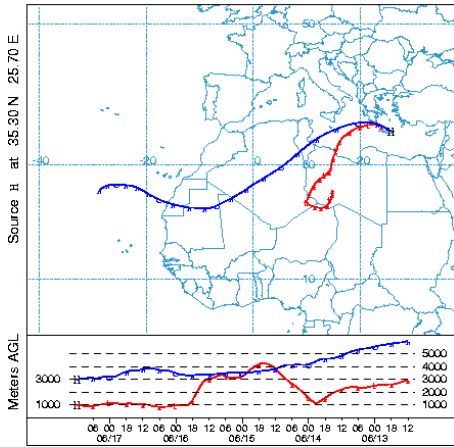


Figure 2.4 continued

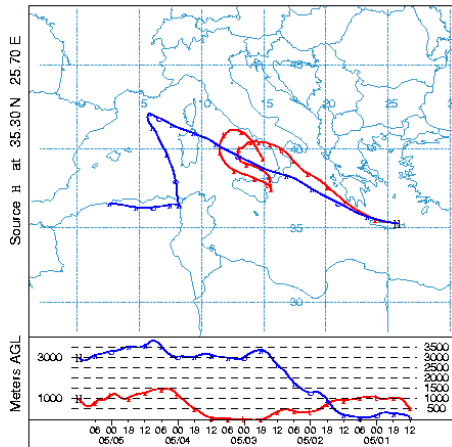
BL242

NOAA HYSPLIT MODEL
Backward trajectories ending at 12 UTC 17 Jun 10
GDAS Meteorological Data



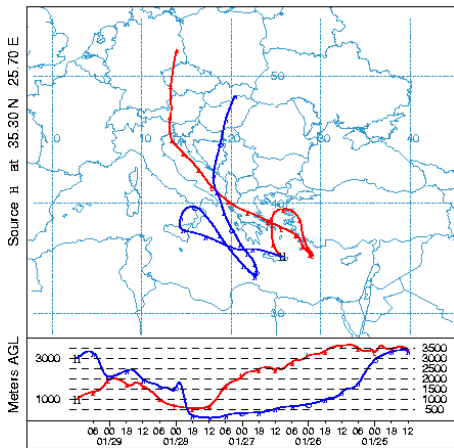
BL380

NOAA HYSPLIT MODEL
Backward trajectories ending at 12 UTC 05 May 11
GDAS Meteorological Data



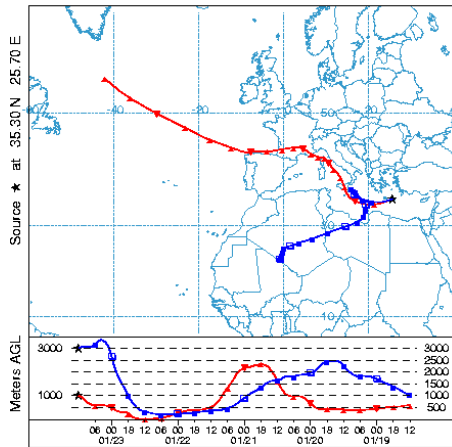
BL339

NOAA HYSPLIT MODEL
Backward trajectories ending at 12 UTC 29 Jan 11
GDAS Meteorological Data



T305

NOAA HYSPLIT MODEL
Backward trajectories ending at 12 UTC 23 Jan 09
GDAS Meteorological Data



BL377

NOAA HYSPLIT MODEL
Backward trajectories ending at 12 UTC 28 Apr 11
GDAS Meteorological Data

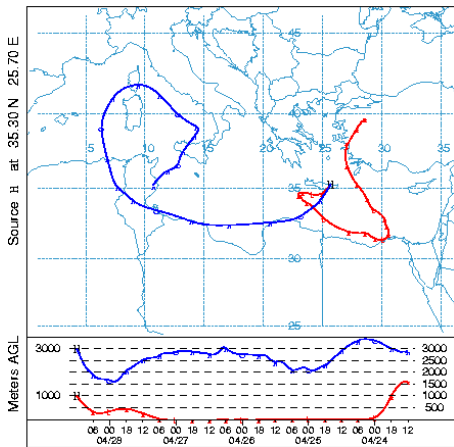


Figure 2.4 continued

Several organic phosphorus compounds were examined with P-NEXFS as standard material (Table 2.2). Samples were mounted onto cellulose acetate filters and prepared for analysis by cutting a 0.5 cm x 0.5 cm portion of filter and mounting the sample across a hole on an aluminum support stick. As shown in Figure S2, organic phosphorus compounds tended to have a relatively featureless post-edge. The lack of distinguishing characteristics does not allow for identification of a specific organic compound through P-NEXFS. Data for organic standards is available in External Database S1.

Table 2.2 Organic Phosphorus compounds and CAS numbers

Organic P compound	CAS
2-aminoethylphosphonic acid	2041-14-7
Ammonium OO-diethyldithiophosphate	1068-22-0
Adenosine-5'-triphosphate	51963-61-2
Glycerol Phosphate	55073-41-1
Hexametaphosphate	68915-31-1
Polyphosphate CL15	-
Sodium tripolyphosphate	7758-29-4
O-Phospho-L-Serine	407-41-0
O-Phosphorylethanolamine	1071-23-4
Phosphotidylcholine	97281-47-5
Phytic Acid	83-86-3

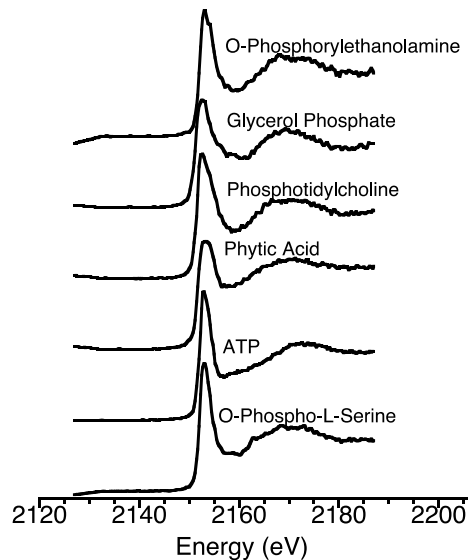


Figure 2.5 Spectra of Several Organic Phosphorus Standards Spectra of several organic P standards. A variety of organic standards all have a sharp peak at 2152 eV, the P k-edge, and a relatively featureless post-edge. As is the case with some mineral groups, the presence of organic P compounds can be detected using spectroscopy, but more detailed chemical identifications are not possible in concentrations typical of natural samples.

CHAPTER 3

COMPOSITION AND OXIDATION STATE OF SULFUR IN ATMOSPHERIC PARTICULATE MATTER

3.1 Abstract

The chemical and physical speciation of atmospheric sulfur was investigated in ambient aerosol samples using a combination of Sulfur Near-Edge X-ray Fluorescence Spectroscopy (S-NEXFS) and X-ray fluorescence (XRF) microscopy. These techniques were used to determine the composition and oxidation state of sulfur in common primary emission sources and ambient particulate matter collected from the greater Atlanta area. Ambient particulate matter samples contained two oxidation states: S^0 and S^{+VI} . Individual particles ($> 1 \mu\text{m}$) contain S^0 in 95% of the individual aerosol particles analyzed. Linear combination fitting revealed that S^{+VI} in ambient aerosol was dominated by ammonium sulfate as well as metal sulfates. The finding of metal sulfates provides further evidence for acidic reactions that solubilize metals such as iron during atmospheric transport. Emission sources including biomass burning, coal fly ash, gasoline, diesel, volcanic ash, and aerosolized Atlanta soil, and the commercially

Longo, A.F., King, L.E., Weber, R.J., Russell, A.G., Vine, D.J., Ingall, E.D. (2016) Composition and oxidation state of sulfur in urban Atlanta aerosols. *Reviewed by selected co-authors and to be submitted to Geophysical Research Letters*

available bacterium *Bacillus subtilis* contained only S^{+VI}. A commercially available *Azotobacter vinelandii* sample contained approximately equal proportions of S⁰ and S^{+VI}. S⁰ in individual aerosol particles most likely originates from primary emission sources such as aerosolized bacteria or incomplete combustion.

3.2 Introduction

Sulfur (S) in atmospheric aerosols has garnered significant interest because of its influence on environmental processes (Bufalini, 1971; Galloway, 1995; Van Grieken, Delalieux, & Gysels, 1998) and human health (Burnett et al., 1995). S-rich aerosol is a source of cloud condensation nuclei, which influences atmospheric visibility through light scattering. On a global scale, cloud formation processes associated with S-rich aerosol change atmospheric albedo (Charlson et al., 1987; Quinn & Bates, 2011), which can ultimately influence global climate. Atmospheric sulfur is also responsible for the production of sulfuric acid, which has been implicated in the solubilization of metals in aerosol (Nenes et al., 2011; Oakes, Ingall, et al., 2012; Sullivan, Guazzotti, Sodeman, & Prather, 2007; Wiederhold et al., 2006). Solubilization of recalcitrant mineral phases during atmospheric transport can release nutrient elements, such as iron, which impacts biological productivity in many ocean regions (Jickells et al., 2005; Longo et al., 2014; Mahowald et al., 2005). Cloud nucleation and acid production associated with aerosol sulfur are a function of not only concentration, but also composition and oxidation state. Thus, characterization of the composition and oxidation state of sulfur in aerosol is key to understanding atmospheric transformation processes.

The range of sulfur oxidation states as well as organic and inorganic forms present in typical samples confound characterization of aerosol sulfur. Characterization approaches including ion chromatography, X-ray fluorescence, and inductively coupled plasma mass spectrometry have been used to quantify bulk elemental concentrations, which can be used to infer the composition of sulfur in aerosols. However, these techniques cannot determine the oxidation state or directly identify the chemical form of aerosol sulfur. Several studies have demonstrated the effectiveness of synchrotron-based sulfur X-ray absorption near-edge structure (XANES) and the closely related sulfur near-edge X-ray fluorescence spectroscopy (NEXFS) to determine the oxidation state and chemical form of sulfur in environmental samples (Farges, Keppler, Flank, & Lagarde, 2009; Morra et al., 1997; J. Prietzel et al., 2011; Solomon, Lehmann, & Martinez, 2003); however, the application of these techniques to ambient aerosol samples has largely been limited to studies characterizing a few ambient aerosol samples that aim to explore the feasibility and limits of applying XANES and NEXFS to aerosol sulfur studies (Cozzi et al., 2009; Higashi & Takahashi, 2009; Pongpiachan, Thumanu, Kositanont, et al., 2012; Pongpiachan, Thumanu, Na Pattalung, et al., 2012; Y. Takahashi et al., 2006).

Consistent with traditional techniques, synchrotron-based XANES studies indicate that sulfur occurs primarily in the S^{+VI} oxidation state, largely, as inorganic sulfate compounds. Primary emission sources of S^{+VI} include both anthropogenic and biogenic sources, including combustion of fossil fuels, biomass burning, volcanoes, and sea spray (Querol et al., 2000). Reduced sulfur in aerosol has also been identified in smaller quantities through the use of XANES techniques (Cao, Li, Jiang, & Hu, 2015;

Cozzi et al., 2009; Craig, Harker, & Novakov, 1974; Eatough et al., 1978; Higashi & Takahashi, 2009; Huggins, Shah, Huffman, & Robertson, 2000). Primary sources of reduced sulfur to the atmosphere are mainly attributed to gaseous emissions from volcanic gases, hot springs, bacteria, vehicle exhaust, and oil refineries (Andersson, Hegazi, & Roberz, 2006; Cozzi et al., 2009). While detected in the solid phase, reduced sulfur in aerosols has not been extensively studied. Reduced aerosol sulfur may reflect a contribution from primary emission sources or may result from condensation of volatile reduced sulfur gaseous phases, but the ultimate origin of reduced S in aerosol particulates remains unresolved.

Here we use S-NEXFS to investigate the composition and oxidation state of sulfur in ambient aerosols and common primary emission source samples. Previous S-NEXFS studies characterized a limited number of ambient aerosol samples in bulk, providing an average view of the sulfur oxidation state and composition in particulate matter (Higashi & Takahashi, 2009; Long et al., 2014; Pongpiachan, Thumanu, Kositanont, et al., 2012; Pongpiachan, Thumanu, Na Pattalung, et al., 2012; Y. Takahashi et al., 2006). Recent studies of aerosol iron and selenium have demonstrated that analyzing compositional differences between large particles ($> 1 \mu\text{m}$) and the bulk sample can help elucidate aerosol sources and transformations (De Santiago et al., 2014; Oakes, Weber, et al., 2012). Following a similar approach, we used a combination of bulk and individual particle S-NEXFS analyses to characterize aerosol sulfur in diverse rural and urban samples and from different emission sources. The spatial distribution of sulfur oxidation states was also characterized in individual particles by mapping particles at different

incident energies to gain further insights into the processes surrounding the formation of reduced sulfur species in aerosol.

3.3 Methods

3.3.1 Ambient aerosol collection

PM_{2.5} samples were collected from urban and rural locations in and around Atlanta, GA. The five sampling sites, South DeKalb, Fire Station 8, Jefferson Street, Yorkville, and Fort Yargo State Park, are part of the ongoing study Assessment of Spatial Aerosol and Composition in Atlanta (Butler, Andrew, & Russell, 2003). Samples were collected on Zefluor filters over 24-h periods at a flow rate of 16.7 L min⁻¹ using cyclone inlet samplers (URG, Chapel Hill, NC). The multichannel particle samplers were mounted approximately 2.5 m off the ground. Three samples were collected from Yorkville (33°55'42.3"N, 85°2'43.68"W), a rural background site for the Atlanta area. Two samples were collected from Jefferson Street (33°46'38.94"N, 84°24'59.58"W), an urban background collection site, which is not immediately influenced by any individual source or roadside traffic. Five samples were collected from Fort Yargo State Park (33°58'4.18"N, 83°43'29.16"W), a rural setting that is frequently impacted by biomass burning plumes and power plant emissions. Four samples were collected in South DeKalb, a mixed commercial–residential area, approximately 8 km from a major interstate (33°41'16.48"N, 84°17'25.26"W). Eight samples were collected from Fire Station 8, located in an industrial area within close proximity to a rail yard, a fire station, and an intersection with heavy diesel truck traffic (33°48'6.01"N, 84°26'8.75"W) (3.6 Supporting Material Table 3.1).

3.3.2 Emission source collection

PM_{2.5} samples were collected from gasoline and diesel exhaust, biomass burning, and coal fly ash (Oakes, Ingall, et al., 2012). Emissions from ultralow sulfur diesel fuel running a 10.8 L engine and conventional gasoline fuel running a 3.3 L engine were collected according to US Environmental Protection Agency protocols under typical urban driving conditions (Oakes, Ingall, et al., 2012). Polydisperse coal fly ash, provided by The Southern Co., from an electrostatic precipitator of a midsized power plant was aerosolized and collected with a cyclone inlet sampler to separate the PM_{2.5} fraction (Oakes, Ingall, et al., 2012). Smoke produced from the burning of materials collected from coniferous and deciduous trees native to Georgia, USA, was sampled during a controlled biomass burning experiment using a cyclone inlet sampler placed 3.5 m above the burn area at a flow rate of 16.7 L min⁻¹ for approximately 30 min. The ash produced from the biomass burning experiment was analyzed in the same manner. The above primary emission source samples were collected on polytetrafluoroethylene (Zefluor) filters (Longo et al., 2014). In addition, two commercially available bacteria samples, *Azotobacter vinelandii* (Sigma A2135) and *Bacillus subtilis* (Sigma B4006), were homogenized with agate mortar and pestle and mounted on a cellulose acetate filter for analysis.

All samples were stored in clean Petri dishes at -20 °C until analysis. Preparation for synchrotron analyses consisted of mounting an approximate 0.5 cm × 0.5 cm section of ambient aerosol and primary emission source filters over a slot on an aluminum support.

3.3.3 Sulfate standards

In order to create a database of inorganic sulfate standards necessary for data analysis described below, ten compounds were analyzed using the same experimental setup and synchrotron system as the ambient aerosols. These standards included, ammonium sulfate (CAS 7783-20-2), barite, copper(II) sulfate (CAS 7758-98-7), gypsum, iron ammonium sulfate (CAS 7783-85-9), iron(III) sulfate (CAS 15244-10-7), jarosite ($\text{KFe}^{3+}_3(\text{OH})_6(\text{SO}_4)_2$), magnesium sulfate (CAS 7487-88-9), potassium sulfate (CAS 7778-80-5), and sodium sulfate (CAS 7757-82-6). All standards were homogenized with an agate mortar and pestle and mounted on a cellulose acetate filter for analysis. A database of sulfate standards is provided in Appendix A.

3.3.4 Synchrotron-based spectromicroscopy

Samples were analyzed on the X-ray fluorescence microscope located at beamline 2-ID-B at the Advanced Photon Source, Argonne National Laboratory. The beamline is optimized to examine samples over a 1–4 keV energy range using a focused X-ray beam with a spot size of approximately 100 nm^2 (McNulty et al., 2003). Sulfur near-edge X-ray fluorescence spectroscopy (S-NEXFS) data were collected in two modes that differ based on spatial resolution. In the first mode, individual sulfur-rich particles with a diameter of greater than $1 \text{ }\mu\text{m}$ were identified in X-ray fluorescence maps; these particles were then interrogated with micro S-NEXFS. The individual sulfur-rich particles seen in X-ray fluorescence maps are obvious contributors to the total sample sulfur. However, much of the total sulfur on an aerosol filter with a PM2.5 inlet can also be contained in particles that are smaller than $1 \text{ }\mu\text{m}$ or less sulfur-rich and therefore less apparent in X-

ray fluorescence maps. Therefore, in the second mode, large areas of the filters were also examined with an unfocused beam (spot size = 0.28 mm

In order to maximize the number of samples analyzed in the allotted time, X-ray fluorescence maps were created for a subset of samples by rastering the focused beam in 0.5 μm steps with an incident energy of 2535 eV. At this resolution, individual sulfur-rich particles were clearly discernible. S-NEXFS spectra were scanned a 50 eV range centered at 2485 eV in 0.33 eV steps, using a 1 s dwell time at each step. Each S-NEXFS measurements for both bulk and individual sulfur-rich particles were repeated at least 3 times, in a single location, creating a minimum effective dwell time of 3 s. X-ray spectromicroscopy data were collected using an energy dispersive silicon drift detector (Ketek with a 5 mm² sensitive area). A flow of helium was introduced between the X-ray optical hardware and the sample to reduce X-ray backscatter. An in-line monitor stick coated with a zinc sulfate standard was measured with each sample in order to identify and correct for any potential drift in monochromator energy calibration that can occur during analyses (de Jonge et al., 2010)). Clean areas of filter were examined as blanks and showed negligible background signal.

S-NEXFS provides essentially the same information as another commonly cited technique, S-XANES (sulfur X-ray absorption near-edge structure) spectroscopy. The two techniques differ primarily in the method of signal detection. S-NEXFS uses the X-ray fluorescence signal, which is inversely proportional to the absorption signal used in a XANES measurement.

Additionally, XRF microscopy was conducted in two fashions. In the first, an incident energy of 2535 eV was used, and samples were raster through the focused beam in 0.5 μm steps, as mentioned above. At this incident energy, all the sulfur present in the sample will be captured. For the second XRF microscopy experiments, the incident energy was altered to capture images of different sulfur oxidation states in particulate matter. This was accomplished by choosing whitenline energies along the S-NEXFS spectrum. Here, incident energies of 2471 eV and 2480 eV were used to capture S^0 and $\text{S}^{+\text{VI}}$, respectively. XRF maps were created at incident energies of 2471 eV and 2480 eV to capture S^0 and $\text{S}^{+\text{VI}}$, respectively. XRF maps were completed in 0.3 μm spatial resolution and 0.5s dwell time per pixel. X-ray focusing was adjusted to maintain a consistent beam spot size at both energies, however some shift in the final image did occur. The images were aligned using the stack registration function of the Fiji software (Schindelin et al., 2012)).

3.3.5 Data analysis

S-NEXFS data were normalized to create a relative intensity value of approximately 1 for post edge area of the spectra. The data was also processed using a three-point smoothing algorithm built into the software package Athena to remove high frequency noise (Ravel & Newville, 2005). The relative contribution of each oxidation state can be determined by assuming the entire area under the whitenline peaks is representative of total sulfur, and the area under each whitenline peak represents the relative contribution of each oxidation state (Huffman et al., 1991; Xia et al., 1998). The area under the whitenline peaks was determined using the Gaussian peak fitting function of Athena (Ravel & Newville, 2005). Because of the relatively low contribution of other

sulfur oxidation states, only sulfur species containing S^{+VI} oxidation state could be further characterized via linear combination fitting. Linear combination fitting is an effective tool for the deconvolution of spectra of known mixtures (Huffman et al., 1991; Long et al., 2014; Longo et al., 2014; J. Prietzel et al., 2011; Solomon et al., 2003). Using Athena software, individual particle and bulk S-NEXFS spectra were fit with previously characterized sulfate standard materials using a linear combination approach to determine both speciation and relative abundance of sulfate phases (Ravel & Newville, 2005). Athena uses a nonlinear, least square s minimization approach to fit spectra of unknown materials with spectra of standard materials and computes an error term, *R* factor, to quantify the goodness of fit produced by a particular linear combination of standard S-NEXFS spectra. The linear combination of standards that yielded the lowest *R* factor reflects the best fit (Ravel & Newville, 2005).

3.4 Results

3.4.1 Oxidation state of sulfur

Azotobacter vinelandii, *Bacillus subtilis*, gasoline and diesel exhaust, biomass burning, and coal fly ash were only characterized at the bulk level (approximately 0.28 mm² filter area). These common primary emission sources, with the exception of one bacteria sample, contained sulfur solely in the S^{+VI} oxidation state. *Azotobacter vinelandii* was the only emission source that contained both oxidized and reduced sulfur, with approximately 44% S^{+VI} and 56% S⁰ (Figure 3.1).

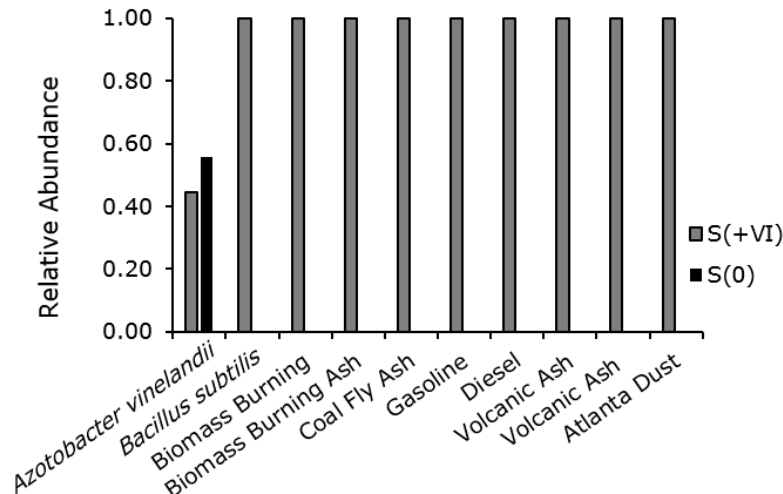


Figure 3.1 The Oxidation State of Sulfur in Common Emission Sources Common emission sources were dominated by S^{+VI} . Only *Azotobacter vinelandii* contained S^0 and S^{+VI} .

At the bulk level, the oxidation state of sulfur in ambient PM_{2.5} samples is dominated by S^{+VI} ; only two samples from South DeKalb contain S^0 , at quantities of less than 10% total sulfur (Figure 3.2a). In contrast, individual particles with aerodynamic diameters of greater than 1 μm consistently contain both S^{+VI} and S^0 (Figure 3.2b). Only one out of twenty-three individual particles analyzed did not contain S^0 . At Fire Station 8 and Jefferson Street, the individual particles sampled contain on average 10% S^0 . Individual particles from South DeKalb average only 4% S^0 . The rural individual particles sampled from Fort Yargo and Yorkville contain on average 5% and 9% S^0 , respectively. Multi-energy maps revealed that S^{+VI} was present throughout the aerosol particle. Often the highest concentration of S^{+VI} was in the center of the particle, where the most mass is present (3.6 Supporting Material Figure 3.4).

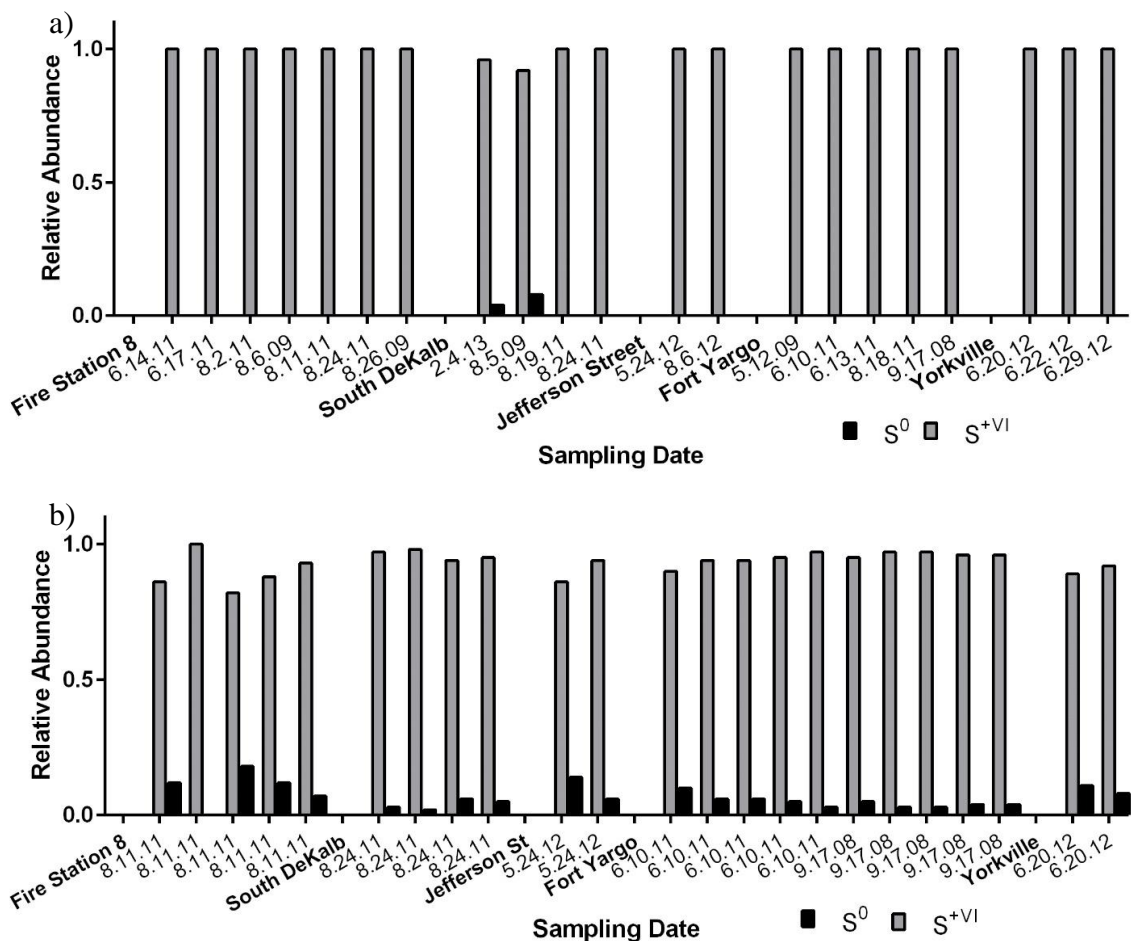


Figure 3.2 Sulfur Oxidation State of Bulk Aerosol and Individual Aerosol Particles
 The oxidation state of sulfur was examined in bulk aerosol (a) and individual particles (b) from a subset of samples. The fractional relative abundance of S^0 (black) and S^{+VI} (grey) is shown for each sample or particle interrogated with S-NEXFS. Bulk samples are dominated by S^{+VI} . At the individual particle level, sulfur is consistently seen at both the S^0 and S^{+VI} oxidation states.

The spatial distribution of S^0 was more varied. In some cases, the S^0 was concentrated in the center of the particle with a less prominent ring on the outside of the particle. In other cases, the S^0 was most concentrated in only one area of the particle (3.6 Supporting Material Figure 3.4).

3.4.2 Sulfate composition

The relative contribution of different sulfur species can be determined by the deconvolution of S-NEXFS spectra with linear combination fitting (J. Prietzel et al., 2011; Ravel & Newville, 2005). In these samples, only S^{+VI} could be further characterized through linear combination fitting because it was by far the most abundant species of sulfur present in the samples. The regions of the S-NEXFS spectra represented by the lower sulfur oxidation states did not possess sufficient detail to yield compositional information. Because of spectral similarities between various metal sulfates, linear combination fits using copper(II) sulfate or iron(III) sulfate often yielded fits with similar R factors. This makes the absolute determination of metal sulfate composition difficult, thus, iron(III) sulfate, copper(II) sulfate, and jarosite are referred to collectively as metal sulfates. The specific compositional information derived from the best linear combination fits, i.e. iron(III) sulfate, copper(II) sulfate, or jarosite, is presented in Table 3.2 and 3.3 (Section 3.6), and suggests that a combination of iron and copper sulfates are likely present in these samples.

In common primary emission sources and ambient PM_{2.5}, S^{+VI} corresponded to sulfate aerosol. In emission sources, only biomass burning, coal fly ash, and diesel exhaust had robust enough signals to characterize specific sulfate composition, and each source had a unique sulfate composition (Table 3.3). Biomass burning contained potassium sulfate ($100 \pm 0.005\%$).

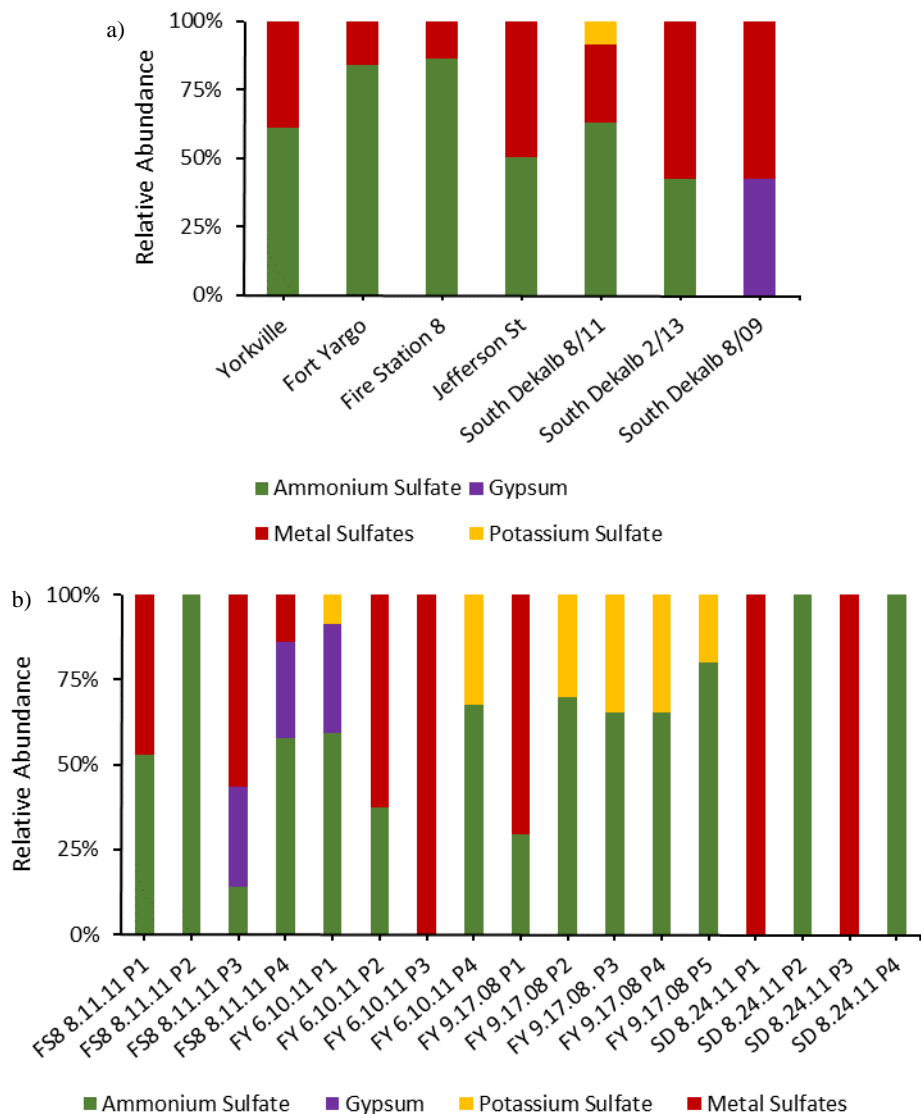


Figure 3.3 Bulk and Individual Particle Sulfate Composition For bulk samples (a), the composition of sulfate was consistent for all samples within a particular sampling location, with the exception of South DeKalb. These samples had three different compositional groups, and the month and year of collection are provided next to the samples. For individual particles (b), the sulfate composition was able to be determined for samples from Fire Station 8 (FS8), Fort Yargo (FY), and South DeKalb (SD). Different particles from the same samples are numbered sequentially (P1-P5).

Coal fly ash contained gypsum ($100 \pm 0\%$), the mineral form of calcium sulfate. Diesel exhaust contains ammonium sulfate ($70 \pm 11\%$) and metal sulfate ($30 \pm 12\%$).

The composition of sulfate was generally consistent within a sampling location (Table 3.3 and Figure 3.3). At the bulk level, rural sampling locations contain a mix of ammonium sulfate and metal sulfate. Yorkville samples is comprised of $61 \pm 9\%$ ammonium sulfate and $39 \pm 9\%$ metal sulfate, and Fort Yargo samples contains $84 \pm 7\%$ ammonium sulfate and $16 \pm 7\%$ metal sulfate. Bulk urban samples all contain a large fraction of ammonium sulfate. Samples from Fire Station 8 contain ammonium sulfate ($84 \pm 7\%$) mixed with metal sulfate ($14 \pm 16\%$), and Jefferson Street contains ammonium sulfate ($51 \pm 8\%$) combined with metal sulfate ($50 \pm 10\%$). South DeKalb has three different compositional groups at bulk level: (1) ammonium sulfate ($63 \pm 7\%$), metal sulfate ($29 \pm 6\%$), and potassium sulfate ($8 \pm 13\%$); (2) ammonium sulfate ($42 \pm 14\%$) and metal sulfate ($58 \pm 14\%$); and (3) gypsum ($43 \pm 15\%$) and metal sulfate ($58 \pm 15\%$).

Only individual particle S-NEXFS spectra from Fire Station 8, Fort Yargo, and South DeKalb contained enough sulfur to determine the sulfate composition (Table 3.3 and Figure 3.3). In total, 17 individual particle S-NEXFS spectra were used to gain insights on the sulfate composition of ambient PM_{2.5}. Consistent with the bulk results, individual particles sampled from Fire Station 8 are largely ammonium sulfate and metal sulfate, with the remainder made of gypsum. Individual particles from South DeKalb contain either ammonium sulfate or metal sulfate. Individual particles from Fort Yargo contain a mixture of mostly ammonium sulfate and potassium sulfate with additional contributions from metal sulfate and gypsum. Spectral signals of samples from Jefferson

Street and Yorkville were not strong enough to characterize the composition of sulfate in the ambient PM_{2.5} samples.

3.5 Discussion

Ammonium sulfate and gypsum are commonly identified phase in studies of aerosol sulfate composition (Higashi & Takahashi, 2009; Long et al., 2014; Y. Takahashi et al., 2006). Consistent with these studies, ammonium sulfate was found across all urban and rural sampling locations, and either ammonium sulfate or gypsum were a major constituent of all bulk samples. At the individual particle level, ammonium sulfate was also a primary contributor to sulfate composition; however, potassium and metal sulfates became more apparent. Our results showed that the sulfate in biomass burning was dominated by potassium sulfate, which suggests biomass burning may be the primary source of the potassium sulfate in ambient aerosol samples. Potassium is often used as a tracer for biomass burning in source apportionment studies (Viana et al., 2008), which show that biomass burning can contribute up to 40% of total PM_{2.5} in Georgia's spring months and 10% of total PM_{2.5} in Georgia's summer months (Tian et al., 2009). Organosulfates have recently been identified as a significant component of sulfate aerosol (Schmitt-Kopplin et al., 2010; Surratt et al., 2008; L. Xu et al., 2015). In this study, organosulfates were not identified as a constituent of sulfate aerosol; however, the concentrations organosulfates are expected to occur at in ambient aerosol could be below the detection limit of NEXFS techniques (Longo et al., 2014; Oakes, Ingall, et al., 2012; Oakes, Weber, et al., 2012).

Metal sulfates were identified as a constituent of all the bulk ambient particulate matter samples and 53% of individual particle spectra. Linear combination fitting of S-NEXFS spectra suggests that iron(III) sulfates are an important group of metal sulfates in ambient Atlanta aerosol (Table 3.2 & 3.3). Furthermore, an Fe-XANES study of ambient Atlanta particulate matter identified iron(III) sulfates, which accounted for approximately 20% of the total iron (Oakes, Ingall, et al., 2012). Iron sulfate represent a very soluble, bioavailable, form of iron that has been found in ambient aerosol (R. C. Moffet et al., 2012; Oakes, Ingall, et al., 2012; Schroth, Crusius, Sholkovitz, & Bostick, 2009; G. H. Zhang et al., 2014). Diesel exhaust was the only primary emission source to contain metal sulfates in this study, and because source apportionment studies only show diesel emissions accounting for 5.3% of total PM_{2.5} in Atlanta (Hu et al., 2014), it is unlikely that diesel exhaust alone can explain the quantities of metal sulfates found in our ambient aerosol samples. Iron sulfate may also be the end product of acidic reactions hypothesized to occur in the atmosphere that are responsible for solubilizing iron. Correlations between the sulfur content and iron solubility have previously been used to suggest this mechanism plays a role in shaping the composition of iron in ambient Atlanta aerosol (Oakes, Ingall, et al., 2012). Briefly, sulfuric acid solubilizes more crystalline iron phases resulting in a solution rich in soluble iron and sulfate that can become internally mixed and potentially precipitate out as iron(III) sulfate (R. C. Moffet et al., 2012; Oakes, Ingall, et al., 2012; G. H. Zhang et al., 2014). Evidence of similar processes has been found for copper (Fang, Guo, Verma, Peltier, & Weber, 2015), which is another metal that is likely in these samples (Table 3.2 and Table 3.3; 3.6 Supporting

Material). The metal sulfates seen in ambient Atlanta aerosol are likely the product of both primary emission sources as well as secondary acidic reactions.

In the multi-energy maps, S^0 always occurs with S^{+VI} (Figure 3.4), suggesting they are either co-emitted as a primary source or linked by a secondary formation process that occurs in the atmosphere. Up to 20% of the sulfur in individual particles was in reduced form, as S^0 . Previous examinations of ambient aerosol have reported less than 5% of total sulfur as reduced sulfur (Cozzi et al., 2009; Long et al., 2014) and have suggested incomplete combustion or incinerator emissions as the likely source (Andersson et al., 2006; Bao et al., 2009; Matsumoto et al., 2006). Common primary emission sources, such as gasoline and diesel exhaust, coal fly ash, and biomass burning, did not contain S^0 as a readily identifiable constituent in bulk S-NEXFS spectra, leaving the source of reduced S in ambient Atlanta aerosol unresolved. Here, bulk S-NEXFS of *Azotobacter vinelandii* revealed this bacterium to be the only analyzed potential emission source to be enriched in S^0 . Microbial cells are increasingly recognized as an important natural component of aerosol (Bauer et al., 2002; Burrows et al., 2009). The ubiquitous distribution of bacteria makes aerosolized soil bacteria, such as *Azotobacter vinelandii*, another potential primary source of S^0 . Furthermore, S^0 was commonly found in individual particles, which constitute the largest particle size fraction of these samples ($>1 \mu\text{m}$). This could further support the hypothesis that the S^0 is from aerosolized soil bacteria, which would reside in larger particles.

The reduced sulfur found in ambient aerosol particles could also be a result of secondary formation processes that occur in the atmosphere. The finding of S^{+IV} in ambient particle matter has been attributed to the absorption and incorporation of sulfur

dioxide (S^{+IV}) onto atmospheric particulate matter (Higashi & Takahashi, 2009).

Theoretically, a similar mechanism could help explain the finding of S^0 in ambient aerosols, however, gaseous phases of reduced sulfur compounds are unlikely to absorb onto an aerosol surface or condense without undergoing oxidation (Alexander, Park, Jacob, Li, & Yantosca, 2005; Liao et al., 2003). Furthermore, reduced sulfur species on the surface of a particle would be easily oxidized by ozone, oxygen, or the hydroxyl radical, suggesting that only reduced sulfur inside of a heterogeneous particle would be likely to survive (Long et al., 2014), suggesting that the S^0 likely has a primary source.

The composition and oxidation state of sulfur in ambient aerosol provides insights for the atmospheric chemistry involving sulfur as well as metals. More than 25% of the bulk sulfate composition can be attributed to metal sulfates, which cannot be accounted for by primary sources alone (Hu et al., 2014). The solubilization of metals with sulfuric acid during atmospheric transport likely plays a role in the forming the metal sulfates observed in this study as well as others (Oakes, Ingall, et al., 2012). Reduced sulfur was also found to account for up to 20% of the total sulfur in individual particles, which is a higher quantity than typically observed in ambient aerosol samples (Cozzi et al., 2009; Long et al., 2014). As is the case with previous studies that have noted reduced sulfur in ambient aerosol samples, the S^0 is likely from a primary emission source. Incomplete combustion is the most commonly cited source of reduced sulfur compounds found in aerosol (Andersson et al., 2006; Bao et al., 2009; Cozzi et al., 2009; Long et al., 2014; Matsumoto et al., 2006); however, in this study, a bacterium was the only potential primary emission source to contain S^0 at the bulk level. This suggests that aerosolized bacteria may contribute to the S^0 seen in ambient Atlanta aerosol.

3.6 Supporting Materials

Table 3.1 Summary of ambient PM_{2.5} collection

Location	Description	Date	No. of Individual Particles Examined
Fire Station 8	Urban	8.6.09	-
		8.26.09	-
		6.14.11	-
		6.17.11	-
		8.2.11	-
		8.11.11	5
		8.24.11	-
South DeKalb	Urban	8.5.09	-
		8.19.11	-
		8.24.11	4
		2.4.13	-
Jefferson Street	Urban	5.24.12	2
	Background	8.6.12	-
Fort Yargo	Rural	9.17.08	5
		5.12.09	-
		6.10.11	5
		6.13.11	-
		8.18.11	-
Yorkville	Rural Background	6.20.12	2
		6.22.12	-
		6.29.12	-

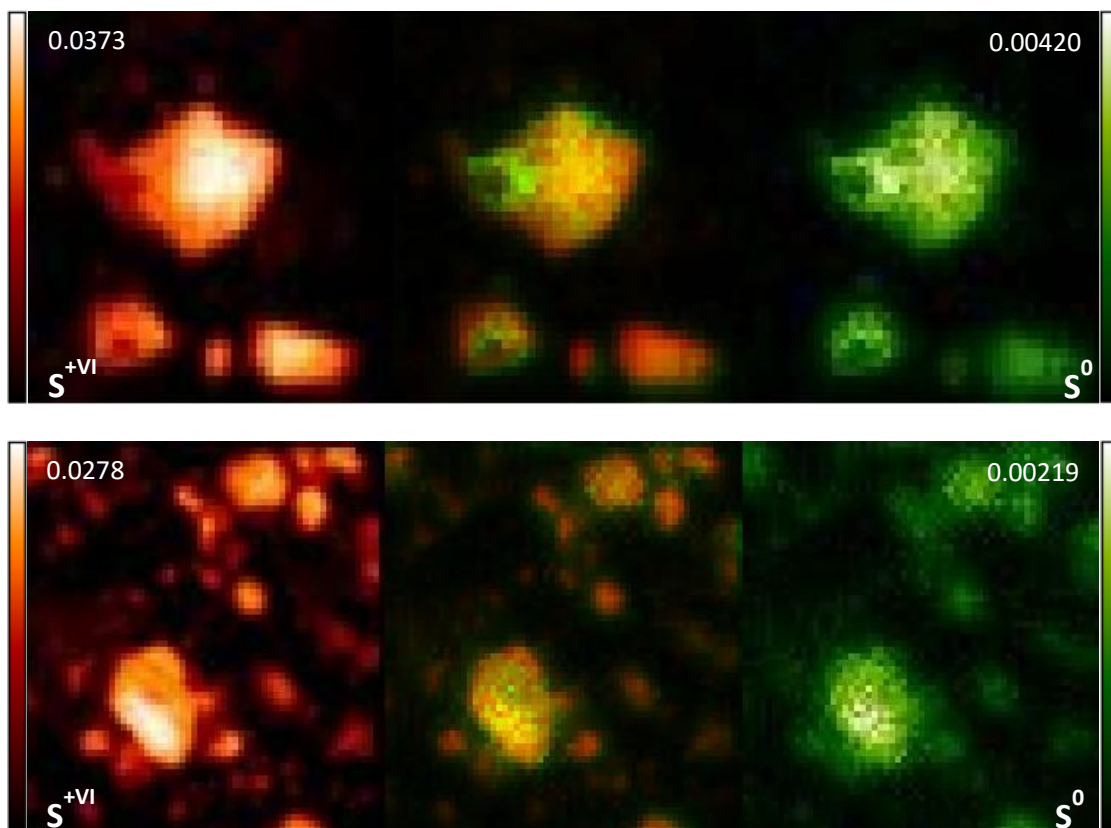


Figure 3.4 X-ray fluorescence map of sulfur for two ambient particulate matter samples The sulfur elemental density maps are scaled from black, lowest intensity, to white for the highest intensity. The maximum intensity value for the elemental map is shown in the upper corner, with corresponding scale bars on the side of the elemental density maps. For both samples, S^{+VI} (red) is concentrated in the center of the particle, where the particle mass is highest. S^0 (green) has a more varied spatial distribution, but is generally concentrated in one specific area. An overlay of the S^0 and S^{+VI} elemental density is shown in the center.

Table 3.2 Composition of Sulfate from Bulk Ambient Aerosols and Emission Sources

Sampling Location	Ammonium Sulfate		Cu(II) Sulfate		Gypsum		Iron(III) Sulfate		Potassium Sulfate		R factor
	%	±	%	±	%	±	%	±	%	±	
Yorkville	61.3	8.5	-	-	-	-	38.7	8.5	-	-	0.096963
Fort Yargo	83.9	7.4	-	-	-	-	16.1	7.4	-	-	0.0767302
Fire Station 8	86.5	6.5	13.5	16.3	-	-	-	-	-	-	0.0692747
Jefferson St	50.5	7.5	-	-	-	-	49.5	10.4	-	-	0.06186
South Dekalb 8/11	62.9	6.7	-	-	-	-	28.8	6.3	8.3	12.7	0.0169871
South Dekalb 2/13	42.3	13.9	-	-	-	-	57.7	13.9	-	-	0.0792618
South Dekalb 8/09	-	-	-	-	42.5	14.5	57.5	14.5	-	-	0.2040939
Biomass Burning	-	-	-	-	-	-	-	-	100.0	0.0	0.3686555
CFA	-	-	-	-	100.0	0.0	-	-	-	-	0.1054832
Diesel	70.2	11.0	-	-	-	-	29.8	12.4	-	-	0.034851

Table 3.3 Composition of Sulfate in Individual Particles

Sample ID	Ammonium Sulfate		Cu(II) Sulfate		Gypsum		Iron(III) Sulfate		Potassium Sulfate		Jarosite		R factor
	%	±	%	±	%	±	%	±	%	±	%	±	
FS8 8.11.11 P1	52.7	6.5	47.3	5.0	-	-	-	-	-	-	-	-	0.07684
FS8 8.11.11 P2	100.0	0.0	-	-	-	-	0.0	13.8	-	-	-	-	0.84504
FS8 8.11.11 P3	14.1	11.6	56.6	16.9	29.3	8.3	-	-	-	-	-	-	0.1339
FS8 8.11.11 P4	57.6	11.9	-	-	28.5	14.5	-	-	-	-	13.9	23.0	0.12948
FY 6.10.11 P1	59.1	10.0	-	-	32.2	7.6	-	-	8.6	5.0	-	-	0.035425
FY 6.10.11 P2	37.3	6.4	62.7	4.7	-	-	-	-	-	-	-	-	0.081002
FY 6.10.11 P3	-	-	100.0	0.0	-	-	-	-	-	-	-	-	0.11171
FY 6.10.11 P4	67.6	5.9	-	-	-	-	-	-	32.4	5.9	-	-	0.10811
FY 9.17.08 P1	29.5	16.6	70.5	3.6	-	-	-	-	-	-	-	-	0.53495
FY 9.17.08 P2	70.0	3.4	-	-	-	-	-	-	30.0	6.8	-	-	0.038327
FY 9.17.08 P3	65.5	7.9	-	-	-	-	-	-	34.5	5.1	-	-	0.080905
FY 9.17.08 P4	65.3	5.6	-	-	-	-	-	-	34.7	9.3	-	-	0.0143
FY 9.17.08 P5	80.1	8.9	-	-	-	-	-	-	19.9	31.0	-	-	0.17596
SD 8.24.11 P1	-	-	64.2	3.1	-	-	35.8	17.3	-	-	-	-	0.42401
SD 8.24.11 P2	100.0	0.0	-	-	-	-	-	-	-	-	-	-	0.49603
SD 8.24.11 P3	-	-	-	-	-	-	100.0	16.0	-	-	-	-	0.09181
SD 8.24.11 P4	100.0	19.4	-	-	-	-	-	-	-	-	-	-	0.67987

CHAPTER 4

IRON OXIDATION STATE AND COMPOSITION OF SAHARAN AEROSOLS: EVIDENCE OF MODIFICATION DURING ATMOSPHERIC TRANSPORT

4.1 Abstract

Aerosol iron was examined in Saharan dust plumes using a combination of iron near-edge X-ray absorption spectroscopy and wet chemical techniques. Aerosol samples were collected at three sites located in the Mediterranean and Atlantic to characterize iron at different stages of atmospheric transport. Iron(III) oxides were a component of aerosols at all sampling sites and dominated the aerosol iron in Mediterranean samples. In Atlantic samples, iron(II & III) sulfate, iron(III) phosphate, and iron(II) silicates were also contributors to aerosol composition. With increased atmospheric transport time, iron(II) sulfates are found to become more abundant, aerosol iron oxidation state became more reduced, and aerosol acidity increased. Acidic reactions and photo-reduction likely influence the form of iron minerals and oxidation state in Saharan dust aerosols and contribute to increases in aerosol iron solubility.

Longo, A.F., Feng, Y., Lai, B., Landing, W., Nenes, A., Mihalopoulos, N. Violaki, K., Ingall, E.D. (2016) Iron oxidation state and composition of Saharan aerosols: Evidence of modifications during atmospheric transport. *In Review at Environmental Science & Technology*

4.2 Introduction

Iron is a key micronutrient that is vital for all organisms and controls primary productivity in approximately 30% of the world's oceans (Moore et al., 2013). As a result, the relationship between iron and marine microorganisms has been extensively studied, most notably through iron fertilization experiments that examine sequestration of carbon dioxide (Buesseler et al., 2004; K. H. Coale et al., 2004; de Jong et al., 2012; Martin, 1990). These studies show that the addition of iron to high nutrient low chlorophyll (HNLC) waters often increases primary productivity creating large algae blooms (Boyd et al., 2000; Buesseler et al., 2004; K. H. Coale et al., 2004; K.H. Coale et al., 1996; de Jong et al., 2012). These studies also point to a need to better understand and quantify the inputs of iron to HNLC regions. As an important iron source to marine ecosystems, it is critical to understand the factors controlling the solubility and associated bioavailability of iron in atmospheric aerosols (Jickells et al., 2005; Mahowald et al., 2005).

The Sahara Desert contains the largest and most active sources of dust globally (Engelstaedter, Tegen, & Washington, 2006). Saharan dust is uplifted and entrained as aerosol where it can be transported vast distances from the source in the Saharan Air Layer. Traces of Saharan dust can be found from Greece to the Americas, making it a key source of nutrients to the Mediterranean Sea, much of the North Atlantic Ocean, and even as far as the Gulf of Mexico (Ganor & Mamane, 1982; Lenes, Prospero, Landing, Virmani, & Walsh, 2012). As a result, this influential dust source has been extensively studied as a nutrient reservoir (Baker et al., 2007; Herut, Collier, & Krom, 2002; Herut et al., 2005). Although the factors that control the solubility of iron in mineral dust remain

unclear, many hypotheses have been proposed. Compositional and oxidation state variations as well as particle aging processes, including photo-reduction (Cornell & Schindler, 1987; Wiederhold et al., 2006; Zhuang, Yi, Duce, & Brown, 1992b), organic ligand association (Wiederhold et al., 2006; N. Xu & Gao, 2008), and proton reactions (Buck, Landing, Resing, & Lebon, 2006; Buck, Landing, Resing, & Measures, 2010; Journet, Desboeufs, Caquineau, & Colin, 2008; Meskhidze, Chameides, & Nenes, 2005; Meskhidze, Chameides, Nenes, & Chen, 2003; Wiederhold et al., 2006), have all been proposed as controls of aerosol iron dissolution, but little direct evidence for these has been collected for Saharan dust.

In laboratory studies, proton reactions have been shown to enhance solubility of recalcitrant mineral phases (Journet et al., 2008; Nenes et al., 2011; Wiederhold et al., 2006) as well as precipitate iron-rich reactive nanoparticles (Shi et al., 2009; Shi, Krom, Bonneville, & Benning, 2015); however, evidence of acidic reactions is only circumstantial for environmental samples (Nenes et al., 2011; Oakes, Ingall, et al., 2012; Sullivan et al., 2007). During atmospheric proton reactions, acidic species may overcome the carbonate buffer capacity of an aerosol particle, allowing the pH to reach values of 1 to 2 in aqueous solutions surrounding aerosol particles (Ito & Feng, 2010). Under these acidic conditions, iron is more soluble (Oakes, Ingall, et al., 2012). Models have estimated photo-chemical and organic ligand-promoted dissolution to increase solubility of iron by an order of magnitude and are predicted to increase global aerosol iron inputs by as much as 75% (Johnson & Meskhidze, 2013). Because of the uncertainty surrounding particle aging processes, proton reactions are the most common reaction type included in atmospheric models. This variability in modeled global soluble iron flux

impedes understanding of aerosol iron in marine ecosystems and interactions between the atmosphere and ocean biogeochemical cycles (Blain, Bonnet, & Guieu, 2008).

Observational studies of aerosol composition and aging processes often employ bulk measurements of iron composition and oxidation state (Cornell & Schindler, 1987; Cornell & Schwertmann, 1996; Wiederhold et al., 2006; N. Xu & Gao, 2008). Composition of aerosol iron has often been confined to oxidation state (Fittschen et al., 2008; Majestic, Schauer, & Shafer, 2007) or sequential extraction procedures, which categorize iron as water-exchangeable, easily reducible, or oxidizable. (Dabek-Zlotorzynska, Kelly, Chen, & Chakrabarti, 2003). Spectroscopic techniques allow for more detailed aerosol iron characterization, such as identification of specific compound or mineral classes (Hoffmann et al., 1996; R. C. Moffet et al., 2012; Oakes, Weber, et al., 2012; Weber et al., 2000). Here, bulk chemical characterizations are combined with synchrotron-based elemental mapping and spectroscopy to analyze Saharan dust aerosols. The results of these experiments are then combined with a thermodynamic analysis of the major soluble ions present in the sample for the determination of its acidity.

4.3 Methods

4.3.1 Sample Collection

Three sampling sites were used to capture Saharan dust at different stages of transport. The Mediterranean samples, closest to the Saharan dust source, were collected at the Finokalia Research Station (35.32 N, 25.67 E), a site isolated from both local and regional influences on the island of Crete, Greece, located 70 km from the nearest major city (Markaki et al., 2003). Samples of particulate matter with an aerodynamic diameter <

10 μm , PM₁₀, were collected on Teflon filters using a virtual impactor with an operational flow rate of 16.7 L min⁻¹. Seven samples were collected at the Finokalia site over a one to three day period from 2009-2011 during which North African air masses dominated.

Twenty-four hour particle collections were completed as part of the 2011 GEOTRACES Atlantic transect (Shelley, Morton, & Landing, 2015). Because the GEOTRACES samples were collected over a short period of time and relatively near the source, they likely provide the purest sampling of Saharan air masses. The GEOTRACES samples are collected from three sites; however, the sampling locations are very close together, and the dust was from a single dust event, sampled over three days. Therefore, the GEOTRACES sample sites are referred to collectively. The three samples were collected at the following locations: Sample 7899, 22.37°N 35.62°W; Sample 7946, 20.88°N 32.62°W; Sample 8004, 19.43°N, 29.38°W. Total aerosol was collected using Whatman-41 filters and a Tisch 5170-VBL high volume sampler operated on average with a face velocity of ~100 cm/sec. (Shelley et al., 2015) The aerosol sampler was sector and wind speed controlled to avoid contamination from ship's exhaust. The aerosol sampler was wind speed (> 0.5 m/s) and sector-controlled (+/- 60 deg from bow) to avoid contamination from ship's exhaust.

Weekly samples were collected at the Bermuda Institute of Ocean Sciences (32.24°N, 64.87°W), which represent the longest transport of Saharan dust in our collection. Sampling was conducted from June 2011 to June 2012. These samples were collected using a Tisch 5170-VBL high-volume Total Suspended Particle (TSP) aerosol sampler using Whatman-41 filters and with a face velocity of ~100 cm/sec. Of the fifty-two

samples that before were collected, eight samples were largely influenced by Saharan dust events. All aerosol samples were stored in the dark at -20°C until analysis.

Samples of Saharan soil were collected from Morocco, Libya, and Senegal in 2009 and 2010 to serve as potential source material for the Saharan dust plumes that were sampled in the Atlantic Ocean and Mediterranean Sea. Sampling locations are provided in Table 4.1 (4.6 Supporting Material). Samples were ground with an agate mortar and pestle to facilitate analyses.

4.3.2 HYSPLIT

Hybrid Single Particle Lagrangian Integrated Trajectory Model (HYSPLIT) (Draxier & Hess, 1998; Izquierdo et al., 2012) back trajectories were completed for each sample using the GDAS half-degree meteorological archive in order to confirm the geographic origin of the air masses sampled. For the Bermuda Institute of Ocean Sciences (BIOS) and GEOTRACES samples, HYSPLIT back trajectories were calculated at 0 m, 500 m and 1000 m above ground level to confirm the North African provenance. At the Finokalia Research Station, HYSPLIT back trajectories were calculated at 1000 m and 3000 m above ground level for five days (approximately atmospheric life time of dust aerosols) preceding sample collection. HYSPLIT back trajectories computed at 1000 m show the origin of air masses within the boundary layer; this height is chosen, rather than the more conventional heights of 0 m or 500 m to avoid orographic influences at this site. HYSPLIT back trajectories were computed at 3000 m to identify dust events. At Finokalia Research Station, dust is either homogeneously distributed from 0 to about 3000 m, during spring and autumn dust events, or is found in a layer between 2500 –

4000 m during summer and autumn dust events (Kalivitis et al., 2007). While the HYSPLIT back trajectories do not guarantee that pure end members were sampled, they help to demonstrate that most air masses contained North African origins during the sampling time periods. Additionally, all samples had the distinctive reddish color of samples derived from Saharan regions.

The HYSPLIT back trajectories were also used to estimate the residence time of dust aerosols in the atmosphere from generation in the Sahara Desert to collection. For this calculation, a five day HYSPLIT back trajectory was completed in ensemble mode at 3000 m. Since each sample was a multiday collection, HYSPLIT back trajectories were completed for each day during the collection period. The mean distance travelled was then determined for each sample and taken as the average distance travelled in five days by the air mass. The average distance travelled in five days was used to estimate a velocity for each sample (average distance travelled in five days divided by five days time). Finally, the distance travelled from source to collection was estimated. The source region in the Sahara Desert was taken as a single location (30°N, 8.5°E). The distances travelled were estimated as follows: Finokalia Research Station, 1763 km; GEOTRACES, 2098 km; and Bermuda Institute of Ocean Science, 6897 km. Using these distances and the estimated velocities, an approximation of travel time was generated for each sample. These approximate travel times are reasonable for Saharan dust events which have been known to travel for as many as 30 days before deposition (Mahowald et al., 2014).

4.3.3 Total and soluble iron

Water soluble iron, hereafter referred to as soluble iron, was determined for all samples using the ferrozine technique (Stookey, 1970). Handling of the filters was conducted under a HEPA-filter laminar flow hood. A quarter filter was extracted into 10 mL of deionized water ($>18\text{ M}\Omega$) in a trace metal grade centrifuge tube by 30 min of ultrasonication. The extraction was followed by the removal of insoluble particles from the extract by a $0.2\ \mu\text{m}$ pore size syringe filter. Any dissolved Fe(III) in the sample was reduced to Fe(II) through the addition of $40\ \mu\text{M}$ solution of hydroxylamine hydrochloride added in a 1:100 ratio reagent to filter extracts. Samples were allowed to react with the hydroxylamine hydrochloride overnight. A $5\ \text{mM}$ ferrozine solution which forms a colored complex with dissolved Fe(II) was then added in a 1:100 ratio reagent to filter extracts. After a ten minute reaction, samples were spectrophotometrically measured at $562\ \text{nm}$ (Oakes, Ingall, et al., 2012). Total iron was measured for GEOTRACES and Bermuda Institute of Ocean Science samples using protocols described in Morton et al. (2013) (Kadko, Landing, & Shelley, 2015; Morton et al., 2013; Shelley et al., 2015). For BIOS and GEOTRACES samples, total iron was also measured via elemental densities collected from X-ray fluorescence maps to ensure total iron could be reliably determined through synchrotron-based techniques (Oakes, Weber, et al., 2012), and for Finokalia Research Station samples, total iron was only determined using elemental densities collected from X-ray fluorescence maps.

4.3.4 Soluble ions

Ion chromatography was used to measure major soluble ions for each aerosol sample (Bardouki et al., 2003). Briefly, approximately 1/8th of each filter was extracted into 10 mL of nanopure water using an ultrasonic bath for 45 min. The filter extracts were then syringe filtered (PALL IC Acrodisc (PES), 0.45 μm , 13 mm) to remove any insoluble species. The acquired filtered solutions were analyzed for anions (Cl^- , Br^- , NO_3^- , SO_4^{2-} , HPO_4^{2-} , $\text{C}_2\text{O}_4^{2-}$) and cations (NH_4^+ , K^+ , Na^+ , Mg^{2+} , Ca^{2+}). Anions were determined using a Dionex-500 ion chromatograph equipped with an Ion Pac AS4A-SC column and an AG4A-SC precolumn, with an ASRS-300 suppressor. Anion separation was conducted with isocratic elution of NaHCO_3 (3.4 mM)/ Na_2CO_3 (3.6 mM) as an eluent and a flow of 1.5 mL min^{-1} . For cations, an Ion Pac CS12A column and a CG12A guard column were used, with a CSRS-300 suppressor, under isocratic elution of 20 mM MSA (methanesulfonic acid) at a flow rate of 1.0 mL min^{-1} . The detection limit of the analysis was 20, 12, 40, 12 and 40 ppb for NH_4^+ , K^+ , Na^+ , Mg^{2+} , and Ca^{2+} , respectively, while the corresponding detection limit for all anions (Cl^- , Br^- , NO_3^- , SO_4^{2-} , HPO_4^{2-} , and $\text{C}_2\text{O}_4^{2-}$) was 20 ppb.

4.3.5 pH modelling

ISORROPIA was used to estimate the aerosol acidity of each aerosol sample (Fountoukis & Nenes, 2007; Nenes, Pandis, & Pilinis, 1998). This thermodynamic model will output the concentration of species in the gas and aerosol (solid/liquid) phases, pH, and aerosol water. The pH determined via ISORROPIA is only an estimate because of size of the particles in these samples will not allow for equilibrium conditions, an

assumption of this thermodynamic model. Therefore, this approach to aerosol pH modelling will only determine whether the samples are acidic or circa neutral. To compute the pH, knowledge of the relative humidity and temperature is needed; therefore, values characteristic of a humid marine boundary layer were assumed (80-90% Relative humidity; 293K). Input values for major aerosol species can be found in Table 4.3 (4.6 Supporting Material).

4.3.6 Synchrotron analysis

Saharan soil and aerosol composition was determined using the micro X-ray fluorescence capabilities at Argonne National Laboratory, Advanced Photon Source, Station 2-ID-D. In this study X-ray fluorescence microscopy and X-ray Absorption Near Edge Structure (XANES) spectroscopy were used to examine the iron in aerosol. In this study, these techniques work by providing incident X-rays of sufficient energy to bombard atoms, ejecting the electrons from the innermost shell electron shell. Subsequently, an outer shell electron may relax into the vacated position, emitting a characteristic fluorescence signal. The type, oxidation state, and structural arrangement of atoms in a particle are revealed as the ejected electron interacts with neighboring atoms and are reflected in XANES spectra (ED Ingall et al., 2011). Therefore, Fe-XANES spectra provide information on both oxidation state and the composition associated with the element of interest.

An energy dispersive Si-drift detector (Vortex EM, with a 50 mm² sensitive area, and a 12.5 μm Be window; SII NanoTechnology, Northridge, CA) was used to measure X-ray fluorescence of the samples. All measurements were conducted under a helium

atmosphere in order to minimize absorption and fluorescence caused by beam interactions with air. A randomly selected area of each filter sample (0.5 cm^2) was placed over a slot of an aluminum sample mount for analysis. The sample was initially analyzed in microscopic X-ray fluorescence mode to identify iron-containing particles on the filter. In this mode, the X-ray beam with a diameter of ca. 200 nm was scanned over a randomly selected filter area (typically 40 to $50 \text{ }\mu\text{m}^2$) at a step size of $0.4 \text{ }\mu\text{m}$ and 0.5 s dwell time to produce an elemental distribution map of the filter. The resulting elemental data were compiled to identify iron-containing particles ($>1 \text{ }\mu\text{m}$ diameter) for Fe-XANES spectroscopy.

Fe-XANES spectroscopy was conducted in bulk and individual particle modes. The composition of Saharan soil was only characterized in bulk mode. In bulk Fe-XANES mode, X-ray focusing optics (zone plate and order sorting aperture) were removed allowing characterization of iron present in ca. 0.4 mm^2 filter areas. In individual particle mode, iron-containing particles identified in elemental distribution maps were characterized with a focused beam with a $0.4 \text{ }\mu\text{m}$ spot size. Of course, every particle could not be examined because of time constraints. Based on elemental maps, particles were selected to attempt to characterize as many different elemental iron associations as possible. Individual particle XANES spectroscopy represent the composition of the entire particle. In both bulk and individual particle modes, XANES scans were collected from 7100 to 7180 eV in 0.5 eV steps with 0.5 – 3 s dwell time per step.

4.3.7 Data reduction

Oxidation state was determined for each sample by determining the pre-edge centroid of each Fe-XANES spectra. The pre-edge feature has been shown to be the most reliable indication of oxidation state, and by interpolating between pre-edge centroid position % Fe(II) of standards, the relative abundance of Fe(II) can be determined for environmental samples (Bajt, Sutton, & Delaney, 1994; Oakes, Weber, et al., 2012; Wilke, Farges, Petit, Brown, & Martin, 2001).

Spectral data was normalized to account for variations in incoming X-ray flux and processed using the Athena software package (Ravel & Newville, 2005). In total, 105 spectra were collected. In order to extract the most useful information from this number of spectra, data reduction techniques were employed. A combination of principle component analysis, PCA, and k-means clustering were used to group like spectra (Marcus & Lam, 2014). The PCA algorithm used, built into Athena (Ravel & Newville, 2005), generates a scree plot where the number of principle components can be determined. Like spectra were merged (Ravel & Newville, 2005) to create an average spectra representing a cluster, and linear combination fitting was then completed for each cluster's Fe-XANES spectra using Athena (Ravel & Newville, 2005). These data reduction techniques were used on each sampling site, with the spectra being divided into bulk and individual particle Fe-XANES.

The linear combination fitting algorithm in Athena uses a database of known iron mineral standards (e.g., iron oxides, organics, silicates, sulfides, and sulfates) (E

Ingall et al., 2013) run on the same synchrotron beamline, in this case, to determine the phases contributing to an unknown aerosol Fe-XANES spectra. An iterative process was used to refine the standard database used to model the sample spectra. First, exotic iron minerals unlikely to be major components of aerosol iron were excluded from the database (Oakes, Weber, et al., 2012). Second, the database was narrowed through elimination of standards with low contribution (i.e. less than 10%) or poor fit (i.e. high R-factor) during initial linear combination fitting. Also, insufficient quantities of a specific mineral or compound in a sample can also lead to underestimation of the specific compound during linear combination fitting (Dean Hesterberg, 2010); thus, iron composition was generalized to express broad chemical classes: iron(III) oxides, iron(III) sulfates, iron(III) phosphates, iron(II) sulfates, and iron(II) silicates. Athena uses a non-linear, least-squares minimization approach to fit spectra of unknown samples with standard material spectra, computing an error term, the R-factor, to quantify the goodness of a given linear combination fit. The linear combination of standards that yielded the lowest R-factor reflected the best fit (Ravel & Newville, 2005).

4.4 Results

To put the results in context, it is important to visualize the typical transport paths of air masses originating in the Sahara. Air masses carrying Saharan dust to Finokalia Research Station travel a relatively short distance across the Mediterranean (~1800 km); it is important to note that it is rare for these air masses to subsequently travel across the Atlantic. GEOTRACES samples collected off the west coast of Africa, near the Cape Verde Islands, also represent a relatively short travel distance (~2100 km). The air

masses that deliver Saharan dust to the Cape Verde islands and surrounding waters may continue their westward journey across the Atlantic Ocean, reaching Bermuda after atmospheric transport of approximately 6900 km from source.

4.4.1 Iron Solubility

Saharan dust solubility varies at the three different sampling sites, with the highest solubility at the Bermuda Institute of Ocean Sciences (BIOS) site and the lowest at the GEOTRACES collection site (Figure 4.1). While BIOS exhibited the highest solubility, it has the least amount of total iron, averaging 196 ng/m³ (Table 4.2). Both the Finokalia Research Station and GEOTRACES collection sites have significantly more total iron

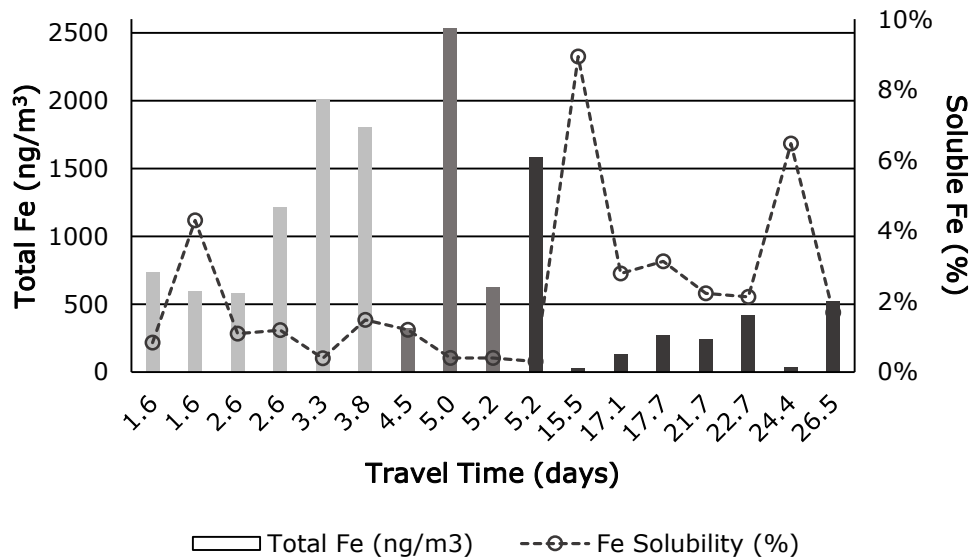


Figure 4.1 Total and Soluble Iron of Saharan Dust Finokalia Research Station (■) has the shortest travel times, followed by the GEOTRACES collection (■), then finally BIOS (■). While BIOS consistently has the highest solubility, there is no correlation between the approximate travel time and either total iron ($R^2 = 0.35$) or fractional iron solubility ($R^2 = 0.18$).

with average concentrations of 735 ng/m³ and 1580 ng/m³, respectively. At each collection site, the soluble iron was on the same order of magnitude with mean values ranging from averaging 5.0-8.75 ng/m³. This cannot be solely due to the preferential removal of insoluble iron particles, as there were large variations in Fe speciation between the different sites (Figure 4.2). Moreover, when the soluble iron is normalized to the total iron, the differences between each collection location become apparent. The BIOS contained on average 2.55% soluble iron, with values ranging from 1.7 – 8.9% (Figure 1). In contrast, the GEOTRACES collections had consistently low solubility, averaging 0.41%. Finokalia Research Station fell between these two locations containing on average 1.2% soluble iron; this station also contained a wide range of iron solubilities from 0.4 – 1.5% (Figure 4.1). Solubility generally increases with travel time, with BIOS samples, which exhibit the longest travel time, being more soluble than GEOTRACES and Finokalia Research Station stations, which both receive air masses after a short transport period; however, there is not a clear statistical relationship between travel time and iron solubility or total iron concentrations (Figure 4.1). This increased solubility could be attributed to the decreases seen in pH as the travel time increases (Table 4.2; 4.6 Supporting Material). The pH drops from circa neutral to less than four pH units after approximately 15 days in the atmosphere, which corresponds to a marked increase in solubility.

4.4.2 Iron Composition

Bulk Fe-XANES revealed two compositions for iron in Saharan soil (Table 4.4; 4.6 Supporting Material). The majority of Moroccan samples, including samples M1, M6, M11, and M13, were composed of about 84% iron(III) oxides and 16% iron(II) sulfates.

The remaining Moroccan samples, as well as those from Libya and Senegal, were composed of only iron(III) oxides.

The results of the k-means cluster analysis and linear combination fitting reveal the iron composition at the Finokalia Research Station to be uniform at the bulk level (Table 4.4; 4.6 Supporting Material). At the GEOTRACES collection sites, each bulk sample was determined to be compositionally distinct despite the fact that the collections sampled three sequential days. At the bulk level, iron from the BIOS collection site was represented by two compositions. Individual particles sampled from Finokalia Research Station all have the same composition; similarly, individual particles sampled from the BIOS collection also exhibited a uniform composition. At the GEOTRACES sample site, the composition of the individual particles sampled was much more varied having one of three different iron compositions (Table 4.4; 4.6 Supporting Material).

In contrast to the GEOTRACES and BIOS collection sites, the Finokalia aerosol samples are on average dominated by iron(III) oxides (>90%) similar to the Sahara soil samples, except the Moroccan samples M1, M6, M11, M13. The GEOTRACES and BIOS samples contain significantly less iron(III) oxides (57% and 41%, respectively) on average. In the GEOTRACES and BIOS aerosol samples, iron(III) oxides are found along with lesser portions (<30%) of iron(II) sulfates, iron(III) sulfates, iron(III) phosphates, and iron(II) silicates. Individual particles from Finokalia Research Station samples followed similar average trends in composition as their bulk counterparts. In contrast, individual particles in both the GEOTRACES and BIOS samples showed notable variation from the bulk composition at these sampling locations. BIOS individual particles were comprised of primarily iron(III) oxides (>70%) with the remaining fraction

being iron(II) silicates, and GEOTRACES individual particles contained iron(III) phosphates and iron(II & III) sulfates. (Figure 4.2)

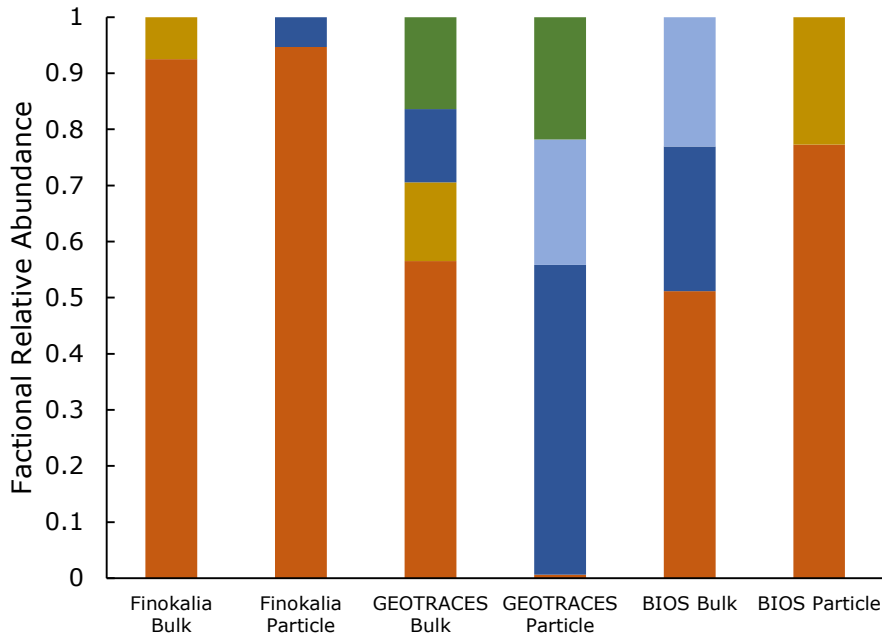


Figure 4.2 Mean Bulk and Individual Particle Iron Composition of Saharan Dust Iron(III) oxides (■) dominate in Finokalia Research Station, with traces of iron(II) silicates (■) and iron (II) sulfates (■) in the bulk and individual particles, respectively (7 bulk sample spectra; 11 individual particle spectra). At GEOTRACES, iron(III) sulfates (■) and iron(III) phosphates (■) appear (3 bulk sample spectra; 17 individual particle sample spectra). Bulk samples from BIOS contain significant contributions from iron sulfates; while individual particles are a mix of iron(II) silicates and iron(III) oxides (8 bulk sample spectra; 18 individual particle spectra).

4.4.3 Oxidation State

In addition to the bulk compositional shifts, Saharan dust experiences a shift in oxidation state between the different sampling sites. The Finokalia Research Station

contains the most oxidized iron with more than 85% of the iron as iron(III), while the BIOS and GEOTRACES aerosol samples contain approximately 60% iron(III). The iron oxidation state, shown using the pre-edge centroid position, is negatively correlated ($R^2=0.54$) with approximated travel time, suggesting that the longer an air masses travels in the atmosphere, the more reduced the iron becomes (Figure 4.3). Although iron(II) is generally considered more soluble than iron(III), the fractional solubility of iron did not correlate ($R^2 = 0.14$) with oxidation state (Table 4.2).

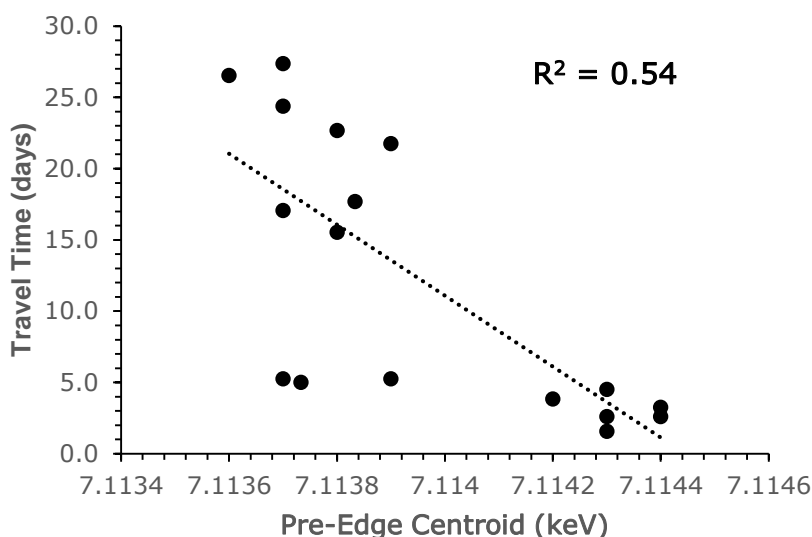


Figure 4.3 Travel Time as a Function of Iron Oxidation State Distance travelled, determined via HYSPLIT back trajectory, is negatively correlated with the increasing oxidation of iron in bulk aerosol samples. The pre-edge centroid, a reliable indicator of oxidation state, increases as iron transitions from iron(II) to iron(III).

4.5 Discussion

The transformation of Saharan dust during atmospheric transport can be seen most clearly in the oxidation state, with aerosol iron being more reduced than most of the Saharan soil investigated in this study and also becoming more reduced the longer it is transported in the atmosphere (Figure 4.4; 4.6 Supporting Material). Photo-reduction pathways for aerosol iron have been demonstrated for both ligand assisted and unassisted mechanisms in laboratory settings (Siefert, Pehkonen, Erel, & Hoffmann, 1994; Siefert, Webb, & Hoffmann, 1996). Once in aqueous form, the reducible fraction of iron(III) can be quickly converted to iron(II) by ligand assisted photo-reduction mechanisms, with this reducible fraction having important implications for bioavailability (Y. Chen & Siefert, 2003; Siefert et al., 1994). A correlation between the oxidation state and the travel time is evident, but not strong ($R^2=0.54$). This could be attributed to differences within the different mineral classes we have defined. Even within the class of iron(III) oxides, different minerals have variable susceptibilities to photochemical processing (Cornell & Schindler, 1987). Despite iron(II) being more soluble than iron(III), there was no correlation between the oxidation state of iron and the solubility, which is consistent with the findings of (X. R. Zhu, Prospero, & Millero, 1997). Consistent with (Majestic et al., 2007), reductive processes appear to occur over relatively short time frames in these Saharan samples, on the order of one to three days. If iron phases susceptible to photo-reduction are completely reduced in this short time frame, then other transformation mechanisms, such as proton-induced iron dissolution, may become increasingly important on longer time scales. Such a shift in mechanisms offers a possible

explanation for the lack of a clear correlation between solubility and oxidation state of aerosol iron in the long-range transport of dust aerosols.

The oxidation state shifts were accompanied by transformations in the composition of iron in Saharan air masses. Saharan soil is dominated by iron(III) oxides, with only minor quantities of iron(II) sulfates; whereas, bulk aerosol iron from the GEOTRACES and BIOS collection locations contain on average only ~50% iron(III) oxides. For aerosol samples, the individual particle composition was often different from the bulk composition seen at a sample site, suggesting that the composition in the large particles ($>1\mu\text{m}$) is different from the fine particles ($<1\mu\text{m}$). However, not every large particle on the filters could be examined; therefore, these differences between bulk and individual particle composition could perhaps stem from particle selection during analysis (see Methods). However, the differences between individual particle composition and bulk composition could provide evidence of particle aging mechanisms. For example, individual particles from the Atlantic, were dominated by iron sulfates, which could be products of acid processing in the atmosphere. Smaller particles, because of their high surface area, will be more susceptible to acidification than larger particles (Nenes et al., 2011). This preferential acidification of small particles could result in different mineral precipitates being favored for different particle sizes. At the GEOTRACES collection site, iron(III) phosphates, iron(II) sulfates, and iron(III) sulfates were found in larger particles ($>1\mu\text{m}$). X-ray fluorescence imaging shows that aerosol phosphorus is sometimes collocated with iron and almost always with calcium. This suggests the iron phosphates are likely formed as a result of the aggregation and subsequent acidification of calcium phosphate containing particles and iron containing particles. At the BIOS

collection site, the opposite is observed. The iron sulfates account for nearly 50% of total iron, but appear only in the bulk phases, suggesting that iron sulfates are likely to be found in small particles ($<1 \mu\text{m}$). This could reflect that there are several sources of sulfate, including seasalt, acidic species, and Saharan soil, thus, particles do not need to aggregate to form the iron sulfate compounds.

The pH of the aerosols became more acidic with increased transport time (>15 days), which corresponds to the aerosols with the more soluble iron. This suggests that proton reactions are solubilizing the iron during atmospheric transport. Our observations of iron phosphates provide further support that acidic reactions are occurring. These phases were not found in any Saharan soil, suggesting they formed in the atmosphere. Although iron sulfates were a minor component of a few Saharan soils, additional mechanisms are likely necessary to explain levels found in bulk BIOS and GEOTRACES samples. Sulfates have also been shown to preferentially accumulate on aluminosilicate-rich dust if the dust air mass contacts a sulfate-rich air mass during transport (Sullivan et al., 2007). Correlations between non-seasalt sulfate and soluble Fe suggest acid formation in aerosols as a means to solubilize iron in laboratory studies (Srinivas, Sarin, & Kumar, 2012), but these correlations were not found in Atlantic samples, likely because these are in fact not good proxies for aerosol acidity (Hennigan, Izumi, Sullivan, Weber, & Nenes, 2015a). Together these two findings support our observations of iron sulfates, which could precipitate out of solution as these acidic reactions occur. However, these reactions can be buffered by carbonate minerals found in Saharan dust (Ito & Feng, 2011; Meskhidze et al., 2003), so the carbonate buffer capacity of the particles must be overcome for these reactions to proceed. The buffering effect of carbonate present in

Saharan dust helps explain the finding of secondary phosphates from acidic reactions as well (Nenes et al., 2011) as the iron(III) oxides in particles where acids were not able to overcome the carbonate buffer.

As the largest source of dust to the Atlantic Ocean, it is important to consider the iron inputs from the Sahara Desert. Shift in oxidation state points to a reductive mechanism taking place during atmospheric transport while iron phosphate and sulfate phases offer possible support for proton reactions. However, these two together may not be sufficient to fully explain differences in aerosol iron solubility seen at the short and long range sampling locations. Ligand promoted iron dissolution is another potential factor influencing aerosol iron solubility (Wozniak et al., 2013). Overall, these findings suggest that a combination of factors are at work to affect the aerosol iron solubility in long-distance atmospheric transport. The observed variations in composition, oxidation state, pH, and solubility of aerosol iron shown here provide insights for process-scale understanding of chemical transformations during atmospheric transport. The observed iron solubility in Saharan dust ranges from 0.41% to 8.9% across the Atlantic Ocean, consistent with previous studies of Saharan dust aerosols in this region (0.05% to 7.9%) (Baker, Jickells, et al., 2006). Iron solubility is higher in aged dust aerosols with lower total iron loadings. Additionally, acidity increases in aged particles suggesting that proton reactions play a role in the transformation of aerosol iron. Iron is enriched in iron(II) or iron(III) sulfates and iron(III) phosphates as it travels to BIOS. Nearly half of the aerosol iron in the BIOS samples was present as iron(II) or iron(III) sulfates, and the formation of iron sulfate appear to significantly increase the iron solubility. Variations in iron(II) and iron(III) relative to aerosol aging and iron solubility highlights the importance of

modeling the reductive dissolution in addition to proton-induced reactions. This is important not only for understanding current ecosystem dynamics, but also on potentially longer time scales. On glacial-interglacial time scales, photo-reduction has been proposed to significantly increase the concentration of iron(II) in the fine dust (Spolaor, Vallelonga, Cozzi, Gabrieli, et al., 2013). In fact, during the Last Glacial Maximum, iron(II) concentrations have been estimated to be seven times higher in fine dust than in the interglacial period, whereas iron(III) concentrations only doubled (Spolaor, Vallelonga, Cozzi, Gabrieli, et al., 2013). This emphasizes the need to further examine these particle aging mechanisms, especially reductive mechanisms, *in situ* to gain a better understanding of the inputs of potentially bioavailable iron(II) to the marine environment.

4.6 Supporting Materials

Table 4.1 Collection Locations of Saharan Soil collected from Morocco, Libya, and Senegal

Country of Origin	Sample ID	Latitude	Longitude
Morocco	M1	31° 01'36"N	6° 35' 05"W
Morocco	M6	31° 26'36"N	5° 20' 38"W
Morocco	M8	30° 47'33"N	5° 31' 00"W
Morocco	M11	30° 25' 59"N	6° 55' 57"W
Morocco	M13	30° 10' 26"N	9° 15' 18"W
Morocco	M14	30° 25' 55"N	8° 53' 55"W
Libya	L1	26° 35'N	12° 46'E
Libya	L2	26° 15' 50"N	11° 09' 21"E
Libya	L3	32° 38' 21"N	14° 17' 26"E
Senegal	S1	15° 55' 15"N	16° 28' 18"W
Senegal	S2	16° 23' 57"N	16° 16' 15"W
Senegal	S3	16° 29' 48"N	14° 55' 45"W
Senegal	S4	15° 42' 22"N	16° 16' 19"W

Table 4.2 Iron Data Table for Saharan Air Masses

Sampling Location	Start Date	Fe Solubility (%)	Total Fe (ng/m ³)	% Fe(II) Bulk	Volume (m ³)	pH (RH=90%)	pH (RH=80%)	Travel Time (days)
BIOS	20/Jul/2011 13:30	2.23%	238.61	30.1	774.29	3.21	3.77	21.75
BIOS	1/Aug/2011 9:21	2.13%	414.23	37.1	714.56	2.68	3.32	22.67
BIOS	13/Aug/2011 10:21	3.14%	265.87	34.7	808.20	3.00	3.67	17.68
BIOS	19/Aug/2011 13:25	1.69%	521.94	51.0	768.70	3.28	3.96	26.53
BIOS	6/Sep/2011 9:05	2.79%	128.19	44.1	802.46	2.51	3.19	17.06
BIOS	26/Sep/2011 8:30	2.31%	153.46	44.1	542.86	3.87	4.49	27.37
BIOS	18/Oct/2011 10:12	8.94%	23.66	37.1	795.22	2.92	3.56	15.52
BIOS	15/May/2012 10:48	6.48%	37.29	44.1	795.67	2.60	3.25	24.38
FRS	18/12/09 0:01	1.09%	578.3	2.1	45.59	7.11	7.13	2.59
FRS	10/2/10 12:01	4.30%	596.4	-	38.37	7.11	7.13	1.60
FRS	10/3/10 0:01	0.83%	734.6	2.1	48.68	7.11	7.13	1.57
FRS	31/3/10 0:01	1.19%	1213.7	0	51.38	7.11	7.13	2.59
FRS	16/4/10 0:01	0.39%	2009.0	0.0	56.10	7.11	7.13	3.26
FRS	10/11/10 0:01	1.20%	323.6	2.1	58.72	7.11	7.13	4.52
FRS	24/12/10 0:01	1.48%	1798.4	9	38.87	7.11	7.13	3.83
GEOTRACES	5/Dec/2011 16:41	0.4%	623	30.1	116.01	5.43	6.04	5.25
GEOTRACES	6/Dec/2011 14:20	0.3%	1580	44.1	137.92	7.11	7.13	5.25
GEOTRACES	7/Dec/2011 15:50	0.4%	2530	41.7	108.81	7.11	7.13	5.00

Table 4.3 Concentration of Soluble Ions used to Model pH with ISORROPIA

Sampling Location	Start Date	Na ⁺ ($\mu\text{g}/\text{m}^3$)	NH ₄ ⁺ ($\mu\text{g}/\text{m}^3$)	K ⁺ ($\mu\text{g}/\text{m}^3$)	Mg ²⁺ ($\mu\text{g}/\text{m}^3$)	Ca ²⁺ ($\mu\text{g}/\text{m}^3$)	Cl ⁻ ($\mu\text{g}/\text{m}^3$)	Br ⁻ ($\mu\text{g}/\text{m}^3$)	NO ₃ ⁻ ($\mu\text{g}/\text{m}^3$)	HPO ₄ ⁻ ($\mu\text{g}/\text{m}^3$)	SO ₄ ²⁻ ($\mu\text{g}/\text{m}^3$)
BIOS	20/Jul/2011 13:30	0.68	0.030	0.056	0.16	0.23	1.40	0.0038	0.45	0.0028	1.48
BIOS	1/Aug/2011 9:21	0.99	0.035	0.13	0.39	0.36	4.50	0.011	0.42	0.0047	1.82
BIOS	13/Aug/2011 10:21	0.78	0.027	0.076	0.20	0.33	2.36	0.006	0.42	0.0078	1.11
BIOS	19/Aug/2011 13:25	0.74	0.026	0.065	0.17	0.32	1.67	0.0045	0.37	0.0063	1.01
BIOS	6/Sep/2011 9:05	1.30	0.051	0.21	0.75	0.42	8.25	0.017	0.38	0.0011	2.13
BIOS	26/Sep/2011 8:30	0.86	0.058	0.087	0.18	0.30	1.27	0.0017	0.45	0.015	1.61
BIOS	18/Oct/2011 10:12	0.55	0.021	0.063	0.20	0.11	2.63	0.0040	0.20	0.0019	0.79
BIOS	15/May/2012 10:48	1.17	0.036	0.13	0.43	0.24	5.80	0.0059	0.34	0.0022	1.49
FRS	18/Dec/09 0:01	2.58	0.021	0.14	0.44	1.62	4.34	0.0071	1.30	0.014	1.84
FRS	10/Feb/10 12:01	1.80	0.044	0.18	0.46	4.74	2.71	0.0099	1.13	0.031	2.08
FRS	10/Mar/10 0:01	2.55	0.050	0.11	0.42	2.21	3.26	0.0069	1.68	0.006	2.09
FRS	31/Mar/10 0:01	1.51	0.031	0.10	0.24	2.99	1.82	2.8E-04	1.75	0.018	1.47
FRS	16/Apr/10 0:01	0.69	0.009	0.10	0.17	3.43	0.65	0.0023	1.58	0.028	2.17
FRS	10/Nov/10 0:01	1.07	0.034	0.20	0.22	2.24	1.18	0.0039	1.46	0.083	2.44
FRS	24/Dec/10 0:01	0.92	0.033	0.088	0.20	3.78	1.18	0.0036	0.86	0.019	1.41
GEOTRACES	5/Dec/2011 16:41	2.71	0.10	0.19	0.34	0.44	3.87	0.0032	0.69	0.007	1.07
GEOTRACES	6/Dec/2011 14:20	2.49	0.040	0.15	0.33	1.89	4.44	0.0040	0.78	0.014	2.16
GEOTRACES	7/Dec/2011 15:50	3.14	0.067	0.23	0.44	2.41	5.70	0.0067	1.05	0.010	2.65

Table 4.4 Compositional Cluster of Bulk Samples and Individual Particles for Saharan Soil and Each Aerosol Collection Location

Sample Site	Type	No. of Samples	Fe(III) Oxide	Fe(II) Sulfate	Fe(III) Sulfate	Fe(II) Silicate	Fe(III) Phosphorus
Saharan Soil	Bulk	4	0.839 ± 0.024	0.161 ± 0.017	-	-	-
Saharan Soil	Bulk	9	1.0 ± 0	-	-	-	-
Finokalia Research Station	Bulk	7	0.925 ± 0.01	-	-	0.075 ± 0.01	-
Finokalia Research Station	Individual Particles	11	0.947 ± 0.003	0.053 ± 0.003	-	-	-
GEO TRACES	Bulk	1	0.472 ± 1.21	-	-	0.421 ± 0.11	0.107 ± 1.11
GEO TRACES	Bulk	1	0.895 ± 0.003	0.105 ± .04	-	-	-
GEO TRACES	Bulk	1	0.329 ± 1.03	0.287 ± 1.39	-	-	0.384 ± 0.9
GEO TRACES	Individual Particles	10	-	0.692 ± 0.04	-	-	0.308 ± 0.04
GEO TRACES	Individual Particles	6	-	0.366 ± 0.02	0.634 ± 0.59	-	-
GEO TRACES	Individual Particles	1	-	0.266 ± 0.02	-	-	0.626 ± 0.96
BIOS	Bulk	3	-	0.385 ± 0.04	0.615 ± 2.08	-	-
BIOS	Bulk	5	0.813 ± 0.02	0.187 ± 0.01	-	-	-
BIOS	Individual Particles	18	0.715 ± 0.014	-	-	0.285 ± 0.34	-

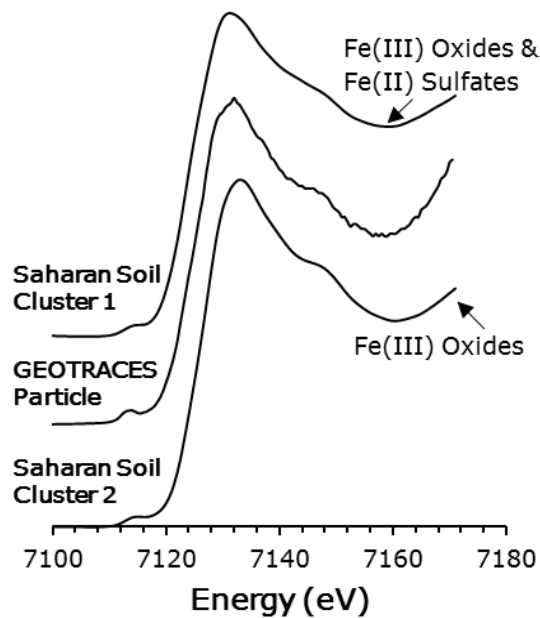


Figure 4.4 The Fe-XANES spectra of Saharan soil compared to the Fe-XANES spectrum from individual particle from the GEOTRACES collection station. Saharan soil is composed either entirely of iron(III) oxides (bottom) or a mix of iron(III) oxides and iron(II) sulfate (top). Saharan soil in cluster 1 is composed of 83.9% iron(III) oxides and 16.1% iron(II) sulfate, and Saharan soil in cluster 2 is composed entirely of iron(III) oxides. Individual particles, especially at the GEOTRACES collection site, often contain iron(II&III) sulfate and iron phosphate. Here, dashed lines denote key features on the individual particle spectra from the GEOTRACES collection that do not line up with either of the Saharan soils. Although subtle, these features are unique to specific iron compounds.

CHAPTER 5

THE ROLE OF IRON COMPOSITION AND OXIDATION STATE ON THE SOLUBILITY OF AEROSOL IRON

5.1 Abstract

The composition and oxidation state of aerosol iron were examined using synchrotron-based iron near-edge X-ray absorption spectroscopy. By combining synchrotron-based techniques with wet chemical extractions, the effect of oxidation state and composition on the solubility of aerosol iron is quantified for samples taken from five locations: India, the Southern Ocean, the Atlantic Ocean, Bermuda, and Crete. These locations capture aerosol from different source regions and with varying marine, mineral dust, and anthropogenic influences. Aerosol iron solubility is inversely related to total iron content. When all the sampling locations were taken together, there was no predominant factor, such composition, pH, oxidation state, or distance travelled, that could explain variations in aerosol iron solubility. The strongest factors influencing aerosol iron solubility for individual sampling locations are pH, oxidation state, and composition. The presence of secondary phases, such as iron phosphates and iron sulfates, in all samples combined with correlations between pH and iron solubility at specific sampling locations suggest that acidic reactions influence for aerosol iron solubility at the global level. Furthermore, correlations between iron oxidation state and

iron solubility at individual sampling locations suggest that photo-reduction may be a regionally important process for some aerosols.

5.2 Introduction

Adverse human health effects led to studies of aerosol chemistry being centered around air pollution. A shift from air pollution-based studies to biogeochemical studies of aerosol chemistry was spurred by the iron hypothesis, which links availability of the nutrient iron to marine primary productivity and ultimately to carbon dioxide sequestration (Boyd, Mackie, & Hunter, 2010; Martin, 1990; Schulz et al., 2012). Iron controls primary productivity in vast ocean regions (Moore et al., 2013). Iron fertilization studies have shown that the addition of iron to high nutrient low chlorophyll (HNLC) waters often increases primary productivity and create large algae blooms (Boyd et al., 2000; Buesseler et al., 2004; K. H. Coale et al., 2004; K.H. Coale et al., 1996; de Jong et al., 2012). In many remote ocean regions, deposition of aerosol iron is a major component of the iron budget. The factors that control the solubility of aerosol iron, and therefore bioavailability of iron, still remain unclear (Jickells et al., 2005; Mahowald et al., 2005). This has hampered the understanding of the aerosol iron's role in marine primary productivity as well as climatic processes associated with marine phytoplankton's ability to uptake and sequestration of large quantities of carbon dioxide (Schulz et al., 2012; Spolaor, Vallelonga, Cozzi, Gabrielli, et al., 2013).

Physical and chemical processes that occur in the atmosphere as well as source region and source material composition are all hypothesized to play a key role in the solubility of aerosol iron (Baker & Croot, 2010). The role that atmospheric processes play in the

solubilization of aerosol iron have been explored through studies looking at mineralogy, cloud processing, organic ligand reactions, and acidic reactions (Journet et al., 2008; Schulz et al., 2012; Shi et al., 2012; X. Zhu et al., 1993; Zhuang, Yi, Duce, & Brown, 1992a). Laboratory studies have shown acidic reactions enhance the solubility of aerosol iron (Journet et al., 2008; Nenes et al., 2011; Shi et al., 2009; Shi et al., 2015; Wiederhold et al., 2006; Witt, Mather, Baker, De Hoog, & Pyle, 2010). During atmospheric proton reactions, acidic species may overcome the carbonate buffer capacity of an aerosol particle, allowing the pH to reach values of 1 to 2 in aqueous solutions surrounding aerosol particles (Cwiertny et al., 2008; Ito & Feng, 2010). Under these acidic conditions, iron is more soluble (Oakes, Ingall, et al., 2012). Evidence for acidic reactions has been shown circumstantially in ambient aerosol samples, using indicators like non-seasalt sulfate and nitrate concentrations. However, the complexities of atmospheric chemistry are often not captured by these proxies (Hennigan, Izumi, Sullivan, Weber, & Nenes, 2015b; Nenes et al., 2011; Oakes, Ingall, et al., 2012; Sullivan et al., 2007). Models have estimated photo-chemical and organic ligand-promoted dissolution could play a key role in the transformation of aerosol iron (Johnson & Meskhidze, 2013), but these reactions are time intensive, complex, and may be hindered by acidic conditions (X. Zhu et al., 1993). The ultimate role of these processes in increasing the solubility of aerosol iron in ambient aerosol is still being deconvolved.

The composition of aerosol iron has been extensively studied through the use of bulk chemical extractions (Buck et al., 2006; Cornell & Schindler, 1987; Cornell & Schwertmann, 1996; Gao et al., 2013; Hoffmann et al., 1996; Wiederhold et al., 2006; N. Xu & Gao, 2008; X. Zhu et al., 1993). These studies yielded information about iron

oxidation state or may divide the composition of iron into operationally defined pools such as water-exchangeable, easily reducible, or oxidizable (Dabek-Zlotorzynska et al., 2003; Fittschen et al., 2008; Majestic et al., 2007; Winton et al., 2015). The application of spectroscopic techniques has allowed aerosol iron mineralogy to be determined more definitively (Hoffmann et al., 1996; R. C. Moffet et al., 2012; Oakes, Weber, et al., 2012; Weber et al., 2000). Using synchrotron-based elemental mapping and spectroscopy, aerosol samples collected in India, Bermuda, Greece, and during an Atlantic and Southern Ocean transects were characterized. These samples represent diverse source regions, having been exposed to varying degrees of mineral dust, anthropogenic, and marine influences. The diversity of this sample group of samples makes them ideal for examining relationships between composition, oxidation state, and acidity over a range of environments.

5.3 Methods

5.3.1 Sample collection

Five different sampling locations were used to capture aerosols with marine, anthropogenic, or mineral dust influences. The Finokalia Research Station (35.32°N, 25.67°E) is an isolated site away from both local and regional influences on the island of Crete, Greece, located 70 km from the nearest major city (Markaki et al., 2003). Samples of particulate matter with an aerodynamic diameter < 10 μm , PM₁₀, were collected on Teflon filters using a virtual impactor with an operational flow rate of 16.7 L min⁻¹. Fourteen samples were collected at the Finokalia site over a one to three-day period from 2009-2011 during which either North African or European air masses dominated.

Twenty-four hour particle collections were completed as part of the 2011 GEOTRACES Atlantic transect (Shelley et al., 2015). A total of nine samples were analyzed from the GEOTRACES collection: three marine, three North African, and three North American samples. Total suspended particle (TSP) samples were collected using Whatman-41 filters and a Tisch 5170-VBL high volume sampler operated on average with a face velocity of ~100 cm/sec (Shelley et al., 2015). The aerosol sampler was wind speed (> 0.5 m/s) and sector-controlled (± 60 deg from bow) to avoid contamination from ship's exhaust.

Weekly samples were collected at the Bermuda Institute of Ocean Sciences (32.24°N , 64.87°W), which receives primarily marine, North African, and North American influences. Total suspended particle sampling was conducted from June 2011 to June 2012. These samples were collected using a Tisch 5170-VBL high-volume Total Suspended Particle aerosol sampler using Whatman-41 filters and with a face velocity of ~100 cm/sec. Of the fifty-two samples that before were collected.

Daily sampling of PM₁₀ was completed at Amity University in Noida, India (28.5°N , 77.3°E). Samples were collected for seventeen hours with a high volume sampler where air was pulled through a size-fractionated cyclone inlet with a flow-rate of 1000 L min^{-1} . Samples were collected on Whatman GF/A filters (1820-866). Fourteen samples were collected in late September 2014, which falls outside of monsoon season when mineral dust is most prevalent (Srinivas, Sarin, & Rengarajan, 2014).

Further analysis was completed on three samples from Gao et al. (2013): C2, C9, and C13 (Gao et al., 2013). Briefly, shipboard aerosol sampling was carried out on the

icebreaker *R/V XueLong* along a transect from southwest Australia to the Australian Antarctic Casey Station. Sampling was conducted between November 2010 and March 2011. Teflon filters (Pall Corporation, 47 mm diameter, 1.0 μm pore size) were used to collect bulk aerosol samples with an operational flow rate of 15 L min^{-1} for 48 – 72 hours. To avoid contamination from the ship's exhaust, all sampling instruments were controlled by a wind sector and speed control system.

All aerosol samples were stored in the dark at -20°C until analysis. More detailed sampling information is available in Table 5.1-5.3 (5.6 Supporting Material).

5.3.2 HYSPLIT

Hybrid Single Particle Lagrangian Integrated Trajectory Model (HYSPLIT) back trajectories were completed for each sample using the GDAS half-degree meteorological archive in order to confirm the geographic origin of the air masses sampled (Draxier & Hess, 1998; Izquierdo et al., 2012). For the Bermuda Institute of Ocean Sciences (BIOS) and GEOTRACES samples, HYSPLIT back trajectories were calculated at 0 m, 500 m and 1000 m above ground level to confirm North American, North African, mixed, or marine provenance. For Southern Ocean and Indian samples HYSPLIT back trajectories were completed at 0 m, 500 m, and 3000 m above ground level. At the Finokalia Research Station, HYSPLIT back trajectories were calculated at 1000 m and 3000 m above ground level for five days (approximately atmospheric life time of dust aerosols) preceding sample collection. HYSPLIT back trajectories computed at 1000 m show the origin of air masses within the boundary layer; this height is chosen, rather than the more conventional heights of 0 m or 500 m to avoid orographic influences at this site.

HYSPLIT back trajectories were computed at 3000 m to identify dust events. At Finokalia Research Station, dust is either homogeneously distributed from 0 to about 3000 m, during spring and autumn dust events, or is found in a layer between 2500 – 4000 m during summer and autumn dust events (Kalivitis et al., 2007). The distance travelled in five days was estimated by using HYSPLIT back trajectories run in ensemble mode at 3000 m above ground level for all samples.

5.3.3 Total and soluble iron

Water soluble iron, hereafter referred to as soluble iron, was determined for all samples using the ferrozine technique (Stookey, 1970). Handling of the filters was conducted under a HEPA-filter laminar flow hood. A quarter filter was extracted into 10 mL of deionized water ($>18\text{ M}\Omega$) in a trace metal grade centrifuge tube by 30 min of ultrasonication. The extraction was followed by the removal of insoluble particles from the extract by a $0.2\ \mu\text{m}$ pore size syringe filter. Any dissolved Fe(III) in the sample was reduced to Fe(II) through the addition of $40\ \mu\text{M}$ solution of hydroxylamine hydrochloride added in a 1:100 ratio reagent to filter extracts. Samples were allowed to react with the hydroxylamine hydrochloride overnight. A 5 mM ferrozine solution which forms a colored complex with dissolved Fe(II) was then added in a 1:100 ratio reagent to filter extracts. After a ten-minute reaction, samples were spectrophotometrically measured at 562 nm (Oakes, Ingall, et al., 2012). Total iron was measured for Southern Ocean, GEOTRACES, and Bermuda Institute of Ocean Science samples using protocols described in Morton et al. (2013) (Gao et al., 2013; Kadko et al., 2015; Morton et al., 2013; Shelley et al., 2015). For BIOS and GEOTRACES samples, total iron was also measured via elemental densities collected from X-ray fluorescence maps to ensure total

iron could be reliably determined through synchrotron-based techniques (Oakes, Weber, et al., 2012), and for India and Finokalia Research Station samples, total iron was only determined using elemental densities collected from X-ray fluorescence maps.

5.3.4 Soluble ions and pH modelling

Ion chromatography was used to measure major soluble ions for samples from Finokalia Research Station and a subset of samples from the GEOTRACES transect and BIOS collection (Bardouki et al., 2003). Briefly, approximately 1/8th of each filter was extracted into 10 mL of nanopure water using an ultrasonic bath for 45 min. The filter extracts were then syringe filtered (PALL IC Acrodisc (PES), 0.45 µm, 13 mm) to remove any insoluble species. The acquired filtered solutions were analyzed for anions (Cl⁻, Br⁻, NO₃⁻, SO₄²⁻, HPO₄²⁻, C₂O₄²⁻) and cations (NH₄⁺, K⁺, Na⁺, Mg²⁺, Ca²⁺). Anions were determined using a Dionex-500 ion chromatograph equipped with an Ion Pac AS4A-SC column and an AG4A-SC precolumn, with an ASRS-300 suppressor. Anion separation was conducted with isocratic elution of NaHCO₃ (3.4 mM)/Na₂CO₃ (3.6 mM) as an eluent and a flow of 1.5 mL min⁻¹. For cations, an Ion Pac CS12A column and a CG12A guard column were used, with a CSRS-300 suppressor, under isocratic elution of 20 mM MSA (methanesulfonic acid) at a flow rate of 1.0 mL min⁻¹. The detection limit of the analysis was 20, 12, 40, 12 and 40 ppb for NH₄⁺, K⁺, Na⁺, Mg²⁺, and Ca²⁺, respectively, while the corresponding detection limit for all anions (Cl⁻, Br⁻, NO₃⁻, SO₄²⁻, HPO₄²⁻, and C₂O₄²⁻) was 20 ppb.

ISORROPIA was used to estimate the aerosol acidity of each aerosol sample (Fountoukis & Nenes, 2007; Nenes et al., 1998). This thermodynamic model will output

the concentration of species in the gas and aerosol (solid/liquid) phases, pH, and aerosol water. The size fraction of aerosols collected in these samples does conform to the equilibrium premise of ISORROPIA; therefore, this approach to aerosol pH modelling will only determine whether the samples are acidic or circa neutral. To compute the pH, knowledge of the relative humidity and temperature is needed; therefore, values characteristic of a humid marine boundary layer were assumed (80% Relative humidity; 293K).

5.3.5 Synchrotron Analysis

Aerosol iron composition was determined using the micro X-ray fluorescence capabilities at Argonne National Laboratory, Advanced Photon Source, Station 2-ID-D. In this study X-ray fluorescence microscopy and X-ray Absorption Near Edge Structure (XANES) spectroscopy were used to examine the iron in aerosol. In this study, these techniques work by providing incident X-rays of sufficient energy to bombard atoms, ejecting the electrons from the innermost shell electron shell. Subsequently, an outer shell electron may relax into the vacated position, emitting a characteristic fluorescence signal. The type, oxidation state, and structural arrangement of atoms in a particle are revealed as the ejected electron interacts with neighboring atoms and are reflected in XANES spectra (ED Ingall et al., 2011). Therefore, Fe-XANES spectra provide information on both oxidation state and the composition associated with the element of interest.

An energy dispersive Si-drift detector (Vortex EM, with a 50 mm² sensitive area, and a 12.5 μm Be window; SII NanoTechnology, Northridge, CA) was used to measure X-ray fluorescence of the samples. All measurements were conducted under a helium

atmosphere in order to minimize absorption and fluorescence caused by beam interactions with air. The effect of iron oxidation due to the X-ray beam was also examined by repeated XANES measurements totaling a ten seconds dwell time, longer than any was analyzed. These effects were found to be negligible. A randomly selected area of each filter sample (0.5 cm^2) was placed over a slot of an aluminum sample mount for analysis. The sample was initially analyzed in microscopic X-ray fluorescence mode to identify iron-containing particles on the filter. In this mode, the X-ray beam with a diameter of ca. 200 nm was scanned over a randomly selected filter area (typically 40 to $50 \mu\text{m}^2$) at a step size of $0.4 \mu\text{m}$ and 0.5 s dwell time to produce an elemental distribution map of the filter. The resulting XRF maps were used to identify iron-containing aerosol particles ($>1 \mu\text{m}$ diameter) for individual particle Fe-XANES spectroscopy.

Fe-XANES spectroscopy was conducted in bulk and individual particle modes. The composition of Saharan soil was only characterized in bulk mode. In bulk Fe-XANES mode, X-ray focusing optics (zone plate and order sorting aperture) were removed allowing characterization of iron present in ca. 0.4 mm^2 filter areas. In individual particle mode, iron-containing particles identified in elemental distribution maps were characterized with a focused beam with a $0.4 \mu\text{m}$ spot size. Of course, every particle could not be examined because of time constraints. Based on elemental maps, particles were selected to attempt to characterize as many different elemental iron associations as possible. Individual particle XANES spectroscopy represent the composition of the entire particle. In both bulk and individual particle modes, XANES scans were collected from 7100 to 7180 eV in 0.5 eV steps with 0.5–3 s dwell time per step.

5.3.6 Data reduction and analysis

Oxidation state was determined for each sample at the bulk and individual particle level by determining the pre-edge centroid of each Fe-XANES spectra. The pre-edge feature has been shown to be the most reliable indication of oxidation state for iron, and by interpolating between pre-edge centroid position % Fe(II) of standards, the relative abundance of Fe(II) can be determined for environmental samples (Bajt et al., 1994; Oakes, Weber, et al., 2012; Wilke et al., 2001).

Spectral data was normalized to account for variations in incoming X-ray flux and processed using the Athena software package (Ravel & Newville, 2005). In order to extract the most useful information from the spectral data, data reduction techniques were employed. A combination of principle component analysis, PCA, and k-means clustering were used to group like spectra (Marcus & Lam, 2014). The PCA algorithm used, built into Athena (Ravel & Newville, 2005), generates a scree plot where the number of principle components can be determined. Like spectra were merged (Ravel & Newville, 2005) to create an average spectra representing a cluster, and linear combination fitting was then completed for each cluster's Fe-XANES spectra using Athena (Ravel & Newville, 2005). These data reduction techniques were used on each sampling site, with the spectra being divided into bulk and individual particle Fe-XANES.

The linear combination fitting algorithm in Athena uses a database of known iron mineral standards (e.g., iron oxides, organics, silicates, sulfides, and sulfates) (Engall et al., 2013) run on the same synchrotron beamline to determine the phases

contributing to an unknown aerosol Fe-XANES spectra. An iterative process was used to refine the standard database used to model the sample spectra. First, exotic iron minerals unlikely to be major components of aerosol iron were excluded from the database (Oakes, Weber, et al., 2012). Second, the database was narrowed through elimination of standards with low contribution (i.e. less than 10%) or poor fit (i.e. high R-factor) during initial linear combination fitting. Also, insufficient quantities of a specific mineral or compound in a sample can also lead to underestimation of the specific compound during linear combination fitting (Dean Hesterberg, 2010); thus, iron composition was generalized to express broad chemical classes: iron(III) oxides, iron(III) sulfates, iron(III) phosphates, iron(II) sulfates, and iron(II) silicates. Athena uses a non-linear, least-squares minimization approach to fit spectra of unknown samples with standard material spectra, computing an error term, the R-factor, to quantify the goodness of a given linear combination fit. The linear combination of standards that yielded the lowest R-factor reflected the best fit (Ravel & Newville, 2005).

5.4 Results

5.4.1 Iron solubility

The solubility of iron varies widely at the five different sampling locations (Tables 5.4 & 5.5; 5.6 Supporting Material). The highest soluble iron concentrations were found in samples from India, which average 69.1 ng/m³ (Figure 5.1). European influenced samples from Finokalia Research Station exhibited the second highest levels of soluble iron (32.0 ng/m³) and contain on average four times more soluble iron than the

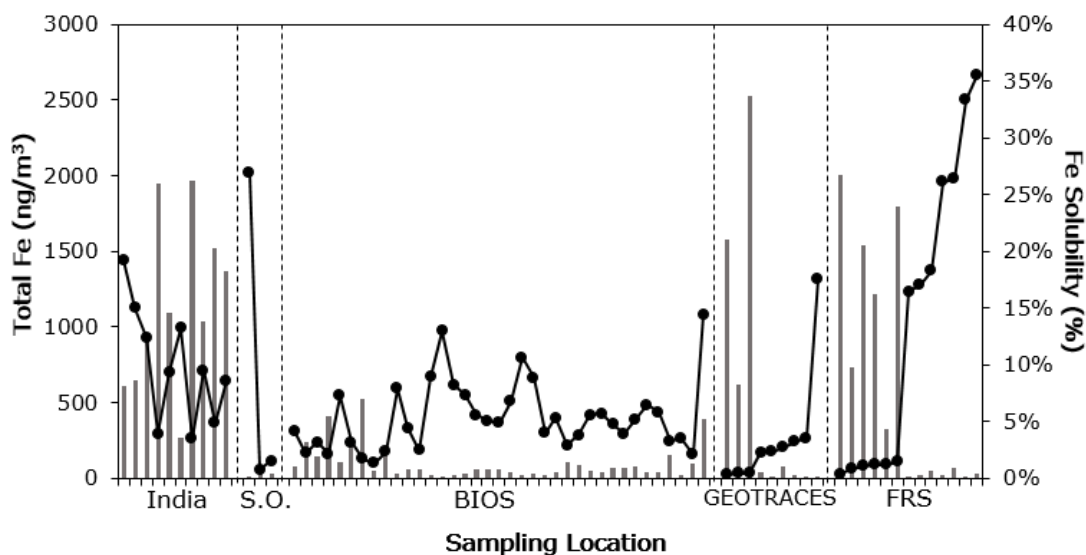


Figure 5.1 Total and Soluble Iron from Global Sample Set The total iron (grey bars) and soluble iron (black line) are shown for each sampling location. Here, S. O. represents samples collected from the Southern Ocean, and FRS represents samples collected from Finokalia Research Station. Generally, samples with the highest total iron have lower relative iron solubility.

North African samples that influence the same sampling location. North African influenced samples from the GEOTRACES collection site and the Finokalia Research Station both have similar quantities of soluble iron (6.0 ng/m^3 and 7.4 ng/m^3 , respectively). Samples with primarily marine influences, GEOTRACES and Southern Ocean samples, contain 0.18 ng/m^3 and 1.2 ng/m^3 of soluble iron, respectively. North American influenced samples from the GEOTRACES collection (1.3 ng/m^3) average the same magnitude of soluble iron as the year-long collection of BIOS samples (3.8 ng/m^3). When the relative solubility of iron is considered (percentage total iron that is water solubilized), European influenced samples from Finokalia Research Station have iron that is the most soluble, followed by samples dominated by marine influences. Samples from

the BIOS sampling location often contain a mixture of North African and North American influences. In these samples where North African mineral dust mixes with North American anthropogenic influences, aerosol iron often has a higher relative solubility than samples containing purer North African mineral dust (Figure 5.1).

5.4.2 Oxidation state

Samples from India contained primarily iron(III), with only one bulk sample showing an iron(II) signal (2.1%) (Table 5.4 & 5.5; 5.6 Supporting Material). This is similar to the findings for Southern Ocean samples, where two of the three samples contain only iron(III) and the final sample contains about 90% iron(III).

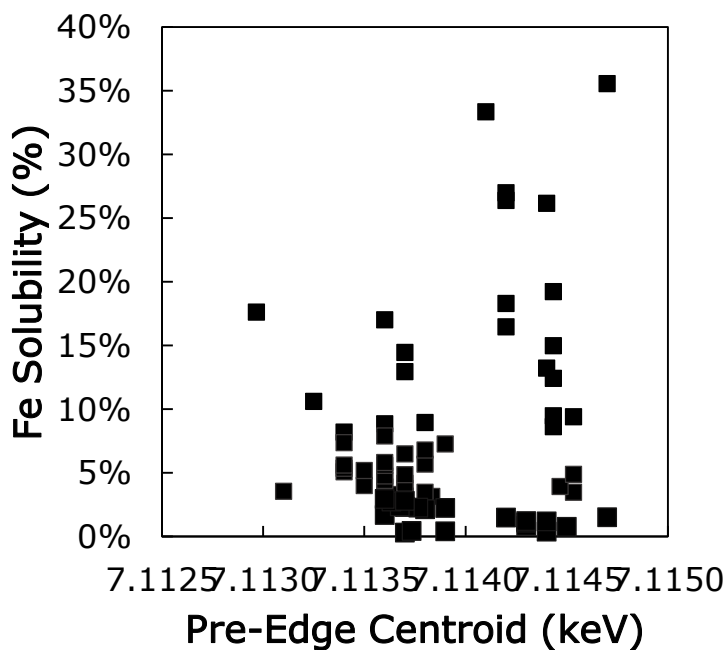


Figure 5.2 Solubility of Iron plotted against Oxidation State of Iron The pre-edge centroid (keV), a reliable indicator of iron oxidation state, has higher values for more oxidized iron. A wide range of pre-edge centroid values exist for each relative solubility of iron. This suggests that oxidation state is not an indicator of iron solubility on a global scale.

At Finokalia Research Station, samples with a European influence tend to contain more reduced iron (13.5% on average) than samples with a North African influence (3.5% on average). In contrast, GEOTRACES samples contain at least 30% iron(II) and the bulk level and can be dominated by iron(II) (>95%). Similar to GEOTRACES samples, BIOS samples contain at least 30% iron(II); however, at this sampling location, the maximum iron(II) in bulk samples is about 75%. Iron(II) is generally considered more soluble than iron(III), but this relationship cannot be seen in our data. When all the data is considered, there is a wide range of relative iron solubility at each oxidation state (Figure 5.2).

Because different processes could be at work to solubilize iron, the relative solubility was broken down into three different classes where samples with low relative iron solubility represents <3% soluble iron, mid-range relative iron solubility represents between 3% and 8% soluble iron, and high relative iron solubility represents >8% soluble iron. In this way mechanisms that more strongly affect iron with high or low relative solubility would be more visible. However, there was no clear relationship between iron oxidation state and any range of relative iron solubility.

5.4.3 Iron composition

At the bulk level, nearly all the samples are dominated by iron(III) oxides. There is also consistently iron(II) sulfates in most samples across all sampling locations (Figure 5.3). At both Finokalia Research Station and India, composition is consistent across all bulk samples (Table 5.6; 5.6 Supporting Material). Finokalia Research Station contains a combination of iron(III) oxides ($86.7 \pm 0.5\%$) and iron(II) sulfates ($13.3 \pm 0.5\%$). Indian samples also contain iron(III) oxides ($87.5 \pm 2.1\%$) and iron(II) sulfates ($12.5 \pm 1.5\%$). BIOS samples were also generally consistent in composition containing iron(III) oxides

($81.3 \pm 2\%$) and iron(II) sulfates ($18.7 \pm 1\%$); however, five samples contained a combination of iron(II) sulfates ($38.5 \pm 0.4\%$) and iron(III) sulfate ($61.5 \pm 20.8\%$).

Samples from the Southern Ocean belonged to one of two compositional groups. One group contained iron(III) oxides ($83.3 \pm 9.4\%$) and iron(II) sulfates ($16.7 \pm 0.7\%$), and one group contained iron(III) oxides ($53.0 \pm 1.9\%$) and ilmenite ($47.0 \pm 4\%$).

GEOTRACES samples contained three compositional groups at the bulk level. Samples contained either a combination of iron(III) oxides ($32.9 \pm 10.3\%$), iron(II) sulfate ($28.7 \pm 13.9\%$), and iron(III) phosphate ($38.4 \pm 9.0\%$); iron(III) oxides ($89.5 \pm 0\%$) and iron(II) sulfates ($10.5 \pm 4\%$); and iron(III) oxides ($47.2 \pm 12.1\%$), iron(III) phosphates ($10.7 \pm 11.1\%$), and iron(II) silicates ($42.1 \pm 11\%$).

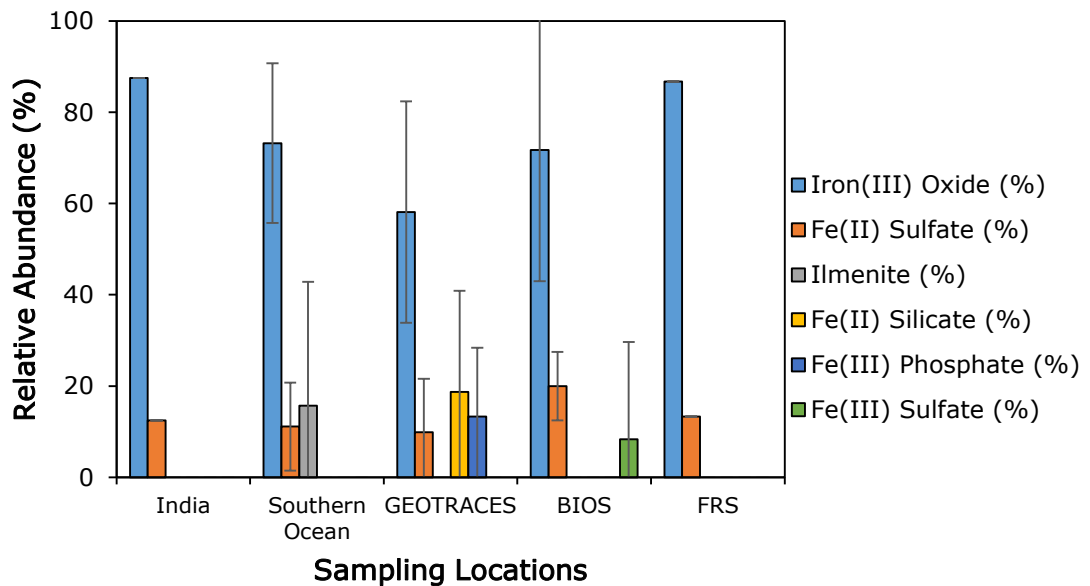


Figure 5.3 Average Bulk Iron Composition of each Sampling Location Iron(III) oxides and iron(II) sulfates are prevalent in all sampling locations. GEOTRACES and BIOS samples also contain iron(II) silicate, iron(III) sulfate, and iron(III) phosphate. The error bars represent plus or minus one standard deviation.

A total of 157 individual particles were examined for iron composition across the five different sampling locations. Individual particles were generally more diverse in composition than particles at the bulk level (Table 5.6; 5.6 Supporting Material). Individual particles sampled from India belong to three compositional groups and were either dominated by iron(III) oxides or iron(II) silicates (Table 5.6; 5.6 Supporting Material). Individual particles sampled from the Southern Ocean contained a combination of iron(III) oxides and iron(II) sulfate or were dominated by iron(III) phosphate. Individual particles from Finokalia Research Station contains largely iron oxides. Some particles also contain minor quantities of ilmenite, an iron oxide containing titanium. Individual particles sampled from Finokalia Research Station also contain ilmenite, but are largely dominated by iron(III) oxides. Individual particles from BIOS are largely a mixture of iron(III) oxides and iron(II) silicates. Individual particles sampled from the GEOTRACES transect had a strong presence of iron(II & III) sulfates and iron(III) phosphates with only minor contributions from iron(III) oxides.

5.5 Discussion

There are several hypotheses regarding the controls of aerosol iron solubility, including composition and mineralogy, oxidation state, cloud processing, acidic reactions, organic ligand, or photo-reduction (Baker & Croot, 2010; Shi et al., 2012; Zhuang et al., 1992b). In ambient aerosol samples, finding direct evidence of these mechanisms is challenging. Here, we focus primarily on the role composition, acidic reactions, oxidation state, and by extension photo-reduction, may play in the solubility of aerosol iron. Photo-reduction pathways have shown to play a key role in the transforming iron through both ligand assisted and unassisted mechanisms in laboratory settings

(Siefert et al., 1994; Siefert et al., 1996); however, nitric acid suppresses the formation of iron(II) at low pH, therefore pH can also act as a control of oxidation state of aerosol iron (Cwiertny et al., 2008). This also suggests that the various particle aging mechanisms, such as acidic reactions and photo-reduction, are likely not working simultaneously, which further confounds the identification of a particular mechanisms in a global sampling ambient aerosol samples.

When data from India, the Southern Ocean, BIOS, GEOTRACES, and Finokalia Research Station is considered together, there are no relationships between traditional factors that are linked to iron solubility. Composition ($R^2 = 0.037$) and oxidation state of iron ($R^2 = 0.058$) are both not correlated with the relative solubility of iron, which suggests that solubility of iron is not strongly tied to a specific iron phase or oxidation state (Figure 5.2 & 5.3). This is in contrast to studies that have routinely found that photo-reduction of iron occurs during the long-range transport of marine aerosol (Zhuang et al., 1992b). However, the lack of relationship between iron solubility and oxidation state could be due to insufficient transport time. Photo-reduction mechanisms working to solubilize mineral dust have been suggested to need more than 10 days of transport to show significant solubilization effects (Baker, French, & Linge, 2006). Composition can also dictate how photochemical mechanisms will proceed. Even within a general class of minerals, such as iron(III) oxides, various minerals have variable levels of susceptibility to photochemical processing (Cornell & Schindler, 1987).

Correlation have been seen between inorganic acids, sulfuric and nitric acid, and the solubility of aerosol iron suggesting that acidic reactions are a key factor controlling the solubility of iron in mineral dust (A. Kumar, Sarin, & Srinivas, 2010; Srinivas et al.,

2012; Srinivas et al., 2014). Here, there was no relationship between total inorganic acidity ($R^2 = 0.0016$), nitrate ($R^2 = 7 \times 10^{-6}$), or non-seasalt sulfate ($R^2 = 0.172$) and the relative solubility of iron. Furthermore, when pH was modelled with ISORROPIA, there was still no relationship that could be discerned between acidity and relative iron solubility (Figure 5.4). When considering samples with only low relative iron solubilities, a correlation between pH and aerosol iron solubility was evident ($R^2 = 0.67$). Because proton reactions only appear to be active at low levels of relative iron solubility, it is unclear whether proton reactions are activating solubilizing iron across all aerosol samples. Mineralogy of iron aerosol iron is key to understanding acidic reactions that may be at work. Heterogeneous mineralogy of aerosol iron can lead to iron with different levels of susceptibility to acid mobilization that act at different time scales (Z. Shi et al., 2011). Acidification of mineral dust has shown that iron will first undergo rapid iron dissolution, followed by a much slower rate (Z. Shi et al., 2011). These differences in rate of dissolution were linked to mineralogy, where the rapidly solubilizing iron is likely ferrihydrite, an amorphous iron oxide that can account for about 2% of the total iron. The iron phases that undergo slow dissolution under acidic conditions are likely crystalline iron oxide phases and clay minerals, which can account for up to 40% of the total iron (Z. Shi et al., 2011). The dominance of iron oxides in our samples (Figure 5.3), helps explain how the correlation between pH and iron solubility is only observed for samples with the lowest relative iron solubility (<3%) which are likely in the slowest extracting iron pool.

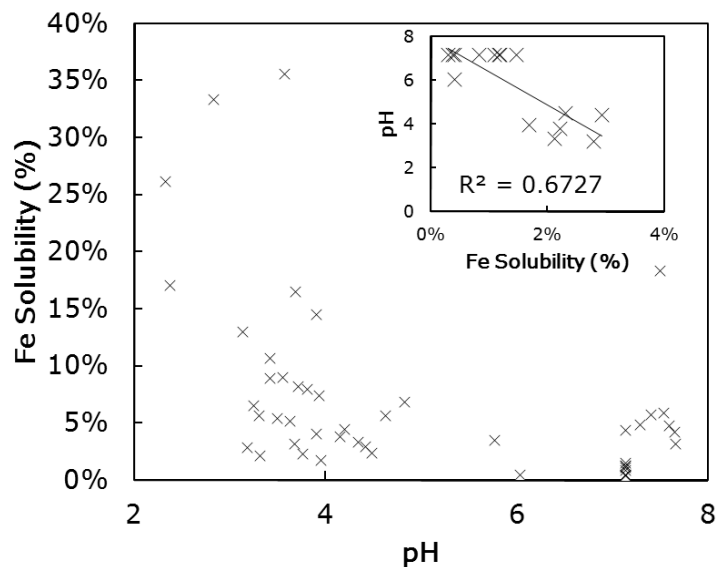


Figure 5.4 Iron Solubility as a Function of pH The pH, modelled by ISORROPIA, for samples from BIOS, GEOTRACES, and Finokalia Research Station, does not show a correlation with the relative solubility of iron when all the data is considered together; however, when just the data with low relative iron solubility is considered (<3% soluble iron), there is a notable correlation between pH and iron solubility ($R^2 = 0.67$).

Alteration of clay mineral phases to produce soluble iron minerals, such as ferrihydrite, have been shown to occur as a result of chemical reactions during atmospheric transport (Y. Takahashi, Higashi, Furukawa, & Mitsunobu, 2011). While traditional indicators of aerosol acidity, such as pH, suggest that acidic reactions may be at work to solubilize iron, our observations of iron phosphates and iron(II & III) sulfates provide further support that acidic reactions are occurring. Iron phosphates and sulfates do not occur in natural environments at high concentrations. To account for the concentrations of these phases seen in aerosol samples across all sampling locations, secondary atmospheric processes are likely at work. Iron phosphates and sulfates could

be the result acidic processes that solubilize iron and phosphorus minerals through reactions with sulfuric and nitric acid species. This could create an aqueous solution rich in iron, phosphorus, and sulfur which favor the precipitation of secondary mineral phases (Nenes et al., 2011). However, these reactions can be buffered by carbonate minerals found commonly found mineral dust (Ito & Feng, 2011; Meskhidze et al., 2003), so the carbonate buffer capacity of the particles must be overcome for these reactions to proceed. Furthermore, aerosol pH undergoes diel fluctuations (Nikolaou et al., 2015) that will cause the process of acidic transformation to be slow. Three to five days are necessary to solubilize 1-2% of iron under acidic conditions of a deliquescent mineral dust particle (Guo et al., 2015; Meskhidze et al., 2003). The buffering effect of carbonate present in mineral dust combined with the diel fluctuations of pH helps explain the finding of secondary phosphates and sulfates that could stem from acidic reactions as well as the iron(III) oxides in particles where acids were not able to overcome the carbonate buffer.

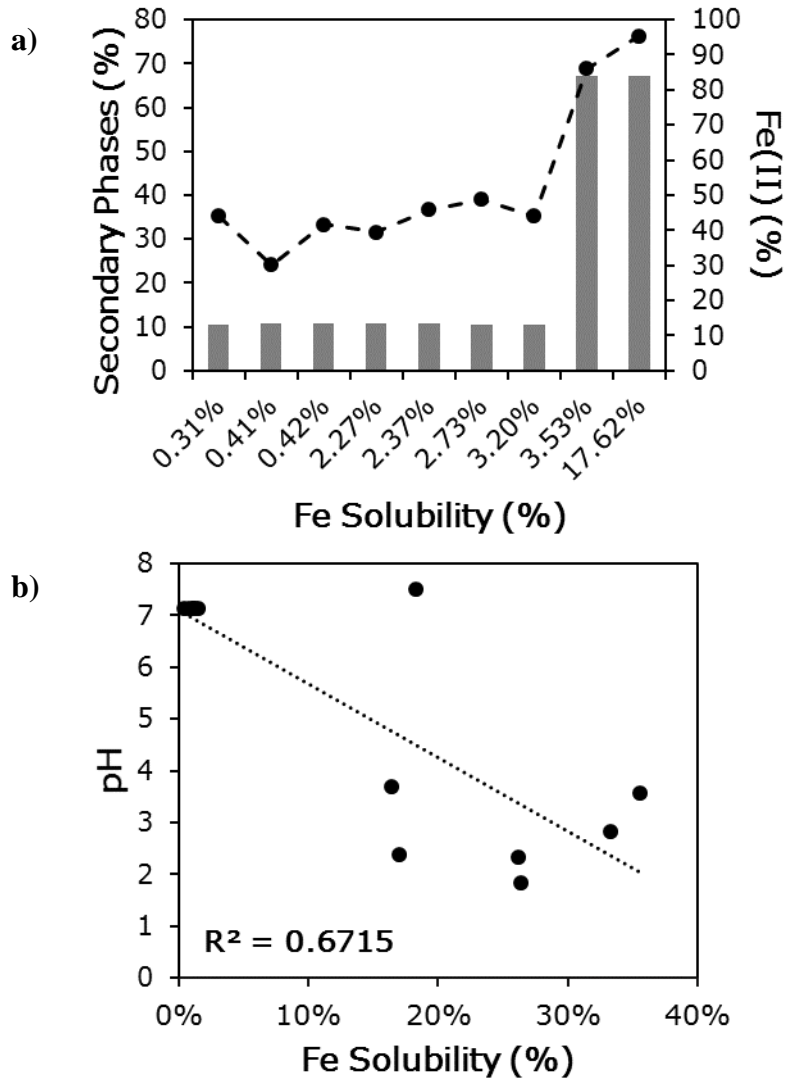


Figure 5.5 Factors Affecting the Solubility of Iron at Individual Collection Locations (a) Samples from the GEOTRACES collection were more soluble when they contained either more iron(II) (black line) or more secondary phases (grey bars). Secondary phases include iron(II & III) sulfate and iron phosphate and are labelled as secondary phases because these are phases that possibly form through secondary reactions that occur in the atmosphere. (b) Samples from Finokalia Research Station show a correlation between pH, modelled via ISORROPIA, and relative solubility of iron.

The source region of the aerosol may also influence the solubility of iron, where samples originating in regions of high anthropogenic influence have greater soluble iron than areas dominated by mineral dust (Sedwick, Sholkovitz, & Church, 2007; E. R. Sholkovitz, Sedwick, & Church, 2009). Even within North African samples, different source regions showed significant variability in chemical weathering (Zongbo Shi et al., 2011). In this study, samples collected at the GEOTRACES and Finokalia Research Station locations show trends that cannot be observed in the larger data set. At the GEOTRACES collection site, composition and oxidation state show strong correlation with iron solubility. In these samples, increased iron(II) correlated to increased iron solubility (Figure 5.5a), which could be evidence of a reductive process, such as photo-reduction. Moreover, samples with the highest quantities of iron(II & III) sulfates and iron(III) phosphates, phases that are likely formed as a result of secondary processes that occur in the atmosphere, also contained the most soluble iron (Figure 5.5a). At Finokalia Research Station, pH was related to the relative solubility of iron ($R^2 = 0.67$) (Figure 5.5b). At this sampling location, two distinct air masses tend to affect the sampling location: anthropogenically influenced European air masses and mineral dust laden North African air masses. This strong dichotomy helps create this relationship. North African air masses exhibit low relative solubility and high pH; while samples from European air masses have higher relative solubility and lower pH, likely due to the anthropogenic influences in these air masses (Sedwick et al., 2007; E. R. Sholkovitz et al., 2009).

In general, the total and soluble iron trends seen in data from this study are similar to those seen in other global aerosol iron data sets (Buck et al., 2006; Fu et al., 2014; Gao et al., 2013; A. Kumar et al., 2010; A. Kumar & Sarin, 2009; Srinivas et al., 2014; T.

Takahashi et al., 2013). For aerosol iron, samples that are high in total iron have low relative iron solubility, and samples with low total iron have higher relative iron solubility (Edward R. Sholkovitz, Sedwick, Church, Baker, & Powell, 2012). This could reflect the effects of aerosol source region, where aerosols with high total iron tend to come from mineral dust sources, which can contain significant buffer capacity. This is in contrast than aerosols from anthropogenically influenced air masses that have lower buffer capacity and more acidic species. However, studies of mineral dust have suggested a physical control over the solubility of aerosol iron where larger particles are removed during atmospheric transport (Baker & Jickells, 2006). This leaves smaller particles with a higher surface area to volume ratio where more iron will be exposed at the particle surface, creating higher iron solubility (Baker & Jickells, 2006; A. Kumar & Sarin, 2009). These physical processes along with ligand promoted iron dissolution are mechanisms that were not evaluated in this study. The presence of ligands is thought to stabilize iron(II) in solution and can also participate in ligand mediated photochemical reactions (Paris et al., 2011; Wozniak et al., 2013). The occurrence of these physical and chemical processes in ambient aerosol could help explain the lack of correspondence between aerosol iron solubility and composition, oxidation state, and pH in the global dataset.

In the natural environment, the various chemical transport phenomena of particle aging may not only occur on different time scales, but may have persistent effects on each other. For example, one study noted marine samples to be 5-17 times more soluble than samples containing significant anthropogenic influence when acidified to the same pH, and this increased solubility was attributed to conversion of iron(III) to iron(II) via

photo-reduction (Zhuang et al., 1992b). This demonstrates that one factor alone cannot be considered to control the solubility of aerosol iron. The observed variations in composition, oxidation state, pH, and solubility of aerosol iron shown here suggest that chemical transformations during atmospheric transport occur on a global scale. However, this data also show that one universal rule of iron solubility should not be applied to estimate the solubility of aerosol iron. Source region, pH, oxidation state, and composition all affected the solubility of aerosol iron. This emphasizes the need to conduct further *in situ* examinations of particle aging mechanisms on a regional basis. In this way, inputs of potentially bioavailable iron(II) to the marine environment will be most accurately quantified.

5.6 Supporting Materials

Table 5.1 Sample Collection Information for Indian, Southern Ocean, Finokalia Research Station, and GEOTRACES Samples

Sample ID	Collection	Sample Deployment	Sample Collection	Predominant Source	Volume (m ³)
SF1	India	9/16/2015	9/17/2015	mixed	1020
SF2	India	9/18/2015	9/19/2015	mixed	1020
SF3	India	9/19/2015	9/20/2015	mixed	1020
SF5	India	9/20/2015	9/21/2015	mixed	1020
SF6	India	9/21/2015	9/22/2015	mixed	1020
SF4	India	9/22/2015	9/23/2015	mixed	1020
SF7	India	9/23/2015	9/24/2015	mixed	1020
SF8	India	9/24/2015	9/25/2015	mixed	1020
SF9	India	9/25/2015	9/26/2015	mixed	1020
SF10	India	9/26/2015	9/27/2015	mixed	1020
SF11	India	9/27/2015	9/28/2015	mixed	1020
SF12	India	9/28/2015	9/29/2015	mixed	1020
SF13	India	9/29/2015	9/30/2015	mixed	1020
SF14	India	9/30/2015	10/1/2015	mixed	1020
C2	Southern Ocean	11/30/2010	12/2/2010	Open Ocean	86.4
C13	Southern Ocean	3/2/2011	3/4/2011	Open Ocean	86.4
C9	Southern Ocean	2/12/2011	2/15/2011	Open Ocean	86.4
6250	GEOTRACES	11/7/11	11/8/11	N. American	92.10
6319	GEOTRACES	11/8/11	11/9/11	N. American	74.96
6546	GEOTRACES	11/12/11	11/13/11	N. American	114.32
6964	GEOTRACES	11/20/11	11/21/11	Marine	95.01
7245	GEOTRACES	11/24/11	11/26/11	Marine	161.00
7587	GEOTRACES	11/30/11	12/1/11	Marine	115.54
7899	GEOTRACES	12/5/11	12/6/11	N. Africa	116.01
7946	GEOTRACES	12/6/11	12/7/11	N. Africa	137.92
8004	GEOTRACES	12/7/11	12/8/11	N. Africa	108.81
BL_165	FRS	12/18/09	12/19/09	SW	45.59
BL_185	FRS	2/10/10	2/11/10	SW	38.37
BL_197	FRS	3/10/10	3/11/10	SW	48.68
BL_206	FRS	3/31/10	4/1/10	SW	51.38
BL_213	FRS	4/16/10	4/17/10	SW	56.10
BL_305	FRS	11/10/10	11/11/10	S	58.72
BL_324	FRS	12/24/10	12/25/10	S	38.87
BL_260	FRS	7/28/10	7/29/10	NW	49.32
BL_274	FRS	9/6/10	9/7/10	NE	67.16
BL_275	FRS	9/9/10	9/10/10	N	56.67
BL_277	FRS	9/13/10	9/14/10	NE	70.06
BL_330	FRS	1/7/11	1/8/11	NW	47.79
BL_333	FRS	1/14/11	1/15/11	N	45.80
BL_344	FRS	2/9/11	2/10/11	NE	43.83

Table 5.2 Sample collection information for samples collected at the Bermuda Institute of Ocean Science

Sample Deployment	Sample Collection	Predominant Source	Total Volume (m³)
26/Jun/2011 10:19	2/Jul/2011 13:50	mixed	838.88
20/Jul/2011 13:30	26/Jul/2011 8:40	Saharan	774.29
26/Jul/2011 16:42	1/Aug/2011 9:13	mixed	715.94
1/Aug/2011 9:21	7/Aug/2011 11:00	Saharan	714.56
7/Aug/2011 11:06	13/Aug/2011 10:18	N. Am/Caribbean	784.84
13/Aug/2011 10:21	19/Aug/2011 13:22	Saharan	808.20
19/Aug/2011 13:25	25/Aug/2011 9:30	Saharan	768.70
6/Sep/2011 9:05	12/Sep/2011 8:51	Saharan	802.46
26/Sep/2011 8:30	30/Sep/2011 10:02	Saharan	542.86
30/Sep/2011 10:05	6/Oct/2011 14:38	mixed	827.92
6/Oct/2011 14:42	12/Oct/2011 10:25	N. Am	779.79
18/Oct/2011 10:12	24/Oct/2011 9:00	Saharan	795.22
5/Nov/2011 10:49	11/Nov/2011 15:50	mixed	831.69
11/Nov/2011 15:54	17/Nov/2011 14:23	N. Am	934.11
17/Nov/2011 14:27	23/Nov/2011 14:45	N. Am	806.96
23/Nov/2011 14:47	29/Nov/2011 15:33	mixed	793.56
5/Dec/2011 9:03	11/Dec/2011 9:25	North	795.74
22/Jan/2012 15:29	28/Jan/2012 10:12	mixed	769.01
28/Jan/2012 10:15	3/Feb/2012 9:20	N. Am	803.10
3/Feb/2012 9:25	9/Feb/2012 9:23	N. Am	769.74
15/Feb/2012 9:30	21/Feb/2012 8:56	N. Am	806.47
21/Feb/2012 9:00	27/Feb/2012 9:18	mixed	801.73
5/Mar/2012 8:36	10/Mar/2012 10:19	mixed	684.31
16/Mar/2012 9:54	22/Mar/2012 9:43	mixed	794.18
28/Mar/2012 9:45	3/Apr/2012 8:54	N. Am	777.83
3/Apr/2012 8:57	9/Apr/2012 9:34	N. Am	797.32
9/Apr/2012 9:36	13/Apr/2012 11:15	mixed	806.72
27/Apr/2012 9:44	3/May/2012 9:30	mixed	789.34
3/May/2012 9:36	9/May/2012 9:26	North	777.73
9/May/2012 9:30	15/May/2012 10:47	mixed	787.57
15/May/2012 10:48	21/May/2012 9:09	Saharan	795.67
27/May/2012 10:26	2/Jun/2012 9:51	mixed	802.12
2/Jun/2012 9:55	8/Jun/2012 9:10	N. Am	756.62
14/Jun/2012 9:28	20/Jun/2012 14:00	mixed	831.43
26/Jun/2012 15:18	2/Jul/2012 9:28	mixed	772.86

Table 5.3 Sample Collection Locations

Collection	Latitude	Longitude
BIOS	32.24 °N	64.87 °W
FRS	35.32 °N	25.67 °E
GEOTRACES	39.71 °N	69.86 °W
	39.70 °N	69.79 °W
	38.33 °N	68.87 °W
	31.75 °N	64.17 °W
	29.70 °N	56.82 °W
	25.55 °N	43.54 °W
	22.37 °N	35.62 °W
	20.88 °N	32.62 °W
19.43 °N	29.38 °W	
Southern Ocean	56 °S	94 °E
	69 °S	77 °E
	44 °S	96 °E
India	28.5 °N	77.3 °E

Table 5.4 Bermuda Institute of Ocean Science Aerosol Data

Sample Deployment	pH at 80% RH	Fe(II) (%)	Pre-Edge Centroid (keV)	Total Fe (ng/m ³)	Soluble Fe (%)	Travelled in 5 days (km)
26/Jun/2011 10:19	7.7	44.1	7.1137	80.4	4.2%	1600
2/Jul/2011 14:08	-	-	-	52.7	1.8%	1360
14/Jul/2011 9:17	-	-	-	63.1	1.0%	2771
20/Jul/2011 13:30	3.8	30.1	7.1139	238.6	2.2%	1586
26/Jul/2011 16:42	7.7	44.1	7.1137	142.6	3.1%	2136
1/Aug/2011 9:21	3.3	37.1	7.1138	414.2	2.1%	1521
7/Aug/2011 11:06	-	30.1	7.1139	108.9	7.3%	2229
13/Aug/2011 10:21	3.7	34.7	7.1138	265.9	3.1%	1950
19/Aug/2011 13:25	4.0	51.0	7.1136	521.9	1.7%	1300
25/Aug/2011 9:33	-	-	-	98.1	0.4%	2064
31/Aug/2011 11:17	-	-	-	49.4	1.3%	1857
6/Sep/2011 9:05	3.2	44.1	7.1137	128.2	2.8%	2021
12/Sep/2011 8:55	-	-	-	98.3	1.3%	2071
26/Sep/2011 8:30	4.5	44.1	7.1137	153.5	2.3%	1260
30/Sep/2011 10:05	3.8	51.0	7.1136	28.0	7.9%	2736
6/Oct/2011 14:42	4.2	51.0	7.1136	60.0	4.4%	3714
12/Oct/2011 10:32	-	-	-	55.7	2.5%	2171
18/Oct/2011 10:12	3.6	37.1	7.1138	23.7	8.9%	2221
24/Oct/2011 9:05	-	-	-	34.7	1.5%	3569
31/Oct/2011 9:48	-	-	-	21.4	8.5%	1790
5/Nov/2011 10:49	3.1	44.1	7.1137	15.4	13.0%	2814
11/Nov/2011 15:54	3.7	65.0	7.1134	25.6	8.2%	4186
17/Nov/2011 14:27	3.9	65.0	7.1134	30.6	7.4%	3886
23/Nov/2011 14:47	4.6	65.0	7.1134	62.6	5.6%	4021
5/Dec/2011 9:03	-	65.0	7.1134	58.2	5.1%	3857
22/Jan/2012 15:29	7.3	44.1	7.1137	55.8	4.8%	3629
28/Jan/2012 10:15	4.8	37.1	7.1138	36.4	6.8%	4371
3/Feb/2012 9:25	3.4	75.5	7.1133	19.3	10.6%	4086
15/Feb/2012 9:30	3.4	51.0	7.1136	26.0	8.8%	4386
21/Feb/2012 9:00	3.9	58.0	7.1135	25.5	4.0%	5243
27/Feb/2012 9:20	-	-	-	35.7	1.9%	4280
5/Mar/2012 8:36	3.5	65.0	7.1134	43.3	5.3%	4520
10/Mar/2012 10:23	-	-	-	65.0	0.8%	2800
16/Mar/2012 9:54	4.4	51.0	7.1136	109.5	2.9%	3171
22/Mar/2012 9:45	-	-	-	88.4	1.9%	2336
28/Mar/2012 9:45	4.2	44.1	7.1137	84.6	3.8%	4271
3/Apr/2012 8:57	3.3	51.0	7.1136	53.3	5.6%	3607
9/Apr/2012 9:36	7.4	37.1	7.1138	44.0	5.7%	4580
13/Apr/2012 11:21	-	-	-	89.7	2.4%	3053
27/Apr/2012 9:44	7.6	51.0	7.1136	65.9	4.7%	2607
3/May/2012 9:36	-	51.0	7.1136	69.0	3.9%	3164
9/May/2012 9:30	3.6	58.0	7.1135	74.0	5.2%	2986
15/May/2012 10:48	3.3	44.1	7.1137	37.3	6.5%	1414
21/May/2012 9:15	-	-	-	46.1	1.3%	1857
27/May/2012 10:26	7.5	51.0	7.1136	40.9	5.8%	1614
2/Jun/2012 9:55	4.3	47.6	7.1137	155.1	3.3%	2814
8/Jun/2012 9:16	-	-	-	35.3	1.4%	3229
14/Jun/2012 9:28	5.8	37.1	7.1138	21.7	3.5%	1329
20/Jun/2012 14:05	-	-	-	93.3	2.1%	1686
26/Jun/2012 15:18	3.9	44.1	7.1137	392.3	14.4%	2686

Table 5.5 India, GEOTRACES, Southern Ocean, and Finokalia Research Station Aerosol Data

Sample ID	Collection	pH at 80% RH	% Fe(II)	Pre-Edge Centroid (keV)	Total Fe (ng/m ³)	Soluble Fe (%)	Travelled in 5 days (km)
SF1	India	-	0.0	7.1145	-	-	500
SF2	India	-	0.0	7.1144	612.5	19.2%	2000
SF3	India	-	0.0	7.1144	647.8	15.0%	1500
SF5	India	-	0.0	7.1144	937.1	12.4%	1200
SF6	India	-	0.0	7.1144	-	-	1800
SF4	India	-	0.0	7.1145	1947.6	3.9%	3000
SF7	India	-	0.0	7.1145	1018.8	9.4%	2000
SF8	India	-	0.0	7.1144	271.9	13.2%	1600
SF9	India	-	0.0	7.1144	-	-	1500
SF10	India	-	0.0	7.1145	1972.2	3.5%	1000
SF11	India	-	0.0	7.1144	1039.4	9.5%	2400
SF12	India	-	2.1	7.1143	-	-	1950
SF13	India	-	0.0	7.1145	1517.2	4.9%	2500
SF14	India	-	0.0	7.1144	1365.8	8.6%	2600
C2	Southern Ocean	-	9.1	7.1142	10.0	27.0%	3500
C13	Southern Ocean	-	0.0	7.1145	38.0	0.8%	4800
C9	Southern Ocean	-	0.0	7.1147	30.0	1.5%	1650
6250	GEOTRACES	-	44.1	7.1137	25.7	3.2%	2100
6319	GEOTRACES	-	48.7	7.1136	80.2	2.7%	3300
6546	GEOTRACES	-	39.4	7.1138	38.3	2.3%	5500
6964	GEOTRACES	-	86.0	7.1131	1.7	3.5%	4000
7245	GEOTRACES	-	95.3	7.1130	0.9	17.6%	1400
7587	GEOTRACES	-	45.8	7.1137	13.6	2.4%	3000
7899	GEOTRACES	6.0	30.1	7.1139	623.5	0.4%	2000
7946	GEOTRACES	7.1	44.1	7.1137	1580.0	0.3%	2000
8004	GEOTRACES	7.1	41.7	7.1137	2529.8	0.4%	2100
BL_165	FRS	7.1	2.1	7.1143	1537.2	1.1%	3400
BL_185	FRS	7.1	-	-	3455.3	4.3%	5500
BL_197	FRS	7.1	2.1	7.1143	734.6	0.8%	5600
BL_206	FRS	7.1	0.0	7.1144	1213.7	1.2%	3400
BL_213	FRS	7.1	0.0	7.1144	2009.0	0.4%	2700
BL_305	FRS	7.1	2.1	7.1143	323.6	1.2%	1950
BL_324	FRS	7.1	9.1	7.1142	1798.4	1.5%	2300
BL_260	FRS	7.5	9.1	7.1142	52.1	18.3%	1050
BL_274	FRS	2.4	51.0	7.1136	18.0	17.0%	1500
BL_275	FRS	1.8	9.1	7.1142	73.1	26.4%	1300
BL_277	FRS	2.3	0.0	7.1144	18.8	26.2%	1350
BL_330	FRS	3.7	9.1	7.1142	1.9	16.4%	1800
BL_333	FRS	2.8	16.1	7.1141	14.4	33.3%	2400
BL_344	FRS	3.6	0.0	7.1147	28.0	35.6%	1650

Table 5.6 Composition of Bulk Aerosol and Individual Aerosol Particle Samples

Sample Site	Type	Group Size	Fe(III) Oxide	Fe(II) Sulfate	Fe(III) Sulfate	Fe(III) Phosphate	Ilmenite	Jarosite	Fe(II) Silicate
India	Bulk	14	87.5 ± 2.1%	12.5 ± 1.5%	-	-	-	-	-
	Individual Particle	34	92.6 ± 0.2%	7.4 ± 0.2%	-	-	-	-	-
		15	100 ± 3.9%	-	-	-	-	-	-
	9	25.2 ± 2.8%	-	-	-	-	-	-	74.8 ± 3.9%
	Bulk	2	83.3 ± 9.4%	16.7 ± 0.7%	-	-	-	-	-
Southern Ocean	Bulk	1	53.0 ± 1.9%	-	-	-	47.0 ± 4%	-	-
		4	-	11.7 ± 0.4%	-	88.3 ± 5.5%	-	-	-
	Individual Particle	3	52.2 ± 30.5%	20.6 ± 1.7%	-	-	-	26.9 ± 60.4%	-
	4	-	2.7 ± 4.3%	-	-	-	38.6 ± 42.6%	58.6 ± 73.7%	-
	Bulk	13	86.7 ± 0.5%	13.3 ± 0.5%	-	-	-	-	-
Finokalia Research Station	Individual Particle	24	94.7 ± 0.3%	5.3 ± 0.3%	-	-	-	-	-
	2	74.8 ± 5.6%	-	-	-	25.2 ± 5.6%	-	-	-
BIOS	Bulk	12	81.3 ± 2%	18.7 ± 1%	-	-	-	-	-
	20	83.9 ± 0%	16.1 ± 0%	-	-	-	-	-	-
	5	-	38.5 ± 0.4%	61.5 ± 20.8%	-	-	-	-	-
	Individual Particle	6	17.5 ± 36%	-	-	-	-	-	82.5 ± 11%
	12	71.5 ± 1%	-	-	-	-	-	-	28.5 ± 3%
GEOTRACES	Bulk	10	84.5 ± 4%	-	-	-	-	-	15.5 ± 2%
		2	47.2 ± 12.1%	-	-	10.7 ± 11.1%	-	-	42.1 ± 11%
	3	89.5 ± 0.3%	10.5 ± 4%	-	-	-	-	-	-
	4	32.9 ± 10.3%	28.7 ± 13.9%	-	-	38.4 ± 9.0%	-	-	-
	Individual Particle	27	-	69.2 ± 4%	-	-	30.8 ± 4%	-	-
6	-	36.6 ± 2%	63.4 ± 59%	-	-	-	-	-	
1	10.8 ± 8.9%	26.6 ± 2%	-	-	62.6 ± 9.6%	-	-	-	

APPENDIX A

STANDARD DATABASES

Phosphorus near edge X-ray fluorescence spectroscopy (NEXFS) was collected for a number of organic phosphorus standards. The phosphorus NEXFS data is available as a Microsoft Excel file. Sulfur NEXFS data was also collected for a number of sulfur minerals and compounds. These data are available as a Microsoft Excel file. These databases of standards are submitted electronically with this thesis.

REFERENCES

- Ajiboye, B., Akinremi, O. O., & Jurgensen, A. (2007). Experimental validation of quantitative XANES analysis for phosphorus speciation. *Soil Science Society of America Journal*, 71(4), 1288-1291. doi: 10.2136/sssaj2007.0007
- Alexander, B., Park, R. J., Jacob, D. J., Li, Q. B., & Yantosca, R. M. (2005). Sulfate formation in sea-salt aerosols: Constraints from oxygen isotopes. *Journal of Geophysical Research*, 110(D10307). doi: 10.1029/2004JD005659
- Anderson, L. D., Faul, K. L., & Paytan, A. (2010). Phosphorus associations in aerosols: What can they tell us about P bioavailability? *Marine Chemistry*, 120(1-4), 44-56. doi: 10.1016/j.marchem.2009.04.008
- Andersson, J. T., Hegazi, A. H., & Roberz, B. (2006). Polycyclic aromatic sulfur heterocycles as information carriers in environmental studies. *Analytical and Bioanalytical Chemistry*, 386(4), 891-905. doi: 10.1007/s00216-006-0704-y
- Artaxo, P., Martins, J. V., Yamasoe, M. A., Procopio, A. S., Pauliquevis, T. M., Andreae, M. O., . . . Leal, A. M. C. (2002). Physical and chemical properties of aerosols in the wet and dry seasons in Rondonia, Amazonia. *Journal of Geophysical Research-Atmospheres*, 107(D20). doi: 10.1029/2001jd000666
- Aspila, K.I., Agemian, H., & Chau, A.S.Y. (1976). A semi-automated method for the determination of inorganic, organic and total phosphate in sediments. *Analyst*, 101, 187-197.
- Atkinson, M. J., & Smith, S. V. (1983). C:N:P ratios of benthic marine plants. *Limnol. Oceanogr.*, 28, 568-574.
- Baines, S. B., Twining, B. S., Vogt, S., Balch, W. M., Fisher, N. S., & Nelson, D. M. (2011). Elemental composition of equatorial Pacific diatoms exposed to additions of silicic acid and iron. *Deep-Sea Research Part II-Topical Studies in Oceanography*, 58(3-4), 512-523. doi: 10.1016/j.dsr2.2010.08.003
- Bajt, S., Sutton, S. R., & Delaney, J. S. (1994). X-ray microprobe analysis of iron oxidation-states in silicates and oxides using X-ray -absorption near-edge structure (XANES). *Geochimica Et Cosmochimica Acta*, 58(23), 5209-5214. doi: 10.1016/0016-7037(94)90305-0
- Baker, A. R., & Croot, P. L. (2010). Atmospheric and marine controls on aerosol iron solubility in seawater. *Marine Chemistry*, 120, 4-13. doi: 10.1016/j.marchem.2008.09.003

- Baker, A. R., French, M., & Linge, K. L. (2006). Trends in aerosol nutrient solubility along a west-east transect of the Saharan dust plume. *Geophysical Research Letters*, 33(7). doi: 10.1029/2005gl024764
- Baker, A. R., & Jickells, T. D. (2006). Mineral particle size as a control on aerosol iron solubility. *Geophysical Research Letters*, 33(17). doi: 10.1029/2006gl026557
- Baker, A. R., Jickells, T. D., Witt, M., & Linge, K. L. (2006). Trends in the solubility of iron, aluminium, manganese and phosphorus in aerosol collected over the Atlantic Ocean. *Marine Chemistry*, 98(1), 43-58. doi: 10.1016/j.marchem.2005.06.004
- Baker, A. R., Weston, K., Kelly, S. D., Voss, M., Streu, P., & Cape, J. N. (2007). Dry and wet deposition of nutrients from the tropical Atlantic atmosphere: Links to primary productivity and nitrogen fixation. *Deep-Sea Research Part I-Oceanographic Research Papers*, 54, 1704-1720.
- Bao, L. M., Lin, J., Liu, W. , Lu, W. Z., Zhang, G. L., Li, Y., . . . Hu, T. D. (2009). Investigation of sulfur speciation in particles from small coal-burning boiler by XANES spectroscopy. *Chinese Physics C*, 33(11), 1001-1005.
- Bardouki, H., Liakakou, H., Economou, C., Sciare, J., Smolik, J., Zdimal, V., . . . Mihalopoulos, N. (2003). Chemical composition of size-resolved atmospheric aerosols in the eastern Mediterranean during summer and winter. *Atmospheric Environment*, 37(2), 195-208. doi: 10.1016/S1352-2310(02)00859-2
- Bauer, H., Kasper-Giebl, A., Loflund, M., Giebl, H., Hitzemberger, R., Zibuschka, F., & Puxbaum, H. (2002). The contribution of bacteria and fungal spores to the organic carbon content of cloud water, precipitation and aerosols. *Atmospheric Research*, 64(1-4), 109-119. doi: 10.1016/s0169-8095(02)00084-4
- Beauchemin, S., Hesterberg, D., Chou, J., Beauchemin, M., Simard, R. R., & Sayers, D. E. (2003). Speciation of phosphorus in phosphorus-enriched agricultural soils using X-ray absorption near-edge structure spectroscopy and chemical fractionation. *Journal Of Environmental Quality*, 32(5), 1809-1819.
- Benitez-Nelson, C. R. (2000). The biogeochemical cycling of phosphorus in marine systems. *Earth-Science Reviews*, 51(1-4), 109-135.
- Blain, S., Bonnet, S., & Guieu, C. (2008). Dissolved iron distribution in the tropical and subtropical South Eastern Pacific. *Biogeosciences*, 5, 269-280. doi: 10.5194/bg-5-269-2008
- Boyd, P. W., Mackie, D. S., & Hunter, K. A. (2010). Aerosol iron deposition to the surface ocean - Modes of iron supply and biological responses. *Marine Chemistry*, 120(1-4), 128-143. doi: 10.1016/j.marchem.2009.01.008

- Boyd, P. W., Watson, A. J., Law, C. S., Abraham, E. R., Trull, T., Murdoch, R., . . . Zeldis, J. (2000). A mesoscale phytoplankton bloom in the polar Southern Ocean stimulated by iron fertilization. *Nature*, *407*(6805), 695-702. doi: 10.1038/35037500
- Buck, C. S., Landing, W. M., Resing, J. A., & Lebon, G. T. (2006). Aerosol iron and aluminum solubility in the northwest Pacific Ocean: Results from the 2002 IOC cruise. *Geochemistry, Geophysics, Geosystems*, *7*(4). doi: 10.1029/2005GC00097
- Buck, C. S., Landing, W. M., Resing, J. A., & Measures, C. (2010). The solubility and deposition of aerosol Fe and other trace elements in the North Atlantic Ocean: Observations from the A16N CLIVAR/CO2 repeat hydrography section. *Marine Chemistry*, *120*(1-4), 57-70. doi: 10.1016/j.marchem.2008.08.003
- Buesseler, K. O., Andrews, J. E., Pike, S. M., & Charette, M. A. (2004). The effects of iron fertilization on carbon sequestration in the Southern Ocean. *Science*, *304*(5669), 414-417. doi: 10.1126/science.1086895
- Bufalini, M. (1971). Oxidation of sulfur dioxide in polluted atmospheres - review. *Environmental Science & Technology*, *5*(8), 685-&. doi: 10.1021/es60055a001
- Burnett, R. T., Dales, R., Krewski, D., Vincent, R., Dann, T., & Brook, J. R. (1995). Associations between ambient particulate sulfate and admissions to Ontario hospitals for cardiac and respiratory-diseases. *American Journal of Epidemiology*, *142*(1), 15-22.
- Burrows, S. M., Elbert, W., Lawrence, M. G., & Poschl, U. (2009). Bacteria in the global atmosphere - Part 1: Review and synthesis of literature data for different ecosystems. *Atmospheric Chemistry and Physics*, *9*(23), 9263-9280.
- Butler, A. J., Andrew, M. S., & Russell, A. G. (2003). Daily sampling of PM2.5 in Atlanta: Results of the first year of the assessment of spatial aerosol composition in Atlanta study. *Journal of Geophysical Research-Atmospheres*, *108*(D7), SOS 3-1-SOS 3-11. doi: 10.1029/2002JD002234
- Cao, J. J., Li, Y. K., Jiang, T., & Hu, G. (2015). Sulfur-containing particles emitted by concealed sulfide ore deposits: an unknown source of sulfur-containing particles in the atmosphere. *Atmospheric Chemistry and Physics*, *15*, 6959-6969. doi: 10.5194/acp-15-6959-2015
- Chamard, P., Thiery, F., Di Sarra, A., Ciattaglia, L., De Silvestri, L., Grigioni, P., . . . Piacentino, S. (2003). Interannual variability of atmospheric CO(2) in the Mediterranean: measurements at the island of Lampedusa. *Tellus Series B-Chemical and Physical Meteorology*, *55*(2), 83-93. doi: 10.1034/j.1600-0889.2003.00048.x

- Charlson, R. J., Lovelock, J. E., Andreae, M. O., & Warren, S. G. (1987). Oceanic phytoplankton, atmospheric sulfur, cloud albedo and climate. *Nature*, 326(6114), 655-661. doi: 10.1038/326655a0
- Chen, H. Y., Fang, T. H., Preston, M. R., & Lin, S. (2006). Characterization of phosphorus in the aerosol of a coastal atmosphere: Using a sequential extraction method. *Atmospheric Environment*, 40(2), 279-289. doi: 10.1016/j.atmosenv.2005.09.051
- Chen, Y., & Siefert, R. L. (2003). Determination of various types of labile atmospheric iron over remote oceans. *Journal of Geophysical Research-Atmospheres*, 108(D24). doi: 10.1029/2003JD003515
- Coale, K. H., Johnson, K. S., Chavez, F. P., Buesseler, K. O., Barber, R. T., Brzezinski, M. A., . . . Johnson, Z. I. (2004). Southern ocean iron enrichment experiment: Carbon cycling in high- and low-Si waters. *Science*, 304(5669), 408-414.
- Coale, K.H. , Johnson, K.S., & Fitzwater, S. E. (1996). A massive phytoplankton bloom induced by an ecosystem-scale iron fertilization experiment in the equatorial Pacific Ocean. *Nature*, 383, 495-501.
- Cornell, R. M., & Schindler, P. W. (1987). Photochemical dissolution of goethite in acid/oxalate solution. *Clays and Clay Minerals*, 35(5), 347-352. doi: 10.1346/CCMN.1987.0350504
- Cornell, R. M., & Schwertmann, U. (1996). *The iron oxides, structure, properties, reactions, occurrence and uses*. Hokoken, NJ: John Wiley.
- Cozzi, Federico, Pellegrini, Italo, Adami, Gianpiero, Reisenhofer, Edoardo, Bovenzi, Massimo, & Barbieri, Pierluigi. (2009). Sulphur speciation of PM10 samples by XANES spectroscopy. *Central European Journal of Chemistry*, 7(3), 395-401. doi: 10.2478/s11532-009-0052-9
- Craig, N. L., Harker, A. B., & Novakov, T. (1974). Determination of chemical states of sulfur in ambient pollution aerosols by X-ray photoelectron-spectroscopy. *Atmospheric Environment*, 8(1), 15-21. doi: 10.1016/0004-6981(74)90108-5
- Cwiertny, D. M., Baltrusaitis, J., Hunter, G. J., Laskin, A., Scherer, M. M., & Grassian, V. H. (2008). Characterization and acid-mobilization study of iron-containing mineral dust source materials. *Journal of Geophysical Research*, 113(D05202). doi: 10.1029/2007JD009332
- Dabek-Zlotorzynska, E., Kelly, M., Chen, H., & Chakrabarti, C. L. (2003). Evaluation of capillary electrophoresis combined with a BCR sequential extraction for

- determining distribution of Fe, Zn, Cu, Mn, and Cd in airborne particulate matter. *Analytica Chimica Acta*, 498(1-2), 175-187. doi: 10.1016/j.aca.2003.06.002
- de Jong, Jeroen, Schoemann, Veronique, Lannuzel, Delphine, Croot, Peter, de Baar, Hein, & Tison, Jean-Louis. (2012). Natural iron fertilization of the Atlantic sector of the Southern Ocean by continental shelf sources of the Antarctic Peninsula. *Journal of Geophysical Research-Biogeosciences*, 117. doi: G01029
10.1029/2011jg001679
- de Jonge, M. D., Paterson, D., McNulty, I., Rau, C., Brandes, J. A., & Ingall, E. (2010). An energy and intensity monitor for X-ray absorption near-edge structure measurements. *Nuclear Instruments & Methods in Physics Research Section a-Accelerators Spectrometers Detectors and Associated Equipment*, 619(1-3), 154-156. doi: 10.1016/j.nima.2010.01.001
- De Santiago, A., Longo, A. F., Ingall, E. D., Diaz, J. M., King, L. E., Lai, B., . . . Oakes, M. (2014). Characterization of selenium in ambient aerosols and primary emission sources. *Environmental Science & Technology*, 48(16), 8988-8994. doi: 10.1021/es500379y
- Diaz, J., Ingall, E., Benitez-Nelson, C., Paterson, D., de Jonge, M. D., McNulty, I., & Brandes, J. A. (2008). Marine polyphosphate: A key player in geologic phosphorus sequestration. *Science*, 320(5876), 652-655. doi: 10.1126/science.1151751
- Dockery, D. W., & Pope, C. A. (1994). Acute respiratory effects of particulate air-pollution. *Annual Review of Public Health*, 15, 107-132. doi: 10.1146/annurev.pu.15.050194.000543
- Draxler, R. R., & Hess, G. D. (1998). An overview of the HYSPLIT_4 modelling system for trajectories, dispersion and deposition. *Australian Meteorological Magazine*, 47(4), 295-308.
- Eatough, D. J., Major, T., Ryder, J., Hill, M., Mangelson, N. F., Eatough, N. L., . . . Fischer, J. W. (1978). FORMATION AND STABILITY OF SULFITE SPECIES IN AEROSOLS. *Atmospheric Environment*, 12(1-3), 263-271. doi: 10.1016/0004-6981(78)90206-8
- Engelstaedter, S., Tegen, I., & Washington, R. (2006). North African dust emissions and transport. *Earth-Science Reviews*, 79(1-2), 73 - 100. doi: 10.1016/j.earscirev.2006.06.004
- Escudero, M., Stein, A. F., Draxler, R. R., Querol, X., Alastuey, A., Castillo, S., & Avila, A. (2011). Source apportionment for African dust outbreaks over the Western Mediterranean using the HYSPLIT model. *Atmospheric Research*, 99(3-4), 518-527. doi: 10.1016/j.atmosres.2010.12.002

- Fang, T., Guo, H., Verma, V., Peltier, R. E., & Weber, R. J. (2015). PM2.5 water-soluble elements in the southeastern United States: automated analytical method development, spatiotemporal distributions, source apportionment, and implications for health studies. *Atmospheric Chemistry and Physics*, *15*, 11667-11682. doi: 10.5194/acp-15-11667-2015
- Farges, F., Keppler, H., Flank, A. M., & Lagarde, P. (2009). Sulfur K-edge XANES study of S sorbed onto volcanic ashes. *Journal of Physics: Conference Series*, *190*. doi: 10.1088/1742-6596/190/1/012177
- Fittschen, U. E. A., Meirer, F., Strelt, C., Wobrauschek, P., Thiele, J., Falkenberg, G., & Peponi, G. (2008). Characterization of atmospheric aerosols using Synchrotron radiation total reflection X-ray fluorescence and Fe K-edge total reflection X-ray fluorescence-X-ray absorption near-edge structure. *Spectrochimica Acta Part B - Atomic Spectroscopy*, *63*(12), 1489-1495. doi: 10.1016/j.sab.2008.10.016
- Fountoukis, C., & Nenes, A. (2007). ISORROPIA II: a computationally efficient thermodynamic equilibrium model for K⁺-Ca²⁺-Mg²⁺-NH₄⁽⁺⁾-Na⁺-SO₄²⁻-NO₃⁻-Cl⁻-H₂O aerosols. *Atmospheric Chemistry and Physics*, *7*(17), 4639-4659.
- Fu, H. B., Shang, G. F., Lin, J., Hu, Y. J., Hu, Q. Q., Guo, L., . . . Chen, J. M. (2014). Fractional iron solubility of aerosol particles enhanced by biomass burning and ship emissions in Shanghai, East China. *Science of the Total Environment*, *481*, 377-391. doi: 10.1016/j.scitotenv.2014.01.118
- Galloway, J. N. (1995). Acid deposition: Perspectives in time and space. *Water Air and Soil Pollution*, *85*(1), 15-24. doi: 10.1007/bf00483685
- Ganor, E., & Mamane, Y. (1982). Transport of Saharan dust across the Eastern Mediterranean. *Atmospheric Environment*, *16*(3), 581-587. doi: 10.1016/0004-6981(82)90167-6
- Gao, Y., Xu, G., Zhan, J., Zhang, J., Li, W., Lin, Q., . . . Lin, H. (2013). Spatial and particle size distributions of atmospheric dissolvable iron in aerosols and its input to the Southern Ocean and coastal East Antarctica. *Journal of Geophysical Research: Atmospheres*, *118*(12), 634-648. doi: 10.1002/2013JD020367
- Graham, W. F., & Duce, R. A. (1982). The atmospheric transport of phosphorus to the western North-Atlantic. *Atmospheric Environment*, *16*(5), 1089-1097. doi: 10.1016/0004-6981(82)90198-6
- Guerzoni, S., Chester, R., Dulac, F., Herut, B., Loye-Pilot, M. D., Measures, C., . . . Ziveri, P. (1999). The role of atmospheric deposition in the biogeochemistry of the Mediterranean Sea. *Progress in Oceanography*, *44*(1-3), 147-190. doi: 10.1016/s0079-6611(99)00024-5

- Guo, H., Xu, L., Bougiatioti, A., Cerully, K. M., Capps, S. L., Hite, J. R., . . . Weber, R. J. (2015). Fine-particulate water and pH in the southeastern United States. *Atmospheric Chemistry and Physics*, *15*, 5211-5228. doi: 10.5194/acp-15-5211-2015
- Hamza, W., Enan, M. R., Al-Hassini, H., Stuut, J. B., & de-Beer, D. (2011). Dust storms over the Arabian Gulf: a possible indicator of climate changes consequences. *Aquatic Ecosystem Health & Management*, *14*(3), 260-268. doi: 10.1080/14634988.2011.601274
- Hennigan, C. J., Izumi, J., Sullivan, A. P., Weber, R. J., & Nenes, A. (2015a). A critical evaluation of proxy methods use to estimate the acidity of atmospheric particles. *Atmospheric Chemistry and Physics*, *15*, 2775-2790. doi: 10.5194/acp-15-2775-2015
- Hennigan, C. J., Izumi, J., Sullivan, A. P., Weber, R. J., & Nenes, A. (2015b). A critical evaluation of proxy methods used to estimate the acidity of atmospheric particles. *Atmospheric Chemistry and Physics*, *15*, 2775-2790. doi: 10.5194/acp-15-2775-2015
- Herut, B., Collier, R., & Krom, M. D. (2002). The role of dust in supplying nitrogen and phosphorus to the Southeast Mediterranean. *Limnology and Oceanography*, *47*(3), 870-878.
- Herut, B., Zohary, T., Krom, M. D., Mantoura, R. F. C., Pitta, P., Psarra, S., . . . Thingstad, T. F. (2005). Response of East Mediterranean surface water to Saharan dust: On-board microcosm experiment and field observations. *Deep-Sea Research Part II-Topical Studies in Oceanography*, *52*(22-23), 3024-3040. doi: 10.1016/j.dsr.2005.09.003
- Hesterberg, D., Zhou, W. Q., Hutchison, K. J., Beauchemin, S., & Sayers, D. E. (1999). XAFS study of adsorbed and mineral forms of phosphate. *Journal of Synchrotron Radiation*, *6*, 636-638.
- Hesterberg, Dean. (2010). Chapter 11 - Macroscale Chemical Properties and X-Ray Absorption Spectroscopy of Soil Phosphorus. In S. Balwant & G. Markus (Eds.), *Developments in Soil Science* (Vol. Volume 34, pp. 313-356): Elsevier.
- Higashi, M., & Takahashi, Y. (2009). Detection of S(IV) Species in Aerosol Particles Using XANES Spectroscopy. *Environmental Science & Technology*, *43*(19), 7357-7363. doi: 10.1021/es900163y
- Hoffmann, P., Dedik, A. N., Enslin, J., Weinbruch, S., Weber, S., Sinner, T., . . . M., Ortner, H. (1996). Speciation of iron in atmospheric aerosol samples. *Journal of Aerosol Science*, *27*(2), 325-337. doi: 10.1016/0021-8502(95)00563-3

- Hu, Y., Balachandran, S., Pachon, J. E., Baek, J., Ivey, C., Holmes, H., . . . Russell, A. G. (2014). Fine particulate matter source apportionment using a hybrid chemical transport and receptor model approach. *Atmospheric Chemistry and Physics*, *14*(11), 5415-5431. doi: 10.5194/acp-14-5415-2014
- Huffman, G. P., Mitra, S., Huggins, F. E., Shah, N., Vaidya, S., & Lu, F. L. (1991). Quantitative-analysis of all major forms of sulfur in coal by X-ray absorption fine-structure spectroscopy. *Energy & Fuels*, *5*(4), 574-581. doi: 10.1021/ef00028a008
- Huggins, F. E., Shah, N., Huffman, G. P., & Robertson, J. D. (2000). XAFS spectroscopic characterization of elements in combustion ash and fine particulate matter. *Fuel Processing Technology*, *65*, 203-218. doi: 10.1016/s0378-3820(99)00089-2
- Ingall, E, Diaz, J., Longo, A., Oakes, M., Finney, L., Vogt, S., . . . Brandes, J. (2013). Role of biogenic silica in the removal of iron from Antarctic Seas. *Nature Commun.* , *4*:1981 doi: doi: 10.1038/ncomms2981
- Ingall, ED, Brandes, JA, Diaz, JM, de Jonge, MD, Paterson, D, McNulty, I, . . . Northrup, P. (2011). Phosphorus K-edge XANES spectroscopy of mineral standards. *Journal of Synchrotron Radiation*, *18*, 189-197. doi: 10.1107/s0909049510045322
- Ito, A., & Feng, Y. (2010). Role of dust alkalinity in acid mobilization of iron. *Atmospheric Chemistry and Physics*, *10*, 9237-9250. doi: doi:10.5194/acp-10-9237-2010
- Ito, A., & Feng, Y. (2011). Iron mobilization in North African Dust. *Procedia Environmental Sciences*, *6*, 27-34. doi: 10.1016/j.proenv.2011.05.004
- Izquierdo, R., Benitez-Nelson, C. R., Masque, P., Castillo, S., Alastuey, A., & Avila, A. (2012). Atmospheric phosphorus deposition in a near-coastal rural site in the NE Iberian Peninsula and its role in marine productivity. *Atmospheric Environment*, *49*, 361-370. doi: 10.1016/j.atmosenv.2011.11.007
- Jickells, T. D., An, Z. S., Andersen, K. K., Baker, A. R., Bergametti, G., Brooks, N., . . . Torres, R. (2005). Global iron connections between desert dust, ocean biogeochemistry, and climate. *Science*, *308*(5718), 67-71. doi: 10.1126/science.1105959
- Johnson, M. S., & Meskhidze, N. (2013). Atmospheric dissolved iron deposition to the global oceans: effects of oxalate-promoted dissolution, photochemical redox cycling, and dust mineralogy. *Geoscientific Model Development*, *6*, 1137 - 1155. doi: 10.5194/gmd-6-1137-2013

- Journet, E., Desboeufs, K. V., Caquineau, S., & Colin, J. L. (2008). Mineralogy as a critical factor of dust iron solubility. *Geophysical Research Letters*, *35*(7). doi: 10.1029/2007GL031589
- Kadko, D., Landing, W. M., & Shelley, R. U. (2015). A novel tracer technique to quantify the atmospheric flux of trace elements to remote ocean regions. *Journal of Geophysical Research-Oceans*, *119*. doi: 10.1002/2014JC010314
- Kalivitis, N., Gerasopoulos, E., Vrekoussis, M., Kouvarakis, G., Kubilay, N., Hatzianastassiou, N., . . . Mihalopoulos, N. (2007). Dust transport over the eastern Mediterranean derived from Total Ozone Mapping Spectrometer, Aerosol Robotic Network, and surface measurements. *Journal of Geophysical Research-Atmospheres*, *112*(D3). doi: 10.1029/2006jd007510
- Kay, K. (1952). Analytical methods used in air pollution study. *Industrial and Engineering Chemistry*, *44*(6), 1383-1388. doi: 10.1021/ie50510a052
- Kelly, F. J. (2003). Oxidative stress: Its role in air pollution and adverse health effects. *Occupational and Environmental Medicine*, *60*(8), 612-616. doi: 10.1136/oem.60.8.612
- Kouvarakis, G., Mihalopoulos, N., Tselepidis, A., & Stavrakaki, S. (2001). On the importance of atmospheric inputs of inorganic nitrogen species on the productivity of the eastern Mediterranean Sea. *Global Biogeochemical Cycles*, *15*(4), 805-817. doi: 10.1029/2001gb001399
- Krom, M. D., Emeis, K. C., & Van Cappellen, P. (2010). Why is the Eastern Mediterranean phosphorus limited? *Progress in Oceanography*, *85*(3-4), 236-244. doi: 10.1016/j.pocean.2010.03.003
- Krom, M. D., Kress, N., Brenner, S., & Gordon, L. I. (1991). PHOSPHORUS LIMITATION OF PRIMARY PRODUCTIVITY IN THE EASTERN MEDITERRANEAN-SEA. *Limnology and Oceanography*, *36*(3), 424-432.
- Kumar, A. , Sarin, M., & Srinivas, B. (2010). Aerosol iron solubility over Bay of Bengal: Role of anthropogenic sources and chemical processing. *Marine Chemistry*, *121*(1-4), 167-175. doi: 10.1016/j.marchem.2010.04.005
- Kumar, A., & Sarin, M. (2009). Aerosol iron solubility in a semi-arid region: temporal trend and impact of anthropogenic sources. *Tellus Series B-Chemical and Physical Meteorology*, *62*(2), 125-132. doi: 10.1111/j.1600-0889.2009.00448.x
- Lenes, J. M., Prospero, J. M., Landing, W. M., Virmani, J. I., & Walsh, J. J. (2012). A model of Saharan dust deposition to the eastern Gulf of Mexico. *Marine Chemistry*, *134*, 1-9. doi: 10.1016/j.marchem.2012.02.007

- Liao, H., Adams, P. J., Chung, S. H., Seinfeld, J. H., Mickley, L. J., & Jacob, D. J. (2003). Interactions between tropospheric chemistry and aerosols in a unified general circulation model. *Journal of Geophysical Research*, *108*(D1), 4001. doi: 10.1029/2001JD001260
- Long, S. L., Zeng, J. R., Li, Y., Bao, L. M., Cao, L. L., Liu, K., . . . Zhao, Y. D. (2014). Characteristics of secondary inorganic aerosol and sulfate species in size-fractionated aerosol particles in Shanghai. *Journal of Environmental Science-China*, *26*(5), 1040-1051. doi: 10.1016/S1001-0742(13)60521-5
- Longo, A. F., Ingall, E. D., Diaz, J. M., Oakes, M., King, L. E., Nenes, A., . . . Vine, D. J. (2014). P-NEXFS analysis of aerosol phosphorus delivered to the Mediterranean Sea. *Geophysical Research Letters*, *41*(11), 4043-4049. doi: 10.1002/2014GL060555
- Mackey, K. R. M., Roberts, K., Lomas, M. W., Saito, M. A., Post, A. F., & Paytan, A. (2012). Enhanced Solubility and Ecological Impact of Atmospheric Phosphorus Deposition upon Extended Seawater Exposure. *Environmental Science & Technology*, *46*(19), 10438-10446. doi: 10.1021/es3007996
- Mahowald, N., Albani, S., Kok, J. F., Engelstaedter, S., Scanza, R., Ward, D. S., & Flanner, M. G. (2014). The size distribution of desert dust aerosols and its impact on the Earth system. *Aeolian Research*, *15*, 53-71. doi: 10.1016/j.aeolia.2013.09.002
- Mahowald, N., Baker, A. R., Bergametti, G., Brooks, N., Duce, R. A., Jickells, T. D., . . . Tegen, I. (2005). Atmospheric global dust cycle and iron inputs to the ocean. *Global Biogeochemical Cycles*, *19*(GB4025). doi: doi:10.1029/2004GB002402
- Mahowald, N., Jickells, T. D., Baker, A. R., Artaxo, P., Benitez-Nelson, C. R., Bergametti, G., . . . Tsukuda, S. (2008). Global distribution of atmospheric phosphorus sources, concentrations and deposition rates, and anthropogenic impacts. *Global Biogeochemical Cycles*, *22*(4). doi: 10.1029/2008gb003240
- Majestic, B. J., Schauer, J. J., & Shafer, M. M. (2007). Application of synchrotron radiation for measurement of iron red-ox speciation in atmospherically processed aerosols. *Atmospheric Chemistry and Physics*, *7*(10), 2475-2487.
- Marcus, M. A., & Lam, P. J. (2014). Visualising Fe speciation diversity in ocean particulate samples by micro X-ray absorption near-edge spectroscopy. *Environmental Chemistry*, *11*(1), 10-17. doi: 10.1071/EN13075
- Markaki, Z., Oikonomou, K., Kocak, M., Kouvarakis, G., Chaniotaki, A., Kubilay, N., & Mihalopoulos, N. (2003). Atmospheric deposition of inorganic phosphorus in the

- Levantine Basin, eastern Mediterranean: Spatial and temporal variability and its role in seawater productivity. *Limnology and Oceanography*, 48(4), 1557-1568.
- Martin, J. H. (1990). Glacial-Interglacial CO₂ Change: The Iron Hypothesis. *Paleoceanography*, 5(1), 1-13. doi: 10.1029/PA005i001p00001
- Matsumoto, S., Tanaka, Y., Ishii, H., Tanabe, T., Kitajima, Y., & Kawai, J. (2006). Sulfur chemical state analysis of diesel emissions of vehicles using X-ray absorption. *Spectrochimica Acta Part B-Atomic Spectroscopy*, 61(8), 991-994. doi: 10.1016/j.sab.2006.06.013
- McInnes, K. L., Erwin, T. A., & Bathols, J. M. (2011). Global Climate Model projected changes in 10 m wind speed and direction due to anthropogenic climate change. *Atmospheric Science Letters*, 12(4), 325-333. doi: Doi 10.1002/Asl.341
- McNulty, I., Paterson, D., Arko, J., Erdmann, M., Frigo, S. P., Goetze, K., . . . Xu, S. (2003). The 2-ID-B intermediate-energy scanning X-ray microscope at the APS. *Journal De Physique Iv*, 104, 11-15. doi: 10.1051/jp4:200300019
- Meskhidze, N., Chameides, W. L., & Nenes, A. (2005). Dust and pollution: A recipe for enhanced ocean fertilization? *Journal of Geophysical Research-Atmospheres*, 110(D3). doi: 10.1029/2004JD005082
- Meskhidze, N., Chameides, W. L., Nenes, A., & Chen, G. (2003). Iron mobilization in mineral dust: Can anthropogenic SO₂ emissions affect ocean productivity? *Geophysical Research Letters*, 30(21). doi: 10.1029/2003GL018035
- Moffet, R. C., Furutani, H., Rodel, T. C., Henn, T. R., Sprau, P. O., Laskin, A., . . . Gilles, M. K. (2012). Iron speciation and mixing in single aerosol particles from Asian continental outflows. *Journal of Geophysical Research*, 117(D07204). doi: 10.1029/2011JD016746
- Moffet, Ryan C., Furutani, Hiroshi, Roedel, Tobias C., Henn, Tobias R., Sprau, Peter O., Laskin, Alexander, . . . Gilles, Mary K. (2012). Iron speciation and mixing in single aerosol particles from the Asian continental outflow. *Journal of Geophysical Research-Atmospheres*, 117. doi: 10.1029/2011jd016746
- Moore, C. M., Mills, M. M., Arrigo, K. R., Berman-Frank, I., Bopp, L., Boyd, P. W., . . . Ulloa, O. (2013). Processes and patterns of oceanic nutrient limitation. *Nature Geoscience*, 6, 701 - 710. doi: doi:10.1038/ngeo1765
- Morra, M. J., Fendorf, S. E., & Brown, P. D. (1997). Speciation of sulfur in humic and fulvic acids using X-ray absorption near-edge structure (XANES) spectroscopy. *Geochimica Et Cosmochimica Acta*, 61(3), 683-688. doi: 10.1016/S0016-7037(97)00003-3

- Morton, P. L. , Landing, W. M., Hsu, S. C. , Milne, A. , Aguilar-Islas, A. M., Baker, A. R., . . . Zamora, L. M. (2013). Methods for the sampling and analysis of marine aerosols: results from the 2008 GEOTRACES aerosol intercalibration experiment. *Limnology and Oceanography*, *11*, 62-78. doi: 10.4319/lom.2013.11.62
- Munger, Hamnett P. (1952). The engineering approach to cleaner air for the community. *Amer Jour Publ Health*, *42*((8)), 936-946.
- Murphy, J., & Riley, J.P. (1962). A modified single solution method for the determination of phosphate in natural waters. *Analyt. Chim. Acta*, *27*, 31-36.
- Nenes, A., Krom, M. D., Mihalopoulos, N., Van Cappellen, P., Shi, Z., Bougiatioti, A., . . . Herut, B. (2011). Atmospheric acidification of mineral aerosols: a source of bioavailable phosphorus for the oceans. *Atmospheric Chemistry and Physics*, *11*(13), 6265-6272. doi: 10.5194/acp-11-6265-2011
- Nenes, A., Pandis, S. N., & Pilinis, C. (1998). ISORROPIA: A new thermodynamic equilibrium model for multiphase multicomponent inorganic aerosols. *Aquatic Geochemistry*, *4*(1), 123-152. doi: 10.1023/a:1009604003981
- Nikolaou, P, Bougiatioti, A., Stavroulas, I., Kouvarakis, G., Nenes, A., Weber, R. J., . . . Mihalopoulos, N. (2015). Particle water and pH in the Eastern Mediterranean: sources variability and implications for nutrients availability. *Atmospheric Chemistry and Physics*, *15*. doi: 10.5194/acpd-15-29523-2015
- Oakes, M., Ingall, E. D., Lai, B., Shafer, M. M., Hays, M. D., Liu, Z. G., . . . Weber, R. J. (2012). Iron Solubility Related to Particle Sulfur Content in Source Emission and Ambient Fine Particles. *Environmental Science & Technology*, *46*(12), 6637-6644. doi: 10.1021/es300701c
- Oakes, M., Weber, R. J., Lai, B., Russell, A., & Ingall, E. D. (2012). Characterization of iron speciation in urban and rural single particles using XANES spectroscopy and micro X-ray fluorescence measurements: investigating the relationship between speciation and fractional iron solubility. *Atmospheric Chemistry and Physics*, *12*(2), 745-756. doi: 10.5194/acp-12-745-2012
- Paris, R., Desboeufs, K. V., & Journet, E. (2011). Variability of dust iron solubility in atmospheric waters: Investigation of the role of oxalate organic complexation. *Atmospheric Environment*, *45*(36), 6510-6517. doi: 10.1016/j.atmosenv.2011.08.068
- Pongpiachan, S., Thumanu, K., Kositanont, C., Schwarzer, K., Prietzel, J., Hirunyatrakul, P., & Kittikoon, I. (2012). Parameters influencing sulfur speciation in environmental samples using sulfur K-edge X-ray absorption near-edge structure. *Journal of Analytical Methods in Chemistry*. doi: 10.1155/2012/659858

- Pongpiachan, S., Thumanu, K., Na Pattalung, W., Hirunyatrakul, P., Kittikoon, I., Fai Ho, K., & Cao, J. J. (2012). Diurnal variation and spatial distribution effects on sulfur speciation in aerosol samples as assessed by X-ray absorption near-edge structure (XANES). *Journal of Analytical Methods in Chemistry*. doi: 10.1155/2012/696080
- Prietzl, J., Botzaki, A., Tyufekchieva, N., Brettholle, M., Thieme, J., & Klysubun, W. (2011). Sulfur Speciation in Soil by S K-Edge XANES Spectroscopy: Comparison of Spectral Deconvolution and Linear Combination Fitting. *Environmental Science & Technology*, 45(7), 2878-2886. doi: 10.1021/es102180a
- Prietzl, J., Thieme, J., Eusterhues, K., & Eichert, D. (2007). Iron speciation in soils and soil aggregates by synchrotron-based X-ray microspectroscopy (XANES, mu-XANES). *European Journal of Soil Science*, 58(5), 1027-1041. doi: 10.1111/j.1365-2389.2006.00882.x
- Prietzl, Jörg, Dümig, Alexander, Wu, Yanhong, Zhou, Jun, & Klysubun, Wantana. (2013). Synchrotron-based P K-edge XANES spectroscopy reveals rapid changes of phosphorus speciation in the topsoil of two glacier foreland chronosequences. *Geochimica Et Cosmochimica Acta*, 108(0), 154-171. doi: <http://dx.doi.org/10.1016/j.gca.2013.01.029>
- Querol, X., Alastuey, A., Chaves, A., Spiro, B., Plana, F., & Lopez-Soler, A. (2000). Sources of natural and anthropogenic sulphur around the Teruel power station, NE Spain. Inferences from sulphur isotope geochemistry. *Atmospheric Environment*, 34(2), 333-345. doi: 10.1016/s1352-2310(99)00188-0
- Quinn, P. K., & Bates, T. S. (2011). The case against climate regulation via oceanic phytoplankton sulphur emissions. *Nature*, 480(7375), 51-56. doi: 10.1038/nature10580
- Ramanathan, V., Crutzen, P. J., Kiehl, J. T., & Rosenfeld, D. (2001). Atmosphere - Aerosols, climate, and the hydrological cycle. *Science*, 294(5549), 2119-2124. doi: 10.1126/science.1064034
- Ravel, B., & Newville, M. (2005). ATHENA, ARTEMIS, HEPHAESTUS: data analysis for X-ray absorption spectroscopy using IFEFFIT. *Journal of Synchrotron Radiation*, 12, 537-541. doi: 10.1107/s0909049505012719
- Ridame, C., & Guieu, C. (2002). Saharan input of phosphate to the oligotrophic water of the open western Mediterranean Sea. *Limnology and Oceanography*, 47(3), 856-869.

- Schindelin, J., Arganda-Carreras, I., Frise, E., Kaynig, V., Longair, M., Pietzsch, T., . . . Cardona, A. (2012). Fiji: an open-source platform for biological-image analysis. *Nature Methods*, 9(7), 676-682. doi: 10.1038/nmeth.2019
- Schmitt-Kopplin, P., Gelencser, A., Dabek-Zlotorzynska, E., Kiss, G., Hertkorn, N., Harir, M., . . . Gebefugi, I. (2010). Analysis of the Unresolved Organic Fraction in Atmospheric Aerosols with Ultrahigh-Resolution Mass Spectrometry and Nuclear Magnetic Resonance Spectroscopy: Organosulfates As Photochemical Smog Constituents. *Analytical Chemistry*, 82(19), 8017-8026. doi: 10.1021/ac101444r
- Schroth, A. W., Crusius, J., Sholkovitz, E. R., & Bostick, B. C. (2009). Iron solubility driven by speciation in dust sources to the ocean. *Nature Geoscience*, 2(5), 337-340. doi: 10.1038/ngeo501
- Schulz, M., Prospero, J. M., Baker, A. R., Dentener, F. J., Ickes, L., Liss, P. S., . . . Duce, R. A. (2012). Atmospheric Transport and Deposition of Mineral Dust to the Ocean: Implications for Research Needs. *Environmental Science & Technology*, 46(19), 10390-10404. doi: 10.1021/es300073u
- Schwartz, J., Dockery, D. W., & Neas, L. M. (1996). Is daily mortality associated specifically with fine particles? *Journal of the Air & Waste Management Association*, 46(10), 927-939.
- Sedwick, P., Sholkovitz, E. R., & Church, T. M. (2007). Impact of anthropogenic combustion emissions on the fractional solubility of aerosol iron: Evidence from the Sargasso Sea. *Geochemistry, Geophysics, Geosystems*, 8(10). doi: 10.1029/2007GC001586
- Shafer, Martin M., Perkins, Dawn A., Antkiewicz, Dagmara S., Stone, Elizabeth A., Quraishi, Tauseef A., & Schauer, James J. (2010). Reactive oxygen species activity and chemical speciation of size-fractionated atmospheric particulate matter from Lahore, Pakistan: an important role for transition metals. *Journal of Environmental Monitoring*, 12(3), 704-715. doi: 10.1039/b915008k
- Shelley, R. U., Morton, P. L., & Landing, W. M. (2015). Elemental ratios and enrichment factors in aerosols from the US-GEOTRACES north Atlantic transects. *Deep-Sea Research Part I-Tropical Studies in Oceanography*, 116, 262-272. doi: 10.1016/j.dsr2.2014.12.005. 2014
- Shi, Z., Bonneville, S., Krom, M. D., Carslaw, K. S., Jickells, T. D., Baker, A. R., & Benning, L. G. (2011). Iron dissolution kinetics of mineral dust at low pH during simulated atmospheric processing. *Atmospheric Chemistry and Physics*, 11(3), 995-1007. doi: 10.5194/acp-11-995-2011
- Shi, Z., Krom, M. D., Bonneville, S., Baker, A. R., Jickells, T. D., & Benning, L. G. (2009). Formation of iron nanoparticles and increase in iron reactivity in mineral

- dust during simulated cloud processing. *Environmental Science & Technology*, 43(17), 6592-6596. doi: 10.1021/es901294g
- Shi, Z., Krom, M. D., Bonneville, S., & Benning, L. G. (2015). Atmospheric processing outside clouds increases soluble iron in mineral dust. *Environmental Science & Technology*, 49(3), 1472-1477. doi: 10.1021/es504623x
- Shi, Z., Krom, M. D., Jickells, T. D., Bonneville, S., Carslaw, K. S., Mihalopoulos, N., . . . Benning, L. G. (2012). Impacts on iron solubility in the mineral dust by processes in the source region and the atmosphere: A review. *Aeolian Research*, 5, 21-42. doi: 10.1016/j.aeolia.2012.03.001
- Shi, Zongbo, Krom, Michael D., Bonneville, Steeve, Baker, Alex R., Bristow, Charlie, Drake, Nick, . . . Benning, Liane G. (2011). Influence of chemical weathering and aging of iron oxides on the potential iron solubility of Saharan dust during simulated atmospheric processing. *Global Biogeochemical Cycles*, 25. doi: 10.1029/2010gb003837
- Sholkovitz, E. R., Sedwick, P. N., & Church, T. M. (2009). Influence of anthropogenic combustion emissions on the deposition of soluble aerosol iron to the ocean: Empirical estimates for island sites in the North Atlantic. *Geochimica Et Cosmochimica Acta*, 73, 3981-4003. doi: 10.1016/j.gac.2009.04.029
- Sholkovitz, Edward R., Sedwick, Peter N., Church, Thomas M., Baker, Alexander R., & Powell, Claire F. (2012). Fractional solubility of aerosol iron: Synthesis of a global-scale data set. *Geochimica Et Cosmochimica Acta*, 89, 173-189. doi: 10.1016/j.gca.2012.04.022
- Siefert, R. L., Pehkonen, S. O., Erel, Y., & Hoffmann, M. R. (1994). Iron photochemistry of aqueous suspensions of ambient aerosol with added organic acids. *Geochimica Et Cosmochimica Acta*, 58(15), 3217-3279. doi: 10.1016/0016-7037(94)90055-8
- Siefert, R. L., Webb, S. M., & Hoffmann, M. R. (1996). Determination of photochemically available iron in ambient aerosols. *Journal of Geophysical Research*, 10(D9), 14441-14449. doi: 10.1029/96JD00857
- Solomon, D., Lehmann, J., & Martinez, C. E. (2003). Sulfur K-edge XANES spectroscopy as a tool for understanding sulfur dynamics in soil organic matter. *Soil Science Society of America Journal*, 67(6), 1721-1731. doi: 10.2136/sssaj2003.1721
- Spolaor, A., Vallelonga, P., Cozzi, F., Gabrielli, P., Varin, C., Kehrwald, N., . . . Barbante, C. (2013). Iron speciation in aerosol dust influences iron bioavailability over glacial-interglacial timescales. *Geophysical Research Letters*, 40, 1618-1623. doi: 10.1002/grl.50296

- Spolaor, A., Vallelonga, P., Cozzi, G., Gabrieli, J., Varin, C., Kehrwald, N., . . . Barbante, C. (2013). Iron Speciation in aerosol dust influences iron bioavailability over glacial-interglacial timescales. *Geophysical Research Letters*, *40*, 1618-1623. doi: 10.1002/grl.50296
- Srinivas, B., Sarin, M. M., & Kumar, A. K. (2012). Impact of anthropogenic sources on aerosol iron solubility over the Bay of Bengal and the Arabian Sea. *Biogeochemistry*, *110*, 257-268. doi: 10.1007/s10533-011-9680-1
- Srinivas, B., Sarin, M., & Rengarajan, R. (2014). Atmospheric transport of mineral dust from the Indo-Gangetic Plain: Temporal variability, acid processing, and iron solubility. *Geochemistry, Geophysics, Geosystems*, *15*, 3226-3243. doi: 10.1002/2014GC005395
- Stookey, L. L. (1970). Ferrozine - A new spectrophotometric reagent for iron. *ANALYTICAL CHEMISTRY*, *42*(7). doi: 10.1021/ac60289a016
- Sullivan, R. C., Guazzotti, S. A., Sodeman, D. A., & Prather, K. A. (2007). Direct observations of the atmospheric processing of Asian mineral dust. *Atmospheric Chemistry and Physics*, *7*, 1213-1236.
- Surratt, J. D., Gomez-Gonzalez, Y., Chan, A. W. H., Vermeylen, R., Shahgholi, M., Kleindienst, T. E., . . . Seinfeld, J. H. (2008). Organosulfate formation in biogenic secondary organic aerosol. *Journal of Physical Chemistry A*, *112*(36), 8345-8378. doi: 10.1021/jp802310p
- Takahashi, T., Furukawa, T., Kanai, Y., Uematsu, M., Zheng, G., & Marcus, M. A. (2013). Seasonal changes in Fe species and soluble Fe concentration in the atmosphere in the Northwest Pacific region based on the analysis of aerosols collected in Tsukuba, Japan. *Atmospheric Chemistry and Physics*, *13*, 7695-7710. doi: 10.5194/acp-13-7695-2013
- Takahashi, Y., Higashi, M., Furukawa, T., & Mitsunobu, S. (2011). Change of iron species and iron solubility in Asian dust during the long-range transport from western China to Japan. *Atmospheric Chemistry and Physics*, *11*(21), 11237-11252. doi: 10.5194/acp-11-11237-2011
- Takahashi, Y., Kanai, Y., Kamioka, H., Ohta, A., Maruyama, H., Song, Z., & Shimizu, H. (2006). Speciation of sulfate in size-fractionated aerosol particles using sulfur K-edge X-ray absorption near-edge structure. *Environmental Science & Technology*, *40*(16), 5052-5057. doi: 10.1021/es060497y
- Tao, F., Gonzalez-Flecha, B., & Kobzik, L. (2003). Reactive oxygen species in pulmonary inflammation by ambient particulates. *Free Radical Biology & Medicine*, *35*(4), 327-340. doi: 10.1016/S0891-5849(03)00280-6

- Tian, D., Hu, Y. T., Wang, Y. H., Boylan, J. W., Zheng, M., & Russell, A. G. (2009). Assessment of biomass burning emissions and their impacts on urban and regional PM_{2.5}: A Georgia case study. *Environmental Science & Technology*, 43(2), 299-305. doi: 10.1021/es801827s
- Twining, B. S., Baines, S. B., Bozard, J. B., Vogt, S., Walker, E. A., & Nelson, D. M. (2011). Metal quotas of plankton in the equatorial Pacific Ocean. *Deep-Sea Research Part II-Topical Studies in Oceanography*, 58(3-4), 325-341. doi: 10.1016/j.dsr2.2010.08.018
- Twomey, S. (1977). Influence of pollution on shortwave albedo of clouds. *Journal of Atmospheric Sciences*, 34, 1149-1152.
- Van Grieken, R., Delalieux, F., & Gysels, K. (1998). Cultural heritage and the environment. *Pure and Applied Chemistry*, 70(12), 2327-2331. doi: 10.1351/pac199870122327
- Viana, M., Kuhlbusch, T. A. J., Querol, X., Alastuey, A., Harrison, R. M., Hopke, P. K., . . . Hitzenberger, R. (2008). Source apportionment of particulate matter in Europe: A review of methods and results. *Journal of Aerosol Science*, 39(10), 827-849. doi: 10.1016/j.jaerosci.2008.05.007
- Vidrio, E., Jung, H., & Anastasio, C. (2008). Generation of hydroxyl radicals from dissolved transition metals in surrogate lung fluid solutions. *Atmospheric Environment*, 42(18), 4369-4379. doi: 10.1016/j.atmosenv.2008.01.004
- Weber, S., Hoffmann, P., Enslin, J., Dedik, A. N., Weinbruch, S., Miehe, G., . . . Ortner, H. M. (2000). Characterization of iron compounds from urban and rural aerosol sources. *Journal of Aerosol Science*, 31(8), 987-997. doi: 10.1016/S0021-8502(99)00564-9
- Wiederhold, J. G., Kraemer, S. M., Teutsch, N., Borer, P. M., Halliday, A. N., & Kretzschmar, R. (2006). Iron isotope fractionation during proton-promoted, ligand-controlled, and reductive dissolution of goethite. *Environmental Science & Technology*, 40(12), 3787-3793. doi: 10.1021/es052228y
- Wilke, M., Farges, F., Petit, P. E., Brown, G. E., & Martin, F. (2001). Oxidation state and coordination of Fe in minerals: An FeK-XANES spectroscopic study. *American Mineralogist*, 86(5-6), 714-730.
- Winton, V. H. L., Bowie, A. R., Edwards, R., Keywood, M., Townsend, A. T., van der Merwe, P., & Bollhofer, A. (2015). Fractional iron solubility of atmospheric iron inputs to the Southern Ocean. *Marine Chemistry*, 177(1), 20-32. doi: 10.1016/j.marchem.2015.06.006

- Witt, M. L. I., Mather, T. A., Baker, A. R., De Hoog, J. C. M., & Pyle, D. M. (2010). Atmospheric trace metals over the south-west Indian Ocean: Total gaseous mercury, aerosol trace metal concentrations and lead isotope ratios. *Marine Chemistry*, *121*(1-4), 2-16. doi: doi:10.1016/j.marchem.2010.02.005
- Wozniak, A. S., Shelley, R. U., Sleighter, R. L., Abdulla, H. A. N., Morton, P. L., Landing, W. M., & Hatcher, P. G. (2013). Relationships among aerosol water soluble organic matter, iron and aluminum in European, North African, and Marine air masses from the 2010 US GEOTRACES cruise. *Marine Chemistry*, *154*, 24-33. doi: 10.1016/j.marchem.2013.04.011
- Xia, K., Weesner, F., Bleam, W. F., Bloom, P. R., Skyllberg, U. L., & Helmke, P. A. (1998). XANES studies of oxidation states of sulfur in aquatic and soil humic substances. *Soil Science Society of America Journal*, *62*(5), 1240-1246.
- Xu, L., Guo, H., Boyd, C. M., Klein, M., Bougiatioti, A., Cerully, K. M., . . . Ng, N. L. . (2015). Effects of anthropogenic emissions on aerosol formation from isoprene and monoterpenes in the southeastern United States. *Proceedings of the National Academy of Sciences of the United States of America*, *112*(1), 37-42. doi: 10.1073/pnas.1417609112
- Xu, N., & Gao, Y. (2008). Characterization of hematite dissolution affected by oxalate coating, kinetics and pH. *Applied Geochemistry*, *23*(4), 783-793. doi: 10.1016/j.apgeochem.2007.12.026
- Zamora, L. M., Prospero, J. M., Hansell, D. A., & Trapp, J. M. (2013). Atmospheric P deposition to the subtropical North Atlantic: sources, properties, and relationship to N deposition. *Journal of Geophysical Research-Atmospheres*, *118*(3), 1546-1562. doi: 10.1002/jgrd.50187
- Zhang, G. H., Bi, X. H., Lou, S. R., Li, L., Wang, H. L., Wang, X. M., . . . Chen, C. H. (2014). Source and mixing state of iron-containing particles in Shanghai by individual particle analysis. *Chemosphere*, *95*, 9-16. doi: 10.1016/j.chemosphere.2013.04.046
- Zhang, Y., Schauer, J. J., Shafer, M. M., Hannigan, M. P., & Dutton, S. J. (2008). Source apportionment of in vitro reactive oxygen species bioassay activity from atmospheric particulate matter. *Environmental Science & Technology*, *42*(19), 7502-7509. doi: 10.1021/es800126y
- Zhu, X., Prospero, J. M., Savoie, D. L., Millero, F. J., Zika, R. G., & Saltzman, E. S. (1993). Photoreduction of iron(III) in marine mineral aerosol solutions. *Journal of Geophysical Research-Atmospheres*, *98*(D5), 9039-9046. doi: 10.1029/93jd00202

- Zhu, X. R., Prospero, J. M., & Millero, F. J. (1997). Diel variability of soluble Fe (II) and soluble total Fe in North African dust in the trade winds at Barbados. *Journal of Geophysical Research*, 102(D17), 21297 - 21305.
- Zhuang, G., Yi, Z., Duce, R. A., & Brown, P. R. (1992a). Chemistry of iron in marine aerosols. *Global Biogeochemical Cycles*, 6(2), 161-173. doi: 10.1029/92GB00756
- Zhuang, G., Yi, Z., Duce, R. A., & Brown, P. R. (1992b). Link between iron and sulphur cycles suggested by detection of Fe(II) in remote marine aerosols. *Nature*, 335(6360), 537-539. doi: 10.1038/355537a0

VITA

AMELIA F. LONGO

Amelia Longo was born in St. Marys, Georgia. She attended Georgia Institute of Technology, where she received a B.S and M.S. in Environmental Engineering in 2012 and 2013, respectively. Longo then decided to further pursue her education by entering a doctoral studies program at Georgia Institute of Technology in the School of Earth and Atmospheric Sciences. When Longo is not working in the research laboratory or enjoying copious time using the Advanced Photon Source at Argonne National Laboratory, she enjoys playing with her dog, Toby, and her cat, Dusk.